

Investigating Cell Adhesion To Controlled Surface Chemistry via Self-Assembly of  
Binary Composition Alkylthiol Monolayers, Streptavidin Immobilization, and Cell  
Receptor Ligand Attachment

Kjell Erik Nelson

A dissertation submitted in partial fulfillment of the requirements for the degree of

Doctor of Philosophy

University of Washington

2003

Program Authorized to Offer Degree: Department of Bioengineering

UMI Number: 3102688

Copyright 2003 by  
Nelson, Kjell Erik

All rights reserved.

**UMI**<sup>®</sup>

---

UMI Microform 3102688

Copyright 2003 by ProQuest Information and Learning Company.


All rights reserved. This microform edition is protected against  
unauthorized copying under Title 17, United States Code.

ProQuest Information and Learning Company  
300 North Zeeb Road  
P.O. Box 1346  
Ann Arbor, MI 48106-1346

© Copyright 2003

Kjell Erik Nelson

In presenting this dissertation in partial fulfillment of the requirements for the Doctoral degree at the University of Washington, I agree that the Library shall make its copies freely available for inspection. I further agree that extensive copying of the dissertation is allowable only for scholarly purposes, consistent with "fair use" as prescribed in the U.S. Copyright Law. Requests for copying or reproduction of this dissertation may be referred to Proquest Information and Learning, 300 North Zeeb Road, Ann Arbor, MI 48106-1346, to whom the author has granted "the right to reproduce and sell (a) copies of the manuscript in microform and/or (b) printed copies of the manuscript made from microform."

Signature  \_\_\_\_\_  
Date 8/22/03

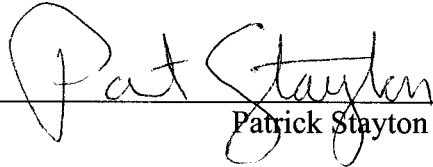
University of Washington  
Graduate School

This is to certify that I have examined this copy of a doctoral dissertation by

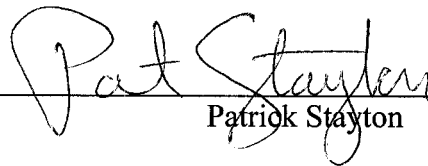
Kjell Erik Nelson

and have found that it is complete and satisfactory in all respects, and that any and all  
revisions required by the final examining committee have been made.

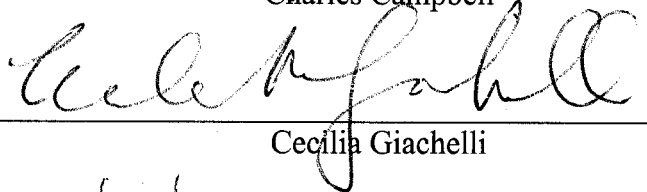
Chair of the Supervisory Committee:

  
\_\_\_\_\_  
Patrick Stayton

Reading Committee:

  
\_\_\_\_\_  
Patrick Stayton

  
\_\_\_\_\_  
Charles Campbell

  
\_\_\_\_\_  
Cecilia Giachelli

Date:

  
\_\_\_\_\_

University of Washington

**Abstract**

Investigating Cell Adhesion To Controlled Surface Chemistry via Self-Assembly of Binary Composition Alkylthiol Monolayers, Streptavidin Immobilization, and Cell Receptor Ligand Attachment

Kjell Erik Nelson

Chair of the Supervisory Committee:  
Professor Patrick Stayton  
Department of Bioengineering

A method of controlling surface chemistry for immobilizing biofunctional ligands for studying in vitro cell response is described. Binary composition self-assembled monolayers (SAMs) of a biotinylated and either an oligo(ethylene oxide) or methylene-terminated alkylthiolate deposited on gold-coated substrates are used to bind streptavidin. Maximal streptavidin adsorption and stability was quantitated and optimized by varying the identity and ratio of the thiolates in the mixed SAMs. The streptavidin coated surfaces were shown to support additional biotinylated ligand adsorption. Sequential biotinylated ligand adsorption is also possible, with the maximum amount of both ligands determined by the streptavidin coverage, which defines the number of available binding sites. The immobilized ligands were used to support adhesion-dependent cell attachment. The attachment was shown to be specific to the identity of the immobilized ligand and to the conjugate cell surface receptor. These substrates can be used to quantitatively immobilize a wide range of ligands with specificity, selectivity, and stability, and the selectively modified substrates can be used as a well-controlled and characterized model system to study the interaction between adhesion-dependent cells in culture to the immobilized ligands.

# Table of Contents

	Page
<b>LIST OF FIGURES.....</b>	<b>iii</b>
<b>LIST OF TABLES.....</b>	<b>ix</b>
<b>GLOSSARY .....</b>	<b>x</b>
<b>1. INTRODUCTION .....</b>	<b>1</b>
Specific Aims:.....	3
Experimental System.....	4
<b>2. MATERIALS AND METHODS .....</b>	<b>13</b>
Organic Synthesis.....	13
Alkylthiolate Monolayer Preparation .....	20
Thiolate Monolayer Surface Analysis .....	25
SPR measurements .....	27
Cell culture.....	29
<b>3. ALKYLTHIOLATE MONOLAYER ASSEMBLY AND CHARACTERIZATION .....</b>	<b>30</b>
Specific aims .....	33
XPS Surface Characterization of Alkylthiolate Monolayers .....	34
Angle-resolved XPS thiolate orientation analysis.....	65

NEXAFS evaluation of intra-thiolate bond orientation.....	81
Determining thickness of BAT / OEG and BAT / MHD SAMs.....	88
Chapter Summary and Conclusions .....	92
<b>4. PROTEIN BINDING AND DESORPTION .....</b>	<b>96</b>
Characterizing and controlling non-specific protein adsorption.....	101
Characterizing and quantitating biotin-mediated streptavidin adsorption.....	106
Demonstrating Specificity, Affinity, and Avidity of SA binding .....	117
Protein multilayer assembly.....	123
Chapter Summary and Conclusions .....	130
<b>5. CELL RESPONSE TO IMMOBILIZED PROTEINS.....</b>	<b>132</b>
Cell adhesion results.....	137
Engineering streptavidin to express an RGD-containing surface loop.....	154
Chapter Summary and Conclusions .....	169
<b>6. SUMMARY AND CONCLUSIONS.....</b>	<b>172</b>
<b>BIBLIOGRAPHY.....</b>	<b>177</b>



## List of Figures

Figure number	Page
1-1: Thiol bond line diagrams.....	5
1-2: Conceptual illustration of a completed mixed self-assembled monolayer.....	6
1-3: Conceptual illustration of surface modification steps.....	8
1-4: Streptavidin adsorption at various surface BAT densities .....	10
1-5: schematic representation of adhesive cell probing surface immobilized molecules.....	12
3-1: Axes of control over surface/protein interactions, determined by selection and proportion of thiols used.....	31
3-2: XPS survey scans of single composition SAMs.....	35
3-3: XPS high resolution carbon spectrum from a pure MHD SAM.....	39
3-4: XPS high resolution carbon spectrum obtained from OEG SAMs.....	41
3-5: XPS high resolution carbon spectrum from pure BAT SAM.....	42
3-6: Comparison of XPS sulfur spectra from pure SAMs.....	45

3-7: Biotin sulfur photoemission spectrum.....	47
3-8: High resolution sulfur spectra from gold and biotin-treated gold surfaces.....	49
3-9: High resolution carbon spectra comparison between gold, biotin-treated gold, and biotin.....	50
3-10: High-resolution nitrogen spectra comparing gold, biotin-treated gold, and biotin.....	52
3-11: Change in gold and oxygen intensity following extensive X-Ray exposure.....	55
3-12: Difference in high resolution carbon spectrum taken from OEG SAMs experiencing different X-Ray exposure times.....	57
3-13: rate of change in O/C ratio of OEG SAMs resulting from X-Ray exposure.....	58
3-14: Correlation between solution and surface thiol ratio for mixed BAT SAMs.....	60
3-15: High resolution XPS carbon spectra from BAT / MHD SAMs .....	63
3-16: Potential orientations of biotin-terminated thiolates to illustrate potential outcomes of ARXPS experiments. ....	66
3-17: Basis for ARXPS composition depth profile measurements.....	68
3-18: ARXPS N/C ratios for different surface compositions of mixed BAT SAMs.....	69
3-19: High resolution sulfur spectra from BAT SAMs.....	72
3-20: Angular dependent XPS oxygen spectra from mixed BAT/MHD SAMs.....	73

3-21: Deconvolution analysis of 100% MHD ARXPS data.....	75
3-22: Deconvolution analysis for 55% BAT / MHD ARXPS data.....	76
3-23: Deconvolution analysis for 100% OEG ARXPS data .....	77
3-24: Composition depth profile deconvolution plot of 45% BAT / OEG SAM.....	78
3-25: Deconvolution analysis for 100% BAT ARXPS data.....	80
3-26: Alternative models for chain packing and bond alignment.....	82
3-27: Angle resolved carbon NEXAFS spectra of MHD SAM.....	83
3-28: NEXAFS spectra of OEG SAMs.....	84
3-29: NEXAFS spectra taken from pure a BAT SAM.....	85
3-30: NEXAFS spectra of mixed BAT / MHD SAM. ....	86
3-31: NEXAFS spectra of mixed BAT / OEG SAM. ....	87
3-32: BAT / OEG SAM film thickness as determined by XPS and SPR.....	89
3-33: Conceptual illustrations of five representative pure and mixed SAMs.....	93
4-1: Schematic illustration of SPR coupling device.....	99
4-2: Ideal SPR reflectivity curves for bulk solution and adsorbed protein layer.....	100
4-3: OEG SAMs prevent streptavidin adsorption .....	102
4-4: MHD SAMs support (non-specific) streptavidin adsorption .....	103

4-5: 85% OEG / 15% BAT surface exposed to 30N osteopontin.....	105
4-6: Comparison of streptavidin adsorption kinetics on different surfaces.....	107
4-7: SPR measurement of streptavidin adsorption to pure BAT SAMs.....	110
4-8: Extended duration SPR adsorption experiment.....	112
4-9: Maximum streptavidin adsorption to mixed composition BAT SAMs .....	113
4-10: Comparison of maximum SA coverage to BAT/SA area ratio.....	114
4-11: Streptavidin mutant W120A is useful for investigating binding avidity.....	118
4-12: W120A dissociation curves for three different BAT / OEG SAM compositions .....	119
4-13: W120A dissociation curves obtained from a representative range of mixed BAT / OEG SAMs using three different SA binding mutants and wild-type.....	120
4-14: Depiction of streptavidin binding modes .....	121
4-15: Demonstrating conditions necessary for assembling engineered protein multilayers .....	124
4-16: Protein multilayers created using collagen as a secondary adsorbate.....	126
4-17: Creating a protein multilayer with a mixture of secondary adsorbates.....	128
5-1: Cell adhesion to protein multilayers requires proper assembly sequence and ligand functionalization.....	138

5-2: Dose-dependency of cell adhesion on 30N coating concentration .....	140
5-3: Phase-contrast photomicrographs of adherent Moav cells at three concentrations and extended time.....	143
5-4: Comparison between cell attachment to 30N coated polystyrene vs. b30N treated BCMs .....	144
5-5: Cell adhesion to immobilized 30N osteopontin is integrin mediated and largely dependent on alpha-v beta-3 expression.....	147
5-6: Cell attachment to immobilized 30N osteopontin is inhibited by addition of soluble GRGDS peptide .....	149
5-7: Comparison of Mo, Moav, and HNB cell adhesion to immobilized 30N osteopontin.....	151
5-8: Comparison of Mo, Moav, and HNB cell adhesion to immobilized bovine collagen I .....	151
5-9: Comparison of cell adhesion to surfaces functionalized with two integrin ligands .....	153
5-10: Two representations of streptavidin dimers showing locations of surface loops .....	156
5-11: Location of surface loop modified to contain RGD peptide.....	157

5-12: Conceptual illustration showing location of RGD peptide loops engineered into core streptavidin and bound to biotin-functionalized SAMs.....	158
5-13: Creating a circularly permuted protein from a tandem gene plus linker.....	160
5-14: Comparison between cell adhesion to immobilized osteopontin and RGD- SA.....	161
5-15: Streptavidin variants expressing RGD peptide promote cell adhesion.....	162
5-16: Cell adhesion to RGD containing streptavidin variants is RGD dependent.....	164
5-17: Cell adhesion to RGD containing streptavidin variants is mediated by alpha- v beta-3 integrin.....	165
5-18: Cell adhesion is determined by uppermost ligand.....	167
5-19: Additional evidence that "uppermost" ligand is responsible for cell attachment.....	167
5-20: Maximum surface density of immobilized SA exceeds cell receptor density by at least 4:1 .....	169

## List of Tables

Table Number	Page
3-1: Elemental composition of thiols (bulk and as assembled) .....	37
3-2: BAT SAM XPS carbon spectrum curve fit values. ....	43
3-3: Peak fit parameters for OEG XPS high-resolution carbon spectra.....	57
4-1: Rate constants determined by fitting data to Equation 7.....	122
4-2: Ratio of streptavidin density to secondary protein adsorbate for collagen I and 30N Osteopontin Fragment .....	127
4-3: Fraction of maximum binding of secondary adsorbates in mixed protein multilayers .....	129
5-1: Integrin receptor expression patterns for Mo, Moav, and HNB18E6E7 cell lines (from (Hu, Hoyer et al. 1995; Smith, Cheung et al. 1996; Smith and Giachelli 1998) .....	136
5-2: Sequence comparison of engineered SA variants expressing an RGD cell adhesion motif.....	158

## Glossary

Some of the terms used in this document refer to specific circumstances or have meanings not commonly encountered in the general literature. Their usage is described below:

assembling solution: the solution that the gold-coated substrate is immersed in to create a self-assembled alkylthiolate monolayer. It generally contains either a single thiol or a mixture of two thiols diluted in absolute ethanol.

biotin containing monolayer: a film (see below) that contains the biotinylated alkylthiolate as one of its components. Abbreviated as BCM.

film: synonymous with *self-assembled monolayer*.

gold interface: meant to describe the “bottom” of the self-assembled monolayer, i.e., the interface between the gold substrate and the sulfhydryl regions of the bound thiolates.

mixed composition: either a solution containing a mixture of exactly two thiol chemistries of defined molar ratio or the self-assembled monolayer created by immersing a gold surface in such a solution.

self-assembled monolayers: in this case, molecular scale films that are generated by adsorption of thiolates from solution onto a gold surface. Abbreviated as SAM.



single thiolate: either a solution containing one type of thiol chemistry or a self-assembled monolayer created from such.

solution ratio: the molar ratio of two thiolates in a mixed assembling solution (total concentration is always held constant at 0.1 mM)

surface: is meant to describe the interface between the “top” of the self-assembled monolayer that would be exposed to solution or to vacuum, depending on the type of analysis or interaction in the context of the statement

surface ratio: the molar ratio of two thiolates in a self-assembled monolayer resulting from immersion of the substrate in a mixed thiol solution. The surface ratio is estimated by a combination of surface measuring techniques

Abbreviations used:

ARXPS – Angle-resolved XPS

BAT – Biotinylated alkyl thiol

BCM – Biotin containing monolayers

OEG – Oligo (ethylene oxide)

MHD – Mercaptohexadecane

NEXAFS – Near edge X-ray absorption fine structure

SAM – Self-assembled monolayer

SPR – Surface plasmon resonance

XPS – X-ray photoelectron spectroscopy

## Acknowledgements

This work would not be possible without the key support of a number of people, and for that at least I shall always be grateful to them. First on the list are Cynthia Atman, Mary Lidstrom, and Robin Adams, who in their infinite patience have allowed me the flexibility to keep up my obligations to them and try to stay abreast of my work on this important project. Another critical source of support came from Scott Coney, who never failed to keep my attention on what needed to be done and was always understanding when I was unable to join him on a back country adventure on account of the my seemingly endless obligations in the laboratory or in front of a computer. Of course, my family: my parents, who have always provided the needed encouragement (if not harassment) to keep the momentum going, and my sibs John and Ingrid, who never ceased to give their confidence that I would succeed. There are, of course many others who showed their support in many different ways, whether from patience, understanding, or encouragement, or who simply put up with me during the trials and tribulations of my life, with the Ph.D. research never far removed from the equation for all these years.

## **Dedication**

Elisabeth, Ethan and Erica

My love for you will endure over all.

## 1. Introduction

Artificial limbs and prosthetic implants have been used for centuries to restore or replace lost function due to trauma, decay, or illness. Originally they may have been simple and strictly functional, such as a wooden peg for a leg, a hook attached to a limb stump, or ivory dentures. More recently the replacement materials are considerably more sophisticated, such as total artificial hip implants, pacemakers, and vascular stents. In comparison to the sensate, dexterous, self-healing originals, these substitutes are only just today approaching their originals in function, longevity and sophistication.

One of the enduring problems to address with these replacements is how to interface them with the biological tissues surrounding the attachment or implantation site. One of the hallmarks of biological systems is an ability to recognize and differentiate “self” versus “non-self” and actively avoid, attack, or reject invasive objects or organisms. The problem with replacement parts or materials becomes, therefore, one of how to “hook them up” and how to avoid the immunological response that inevitably follows.

Alkylthiolate SAMs have long been studied for their ability to control the chemistry and surface properties of an interface (Bain, Evall et al. 1989; Bain, Troughton et al. 1989; Bain and Whitesides 1989; Laibinis, Whitesides et al. 1991; Folkers, Laibinis et al. 1992; Laibinis, Nuzzo et al. 1992; Grunze 1993). They have been characterized by a number of surface analysis methods, either in ultra-high vacuum or using spectroscopic techniques (Porter, Bright et al. 1987; Laibinis, Nuzzo et al. 1992; Rieley, J. et al. 1995;

Zhao, Wilbur et al. 1996). They have been shown to produce complex surfaces if more than one thiolate is co adsorbed onto a surface (Bain, Evall et al. 1989; Bain, Troughton et al. 1989; Bain and Whitesides 1989; Nuzzo, Dubois et al. 1990; Nuzzo, Korenic et al. 1990; Folkers, Laibinis et al. 1992). A great deal of material has been published on the mechanism of formation of these monolayers (Dubois and Nuzzo 1992; Sellers, Ulman et al. 1993; Poirier and J. 1994; Schonenberger, Sondag-Huethorst et al. 1994; Poirier and Pylant 1996; Ulman 1996). They have been shown to have potential for studying the interaction between proteins and surfaces (Prime and Whitesides 1991; Wang, Kreuzer et al. 1997; Harder, Grunze et al. 1998). They have also been shown to serve as supports for the specific binding of streptavidin (Haussling; Haussling, Ringsdorf et al.; Knoll, Liley et al. 1997). The protein streptavidin has unique properties of extremely high binding affinity for biotin and a homotetrameric structure (Green and Joynson; Green and Toms; Green). The utility of self-assembled monolayers for controlling surface chemistry, particularly when using two co adsorbed thiolates, and specifically streptavidin binding, made it an attractive system for immobilizing proteins on surfaces.

Proteins immobilized on biomaterial surfaces are implicated in the response of the body to foreign materials (Epstein and Fukuyama 1989; Tang and Eaton 1993; Tang and Eaton 1995; Tang, Ugarova et al. 1996; Tang, Liu et al. 1998). Controlling these proteins on biomaterial surfaces may be a route to control the wound healing response (Ziats, Miller et al. 1988; Ratner 1993). One problem that remains is identifying the biochemical pathway within the appropriate cell type to exert this control. One key cell

that mediates the inflammatory response to biomaterials is the macrophage (Adams and Hamilton 1984; Haskill, Yurochko et al. 1992; DiPietro 1995; Laskin and Pendino 1995; Hauser 1996), and candidate proteins are those involved in cell adhesion and wound healing (Streuli and Bissell 1990; Gailit and Clark 1994; Raghov 1994; Jackson, Seed et al. 1997). Identifying these proteins is a complex task, though some candidate proteins have been identified, both components of the extracellular matrix (Giachelli, Bae et al. 1993; Beninati, Senger et al. 1994; Liaw, Almeida et al. 1994; O'Brien, Garvin et al. 1994; Schwartz and Boyan 1994; Senger, Perruzzi et al. 1994; Davies 1996; Rollo, Laskin et al. 1996; Senger and Perruzzi 1996) and cell receptor systems, mainly integrins. Controlling the proteins adsorbed to biomaterial surfaces implanted in vivo for controlling wound healing is even more daunting (Tang and Eaton 1993; Tang, Ugarova et al. 1996; Tang 1998; Tang, Liu et al. 1998).

***Specific Aims:***

- 1) Prepare and characterize mixed biotinylated self-assembled monolayers of alkylthiolates on gold designed for controlling streptavidin immobilization.
- 2) Characterize and quantitate streptavidin and secondary protein adsorption to the SAMs generated in (1).

- 3) Characterize and quantitate integrin-mediated cell adhesion to biotinylated, Arg-Gly-Asp containing proteins immobilized on the streptavidin adlayer generated in (2).
- 4) Using optimal surfaces as prepared in (1 - 3), immobilize well-defined lateral surface gradients of biologically relevant secondary proteins using solute dispersion under laminar solution flow.
- 5) Demonstrate, record, and characterize adhesion and haptotactic migration of vascular cells in response to the lateral protein gradients generated in (4).

### ***Experimental System***

#### **General overview of methods used to control surface chemistry and functionality**

The interfacial properties of the model surfaces used in this research were controlled via a method of functionalization that takes advantage of the self-assembly of alkylthiolates on a gold surface. This technique has been shown to provide the capability to control the interfacial chemistry of model surfaces by selectively choosing which end groups are present opposite the sulfhydryl moiety of the alkylthiol molecule. In many cases, mixtures of thiols with different chemistries have been used to achieve more complex interfacial properties than those achievable using single alkylthiols alone. In this study for example, our goal was to create a surface that had a high affinity, high capacity, and high binding specificity for protein streptavidin. To achieve this, a thiol was specially synthesized that was end-functionalized with biotin (Biotinylated alkylthiol,

BAT, see Figure 1-1). In addition to the streptavidin specificity, we desired that our model surface also be resistant to non-specific protein adsorption. To achieve this interfacial property, and to construct comparison surfaces with high non-specific protein adsorption, two thiols were chosen: one end-functionalized with a methyl group (to create a hydrophobic interface), the other end-functionalized with oligo(ethylene oxide), which has been shown in many studies to resist non-specific protein adsorption. Figure 1-1 illustrates the chemical formula and structure of the thiols used in this research.

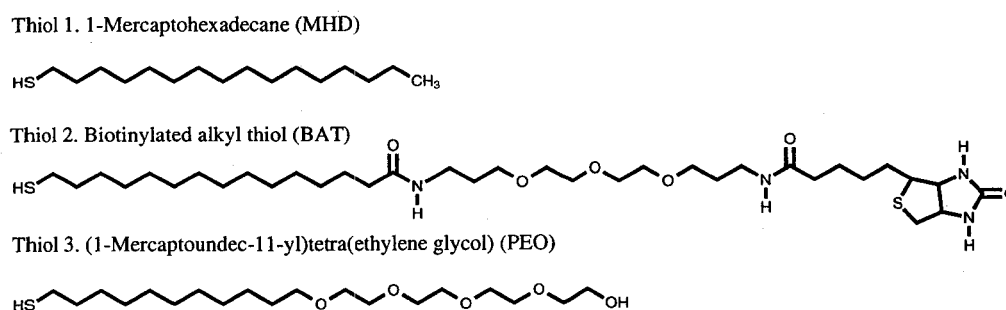


**Figure 1-1: Thiol bond line diagrams**

Each thiol carries an end group that specifies a different functionality to a completed self-assembled monolayer: MHD is hydrophobic, OEG is hydrophilic, and BAT is terminated by biotin, the binding partner of the protein streptavidin.

For the most part, thiols 2 and 3 (BAT and OEG) were used to create surfaces designed to resist non-specific protein adsorption (as a result of the OEG end groups) yet also bind the protein streptavidin with high specificity and affinity (as a result of the biotin end group of BAT).



Similarly to most alkythiols that adsorb onto a gold surface from solution and self-assemble into a close-packed monolayer, it was expected that by exposing a freshly evaporated gold surface to an ethanolic solution containing combinations of the BAT with either the OEG or the MHD thiol would result in a monolayer with a combination of thiolates (and thus surface chemistries), as illustrated in Figure 1-2.

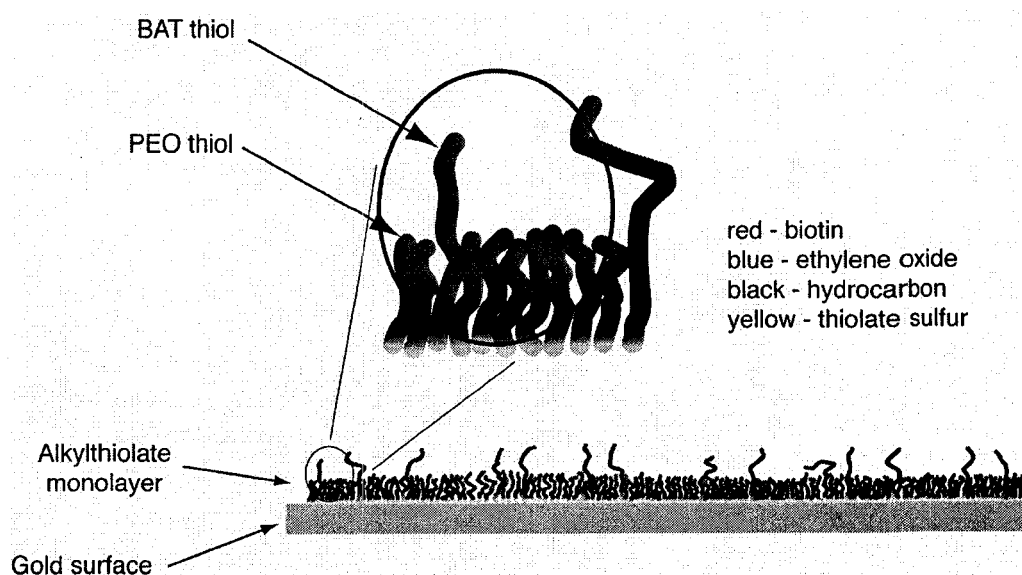


**Figure 1-2: Conceptual illustration of a completed mixed self-assembled monolayer**

The illustration depicts an assembled mixed SAM containing a low surface mole fraction of BAT thiolate relative to the total. The key points are that the sulfur endgroup binds tightly to the gold interface, promoting the directional orientation of the opposite end (terminated in a selected chemistry) toward the new solution/surface interface. This illustration suggests variations in conformations, packing density, and distribution of the minority component.

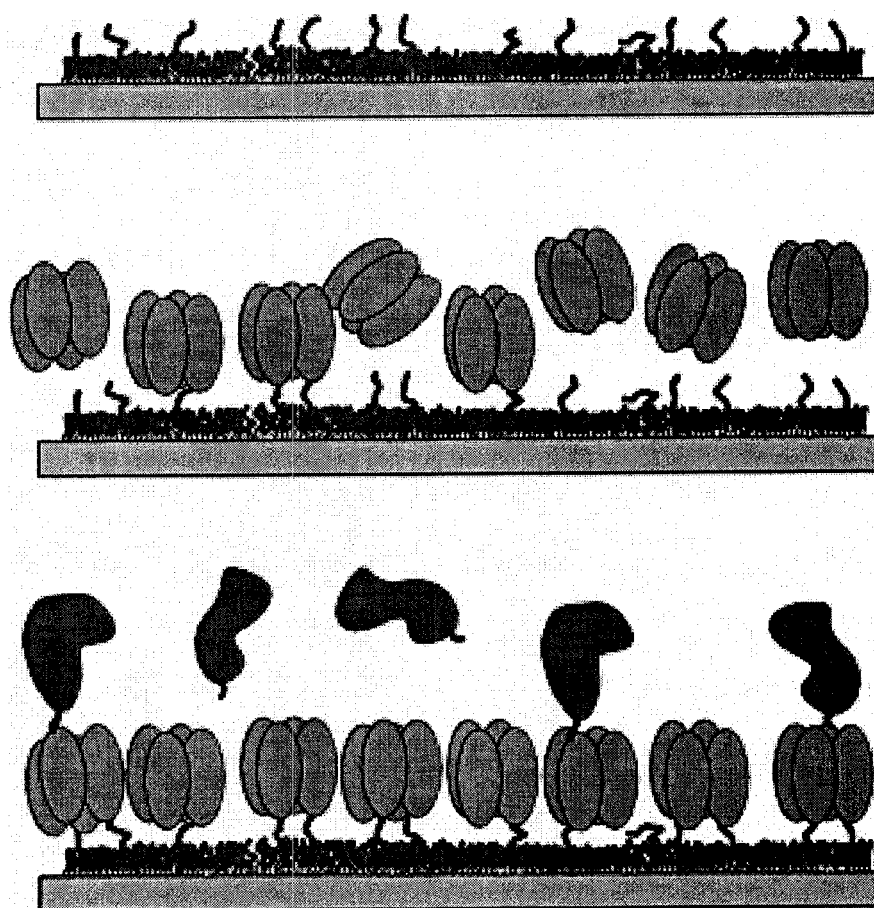
The longer thiols, shown in the figure with a red terminus, represent the BAT thiolates with a biotin end group. The shorter thiols, shown with a blue terminus, represent the OEG thiolates with an ethylene oxide terminal functionality. Whereas the

illustration shows the BAT thiolates relatively well spaced throughout the monolayer, there is no *a priori* reason that this should be the case. While the geometry of streptavidin binding sites suggests an optimum spacing of the thiolates for maximum protein binding with a minimum number of BAT thiolates, the strength of the physisorption of the thiolates and the stochastic nature of the mixed monolayer assembly precludes controlling the optimal distribution of the BAT thiols. Instead, surface optimization for maximum streptavidin coverage and minimum non-selective protein binding is achieved by other means (see Chapter 4). Minimizing the number of BAT thiolates in the monolayer should pay dividends for the non-specific binding properties of the monolayer by maximizing the protein-binding resistant OEG thiolates.

Once the mixed monolayers have been assembled on the surface, it is expected that they bind streptavidin via the biotin-terminated BAT thiol (and, in the case of the mixed BAT / MHD surfaces, to also bind streptavidin non-specifically at a hydrophobic interface). Ideally, these streptavidin-modified surfaces could be used to immobilize essentially any biotin-functionalized protein or small molecule to the surface as depicted in Figure 1-3.

The extremely high affinity of the biotin-streptavidin couple ( $K_d \sim 10^{-13} \text{ M}^{-1}$ , (Green 1975)) combined with the large number of commercially available reagents for conjugating biotin to molecules and the generally minimal impact these conjugation reagents have on the functional activity of the conjugate makes this a convenient,

versatile model system for studying the interactions between surface immobilized molecules and cells in culture.



**Figure 1-3: Conceptual illustration of surface modification steps**

This figure portrays several important steps in the creation of surfaces coated with streptavidin-immobilized cell adhesion ligands: step one (top) the adsorption and assembly of a mixed alkylthiolate monolayer on the gold interface; this first layer can be tailored to control the surface chemistry and protein binding characteristics of the interface, Step two: the binding from solution of streptavidin tetramers; the tetramers can be bound to the alkylthiolate SAM via one or two biotin-terminated alkylthiolates, and Step three: the biotin mediated binding of single or (as shown) several types of cell adhesion ligands.

### **Optimization of streptavidin adsorption by varying surface BAT concentrations**

Using mixed BCMs for streptavidin immobilization as shown in Figure 1-3 raises the possibility of having different interactions between the components of the mixed BCMs and streptavidin. As illustrated in Figure 1-4, different surface densities of the two thiolates in a mixed BCM would be expected to lead to different amounts of adsorbed protein. Furthermore, due to the fact that each streptavidin protein has two adjacent binding sites on two “faces” of the protein (opposite from each other,) there is the strong possibility that some SA molecules may be bound to the surface via one biotin while others are bound via two biotins. (The difference in lengths of the thiols (i.e., BAT:OEG) relative to the size of the SA protein makes it extremely unlikely that the protein is bound to the surface by both biotin binding “faces”.) These different possibilities are shown in Figure 1-4: limiting streptavidin coverage is achieved by either severely limiting the density of the BAT thiols (Figure 1-4, top) or by increasing the BAT concentration to such an extent that the biotin cannot be adequately inserted into the SA binding pocket due to the hindrance of the other nearby BAT molecules (Figure 1-4, bottom.) Optimal SA coverage and stability would be achieved at an intermediate BAT density such that each protein the greatest proportion of the protein is bound to the surface via two biotins, and that the remaining surface is principally characterized by the OEG thiolate, to minimize non-specific or non-selective protein adsorption.

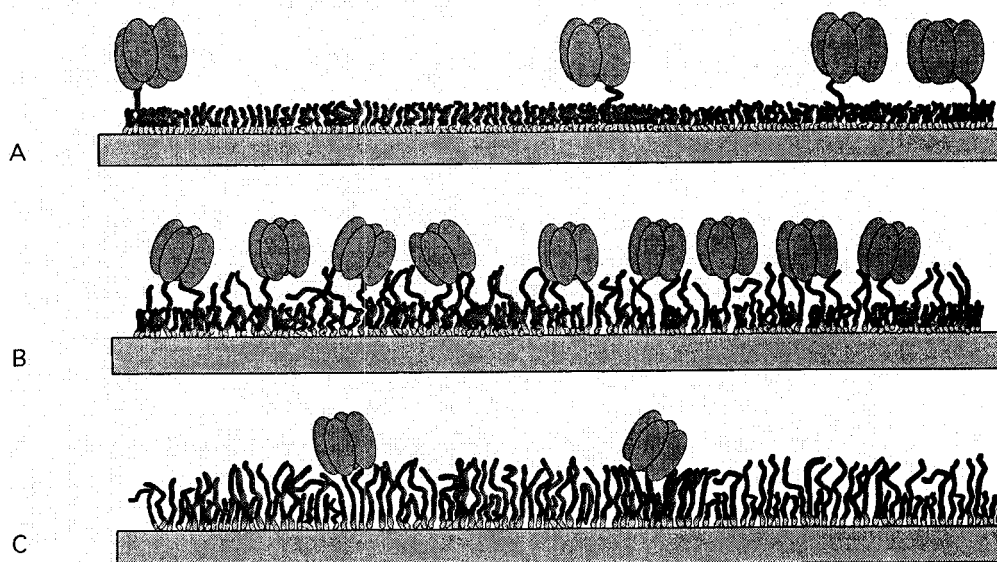


**Figure 1-4: Streptavidin adsorption at various surface BAT densities**

Three different surface/SA binding modes are shown: (A) very low density BAT limits the amount of protein bound to the surface by minimizing the available biotin binding partners, (B) intermediate density BAT coverage increases the protein coverage but still allowing high-affinity binding by allowing the BAT molecules to insert the biotin endgroup into the SA binding pockets, (C) high density BAT coverage prevents high density SA coverage due to steric inhibition to the surface biotin inserting fully into the SA binding pocket before other, non-binding BAT molecules come into contact with the outer surface of the protein.

Of course, Figure 1-3 and Figure 1-4 are idealized representations of what we hoped to accomplish. However, as this surface modification strategy relies on the self-assembly of the thiols shown in Figure 1-1, from solution onto a gold surface, and the BAT and OEG differ markedly from the regular structure and chemistry of the MHD thiol (whose self-assembly properties have been extensively characterized and are quite robust and reproducible), we understood at the outset of these experiments that there were a large

number of unknown physical and chemical parameters that may influence the resulting surface characteristics, which could deviate significantly from our idealized depictions. Thus, verification of the interfacial properties of the self-assembled monolayers of these mixtures of thiolates was a critical foundation for using these surfaces as model systems for protein immobilization, and represents a substantial portion of the research reported herein. The analysis and verification of the surface chemistry resulting from the self-assembly of mixed BAT / MHD and BAT / OEG alkylthiolate monolayers is described in the next two chapters.

### **Cell binding to engineered surfaces**

The principal motivation for carrying out this method of surface engineering is to develop a flexible model system for studying how cells respond to the immobilized molecules, mainly so serve our interests in determining which molecules should be immobilized on biomaterial surfaces in order to direct a desirable wound healing outcome. Figure 1-5 gives a conceptual illustration of how an adherent-dependent cell might specifically recognize the proteins immobilized on the engineered surfaces through its surface-expressed receptors.

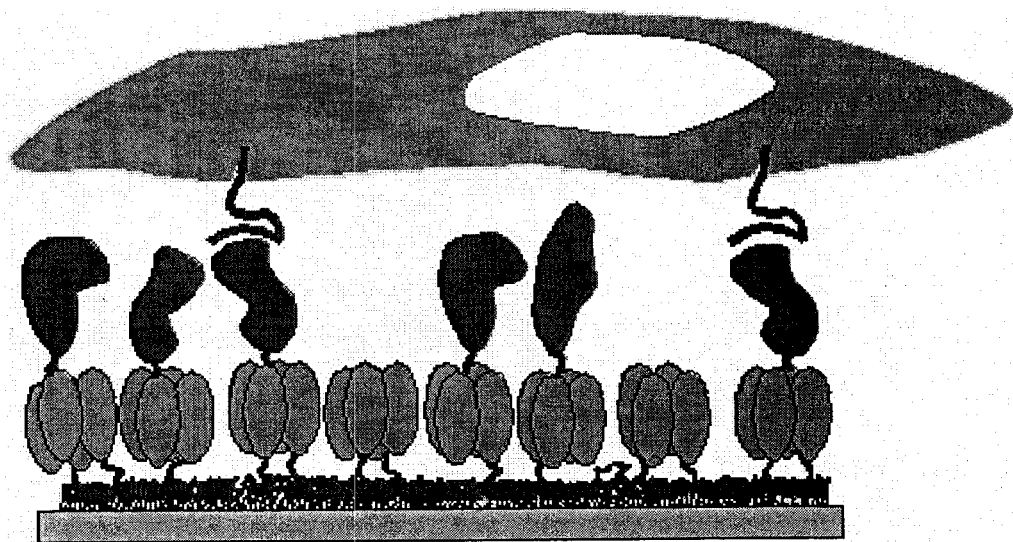


**Figure 1-5: schematic representation of adhesive cell probing surface immobilized molecules**

The components of the engineered surface is recognizable from the first four illustrations. Shown here is an idealized nucleated cell (not to scale) interacting directly with two immobilized molecules via surface-expressed receptors (red). No other interactions between the surface and the cell are represented in the diagram, though additional immobilized molecules (ochre) could stimulate cell response should the cell express cognate receptors (not shown).

The experiments described in this body of work show how this surface engineering method can be used to control the identity and amount of proteins at a gold interface, and that the immobilized proteins alone support cell adhesion. In short, we have developed, characterized, and verified a versatile method for rapid, specific, high-affinity surface immobilization of proteins for studying how they influence adherent cell behavior.

## 2. Materials and Methods

### *Organic Synthesis*

The organic synthesis of the BAT and OEG thiols was carried out as follows:

**Synthesis of Biotinylated Alkyl Thiol (BAT).** All reagents, solvents and chemicals were purchased from Aldrich and Baker. Triethylamine (TEA) was distilled from ninhydrin to remove primary and secondary amines before use. Dimethylformamide (DMF) and methylene chloride were dried by distillation from magnesium sulfate and calcium hydride, respectively. All other solvents and chemicals were used as received. NMR spectra were obtained with a Bruker AF300 or a Bruker AC200 instrument. Infrared spectra were recorded on a Perkin Elmer 1600 series FT-IR. Mass spectra were obtained using a Kratos Profile HV3 electron impact mass spectrometer with a direct probe for sample introduction, or a Kratos Profile HV4 electrospray mass spectrometer. A 50% methanol/water solvent was used for ES-MS and gramicidin was the internal standard.

*Synthesis of biotin tetrafluorophenyl ester (2):* Biotin, **1**, (505.4 mg, 2.1 mmol) and 2,3,5,6-tetrafluorophenol (450.9 mg, 2.7 mmol) were dissolved in 10 ml of anhydrous DMF at 70°C under nitrogen. After cooling to room temperature 1,3-dicyclohexylcarbodiimide (DCC) (504.9 mg, 2.5 mmol), dissolved in 3 ml of dry DMF, was added to the reaction mixture and the reaction was heated to 70-80°C for 4 hours.



The solvent was removed under reduced pressure and the resulting white residue was triturated with ether to remove residual tetrafluorophenol. Substantial amounts of dicyclohexylurea (DCU) can be removed by sonicating the residue several times with acetone, where the product dissolves in the acetone and DCU remains behind. After evaporation of the acetone, the crude product was purified by flash column chromatography on silica gel using 9:1 methylene chloride:methanol to yield biotin tetrafluorophenyl ester, **2** (575.5 mg, 62 %, mp 185.5-186.5°C). <sup>1</sup>H-NMR (CDCl<sub>3</sub>, 200 MHz): δ 1.4-1.9 (m, 6H), 2.73 (m, 3H), 2.95 (dd, 1H), 3.21 (m, 1H), 4.34 (dd, 1H), 4.54 (dd, 1H), 5.1 (bs, 1H), 7.00 (m, 1H); FT-IR (KBr, cm<sup>-1</sup>): 3250, 2931, 2860, 1795, 1702, 1525, 1484, 1179, 1096, 955

*Synthesis of N-(13-amino-4,7,10-trioxatridecanyl)biotinamide (3)<sup>1</sup>*: 4,7,10-Trioxa-1,13-tridecanediamine (1.24 ml, 4.7 mmol) and freshly distilled triethylamine (TEA) (0.20 ml, 1.4 mmol) were dissolved in 6 ml anhydrous DMF. The reaction mixture was cooled on ice and biotin tetrafluorophenyl ester, **2**, (210.0 mg, 0.54 mmol, dissolved in 6 ml dry DMF) was added over a period of 45 min under nitrogen. The reaction was then stirred for 1 hour at room temperature and the solvent was removed under reduced pressure. The resulting oil was triturated with ether to remove tetrafluorophenol and residual diamine to yield **3** as a sticky white residue (84 mg, 72%, mp 104-105.5°C). <sup>1</sup>H-NMR (CDCl<sub>3</sub>, 200 MHz): δ 1.47 (m, 2H), 1.6-1.9 (m, 8H), 2.23 (m, 1H), 2.38 (m, 1H), 2.71 (d, 1H), 2.91 (dd, 1H), 3.01 (t, 1H), 3.15 (m, 1H), 3.2-3.5 (m, 3H), 3.62 (m, 12H), 4.35

(dd, 1H), 4.48 (dd, 1H); FT-IR (thin film,  $\text{cm}^{-1}$ ): 3296, 2931, 2860, 1701, 1643, 1555, 1461, 1325, 1108

*Synthesis of 16-bromohexadecanoic acid (5)*<sup>2</sup>: 16-Hydroxyhexadecanoic acid, **4**, (5.300 g, 19.5 mmol) was refluxed in 70 ml of a 1 : 1 mixture of 48% hydrobromic acid and glacial acetic acid for two days. Upon cooling the product precipitated and was filtered and washed with deionized water. The crude 16-bromohexadecanoic acid was recrystallized from hot hexane to yield white shiny flakes (5.782 g, 88%, mp = 69.5-70°C). <sup>1</sup>H-NMR ( $\text{CDCl}_3$ , 200 MHz):  $\delta$  1.26 (bs, 22H), 1.63 (m, 2H), 1.86 (m, 2H), 2.35 (t, 2H), 3.41 (t, 2H); FT-IR (KBr,  $\text{cm}^{-1}$ ): 2917, 2850, 1696, 1472, 1289, 1249, 1210, 918

*Synthesis of 16-benzoylthiohexadecanoic acid (6)*<sup>3</sup>: To 30 ml of degassed absolute ethanol, sodium metal (83.1 mg, 3.61 mmol) and thiobenzoic acid (0.53 ml, 4.50 mmol) were added. This sodium thiobenzoate solution was added over a period of 10 min to 16-bromohexadecanoic acid, **5**, (1.0243 g, 3.05 mmol), dissolved in absolute ethanol (10 ml). The reaction mixture was stirred at room temperature for two hours and then heated at 85-88°C for 1 hour. The mixture was then cooled to room temperature and the solvent was evaporated. The resulting residue was taken up in ethyl acetate and extracted once with water. The aqueous layer was extracted with ethyl acetate and the organic layers were combined and washed once with sat.  $\text{NaCl}_{(\text{aq})}$ , dried over anhydrous magnesium sulfate, filtered and the solvent was evaporated. The crude product was recrystallized from hexane to yield light maroon flakes of **6** (1.102 g, 92 %, mp = 72.5-73.2°C). <sup>1</sup>H-

NMR (CDCl<sub>3</sub>, 300 MHz):  $\delta$  1.26 (m, 22H), 1.65 (m, 4H), 2.35 (t, 2H), 3.07 (t, 2H), 7.44 (dd, 2H), 7.56 (dd, 1H), 7.97 (dd, 2H); FT-IR (thin film, cm<sup>-1</sup>): 2919, 2849, 1702, 1655, 1467, 1443, 1408, 1290, 1208; MS (EI, m/z): 410 [M+H<sub>2</sub>O]<sup>+</sup>, 431 [M+K]<sup>+</sup>

*Synthesis of 2',3',5',6'-tetrafluorophenyl-16-benzoylthiohexadecanoate (7):* 16-Benzoyl-thiohexadecanoic acid, **6**, (955.6 mg, 2.43 mmol) and tetrafluorophenol (489.2 mg, 2.95 mmol) were dissolved in 15 ml freshly distilled methylene chloride. To this mixture DCC (545.5 mg, 2.64 mmol), dissolved in 5 ml methylene chloride, was added. After 5 minutes the formation of a white precipitate (DCU) was observed. The reaction was allowed to proceed for an additional 1.5 hours. The precipitate was filtered and the filtrate was concentrated under reduced pressure. The resulting residue was taken up in hot methanol and the insoluble impurities were filtered off. Upon cooling **7** crystallized and was collected by filtration to yield off-white crystals (1.2915 g, 98%, mp = 64.8-67°C). <sup>1</sup>H-NMR (CDCl<sub>3</sub>, 200 MHz):  $\delta$  1.27 (bs, 22H), 1.76 (m, 4H), 2.66 (t, 2H), 3.07 (t, 2H), 3.98 (tt, 1H), 7.44 (dd, 2H), 7.55 (dd, 1H), 7.97 (dt, 2H); FT-IR (KBr, cm<sup>-1</sup>): 3323, 2916, 2856, 1788 (C(=O)OR), 1656 (C(=O)SR), 1626, 1519, 1489, 1196, 1171, 1088

*Synthesis of biotinylated alkyl thiobenzoyl (8):* Under nitrogen, 2',3',5',6'-tetrafluorophenyl-16-benzoylthiohexadecanoate, **7**, (347.5 mg, 0.778 mmol) and N-(13-amino-4,7,10-trioxatridecanyl)biotinamide, **3**, (177.2 mg, 0.328 mmol) were dissolved in 20 ml anhydrous methylene chloride and the solution was heated briefly to dissolve the

biotin conjugate. After cooling to room temperature, 62  $\mu$ l (0.445 mmol) of freshly distilled triethylamine was added and the reaction mixture was stirred at room temperature. After 45 hours the solvent was evaporated under vacuum and the white residue was dissolved in hot methylene chloride and precipitated with cold hexane. The precipitate was filtered and washed with cold hexane to yield **8** (102.8 mg, 69.2%).  $^1\text{H-NMR}$  ( $\text{CDCl}_3$ , 300 MHz):  $\delta$  1.25 (bs, 22H), 1.46 (m, 2H), 1.68 (m, 4H), 1.78 (m, 8H), 2.21 (t, 2H), 2.25 (t, 2H), 2.77 (d, 1H), 2.93 (dd, 1H), 3.07 (t, 2H), 3.17 (dt, 1H), 3.35 (bt, 4H), 3.57 (m, 4H), 3.62 (m, 8H), 4.35 (dd, 1H), 4.54 (dd, 1H), 7.44 (dt, 2H), 7.56 (t, 1H), 7.97 (dd, 2H); FT-IR (KBr,  $\text{cm}^{-1}$ ): 3311, 2917, 2849, 1696, 1661, 1637, 1549, 1472, 1449, 1208, 1114

*Synthesis of biotinylated alkyl thiol (BAT, 2)*<sup>4</sup>: To biotinylated alkyl thiobenzoyl, **8**, (86.0 mg, 0.105 mmol) 10 ml of 2M NaOH in methanol (20 mmol) were added while stirring under nitrogen. The solution was briefly heated to dissolve all of the starting material, then it was allowed to stir at room temperature. The reaction was discontinued after 15 minutes by slowly adding 6M  $\text{HCl}_{(\text{aq})}$  until a pH of about 4 was reached. A slight color change was noticed when going from basic (light yellow) to neutral (light brown) to acidic (colorless) conditions. The solvent was evaporated and the residue was washed well with deionized water and ether to remove the side products to yield biotinylated alkyl thiol, **2** (70.5 mg, 94%).  $^1\text{H-NMR}$  (MeOD, 300 MHz):  $\delta$  1.24 (s, 22H), 1.39 (m, 2H), 1.55-1.70 (m, 12H), 2.11 (t, 2H,  $J = 7.7$  Hz), 2.14 (t, 2H,  $J = 7.5$  Hz),

2.43 (t, 2H,  $J = 7.3$  Hz), 2.65 (d, 1H,  $J = 12.8$  Hz), 2.87 (dd, 1H,  $J = 12.7, 4.9$  Hz), 3.13 (dt, 1H, 4.4 Hz), 3.20 (2t, 4H,  $J = 6.8, 6.8$  Hz), 3.46 (2t, 4H,  $J = 6.3, 6.1$  Hz), 3.56 (m, 8H), 4.24 (dd, 1H,  $J = 7.8, 4.4$  Hz), 4.43 (dd, 1H,  $J = 7.9, 4.9$  Hz); FT-IR (KBr,  $\text{cm}^{-1}$ ): 3413, 3319, 2919, 2849, 1694, 1637, 1546, 1472, 1126; MS (ES,  $m/z$ ): 739  $[\text{M}+\text{Na}]^+$ , 247  $[\text{M}+2\text{H}+\text{Na}]^{3+}$

**Synthesis of (1-Mercaptoundec-11-yl)tetra(ethylene glycol).** undec-10-enyl bromide(Lancaster, 97%), tetrethylene glycol (Aldrich, 98%), thiolacetic acid( Aldrich, 99%), 1,1' azobis-(cyclohexanecarbonitrile) ( Aldrich, 99%), all other chemicals were reagent grade from Aldrich. The chemicals were used as received. Preparative TLC plates, C18-silica gel, (Aldrich, 20x20 cm, 1000 microns)

*Synthesis of Undec-1-en-11yltetra(ethylene glycol) I.* A mixture of 50% aqueous sodium hydroxide ( 21 mmol, 1.68 ml) and tetrethylene glycol (10 mmol, 1.94 gr.) was stirred for about 1 hour in an oil bath at 100 C under nitrogen. To above mixture was added undec-10-enyl bromide (21 mmol, 4.89 gr.), and the reaction continued. After 16 hours, the reaction mixture was cooled and extracted 5 times with heptane. Removal of heptane under reduced pressure gave a yellow oil. This oil was purified by column chromatography on silica gel ( eluent: ethyl acetate) gave 2.69 gr. of the product in 78% yield;  $^1\text{H}$  NMR (300 MHz,  $\text{CDCl}_3$ )  $\delta$  1.3(br s, 12 H), 1.55 (q, 2 H,  $J = 7$  Hz), 2.0 (q, 2 H,  $J = 7$  Hz), 2.85 (br s, 1 H), 3.4 (t, 2 H,  $J = 7$  Hz), 3.45-3.75 (m, 16 H), 4.9-5.05 (m, 2 H), 5.75-5.85 (m, 1 H). IR (neat)  $\nu_{\text{max}}$  3450, 2900, 2840, 1100  $\text{cm}^{-1}$ .

*Synthesis of [1-[(Methylcarbonyl)thio]undec-11-yl]tetra(ethylene glycol) II.* A solution of **I** (5 mmol, 1.73 gr.) in methanol (15 ml) and thiolacetic acid (20 mmol, 1.52 gr.) and radical initiator 1,1' azobis-(cyclohexanecarbonitrile) (5 mg) were irradiated for 10 hours nitrogen with a 450-W, medium pressure mercury lamp. The mixture was concentrated on rotary evaporator at reduced pressure to give 1.7 gr. of product in 81% yield. <sup>1</sup>H NMR (300 MHz, CDCl<sub>3</sub>) δ 1.25(br s, 15H), 1.6 (m, 4 H), 2.3 (s, 3 H), 2.85 (t, 2 H, *J* = 7 Hz), 3.45 (t, 2 H, *J* = 7 Hz), 3.45-3.75 (m, 16 H). IR (neat)  $\nu_{\max}$  3450, 2900, 2840, 1700, 1100 cm<sup>-1</sup>.

*Synthesis of (1-Mercapto)undec-11-yl]tetra(ethylene glycol) III.* To 50 ml solution of 0.1 M HCl in methanol was added compound **II** (1.5 gr., 3.5 mmol). The mixture was refluxed under an atmosphere of nitrogen for 6 hours. Concentration of the reaction mixtures by rotary evaporation at reduced pressure followed by purification of the residues by chromatography on preparative TLC plates C18-silica gel and acetonitrile as mobile phase gave 910 mg of product in 68% yields. <sup>1</sup>H NMR (300 MHz, CDCl<sub>3</sub>) δ 1.2 (br s, 14 H), 1.3 (t, 1 H, *J* = 7 Hz), 1.5 (m, 4 H), 2.5 (q, 2 H, *J* = 7 Hz), 2.85 (br s, 1 H), 3.4 (t, 2 H, *J* = 7 Hz), 3.55-3.75 (m, 16 H). IR (neat)  $\nu_{\max}$  3450, 2900, 2840, 1100 cm<sup>-1</sup>. Mercaptohexadecane was purchased from Aldrich (92% purity) and used without further purification.

All thiol reagents were stored at -20°C (OEG and MHD are liquids at room temperature and were flushed with nitrogen before storage.) Stock 1 mM thiol solutions

were stored under nitrogen at  $-20^{\circ}\text{C}$  until needed. Stock solutions were stored for up to six months before discarding the unused portions.

### *Alkylthiolate Monolayer Preparation*

#### **Substrate preparation**

All non-polymer substrates were cleaned before use with RBS (Pierce) according to the manufacturer's directions. Briefly, a working concentration of RBS was made (1 part RBS to 20 parts hot tap water ( $\sim 50^{\circ}\text{C}$ )). The glass or silicon substrates were soaked in this solution 2-12 hours, then generously rinsed with cold tap water, deionized water, then absolute ethanol (McCormick). Substrates were blown dry under a nitrogen stream, then baked in a vacuum oven ( $<1''$  Hg,  $\sim 50^{\circ}\text{C}$ ) overnight. After venting the oven, the substrates were allowed to cool to room temperature and used without further treatment. Tissue culture substrates (Falcon or Corning), generally 24 or 96 well plates, were used as provided by the manufacturer without further treatment.

#### **Gold evaporation**

Gold evaporation was performed at the University of Washington in one of three locations: 1) the Electrical Engineering Department (Bruce Darling's equipment), 2) the Physics Department (glass shop), or 3) the Center for Nanotechnology (located in the Washington Technology Center's clean room facility). All evaporation equipment was used essentially as follows: After loading the clean substrates, the chamber was evacuated to a pressure of  $\sim 1\text{e-}6$  torr.  $20 \text{ \AA}$  of either a chromium or titanium (Alfa Aesar)

adlayer was deposited at a rate of  $\sim 5 \text{ \AA}/\text{sec}$ . Gold beads (Alfa Aesar, 99.9999% metals basis) were heated in a molybdenum crucible using an 8 KV electron beam at a current sufficient to achieve a rate of  $\sim 1\text{-}2 \text{ \AA}/\text{sec}$  until  $\sim 500 \text{ \AA}$  material had been deposited. The chamber was then allowed to cool for  $>15$  minutes before venting with nitrogen. The coated substrates were stored in a desiccating chamber at ambient pressure to minimize exposure to the ambient lab atmosphere.

Occasionally, the gold-coated substrates were used after an extended period of storage ( $>2$  weeks.) In these cases, adventitious contaminants would accumulate on the gold surfaces. This would be evidenced by the contact angle of water on the surface: the “clean” gold would be fully wet (contact angle  $<5$  degrees), whereas on “contaminated” gold, the water contact angle would be visibly higher ( $<90$  degrees). In other words, the water would either “sheet” or “bead.” In the latter case, if used as-is, the substrates would not support alkylthiolate self-assembly (unpublished XPS results) To minimize the waste of reagents and maximize the number of substrates that could be coated in one evaporator run, the following cleaning protocol for the contaminated gold surfaces was used.

### **Gold substrate cleaning**

This procedure was carried out in a chemical containment / fume hood for operator safety. A solution of ammonium hydroxide ( $\text{NH}_4\text{OH}$ ) at stock concentration was mixed with concentrated hydrogen peroxide ( $\text{H}_2\text{O}_2$ , 33%) and deionized water at a ratio of 1:1:5. (Care was taken to store the hydrogen peroxide at  $4^\circ\text{C}$  to maintain concentration and



activity.) A wide-mouth beaker with just enough volume to immerse the gold substrate was filled with this cleaning solution. The beaker was suspended in a clamp such that the liquid-filled portion was itself immersed in a larger beaker containing tap water. The lower beaker rested on a combination hot plate / stirrer apparatus. A small stir bar was added to the lower beaker and a Celsius thermometer was arranged such that it too was immersed in the bulk of the liquid in the lower beaker (i.e., not resting on the bottom.) This “double-boiler” setup was used to heat the cleaning solution liquid to between 50° and 60°C. A fresh cleaning solution at this temperature would effervesce slightly by itself and bubble vigorously when a contaminated gold substrate was immersed in it. The gold substrates were soaked in this hot cleaning solution for up to 10 minutes, monitoring the action carefully to ensure the gold coating was not removed from the substrate in the process or that the bubbling action on the surface of the gold visibly decreased. The substrates were then removed from the cleaning solution and rinsed with deionized water, then ethanol, then immersed directly into the thiol solution for monolayer self-assembly. If, after removing the gold substrate from the cleaning solution, the aqueous rinse showed that the water was still beading on the gold surface, the substrate would be returned to the cleaning solution. If the gold had been treated in this way for >10 minutes with no visible improvement in its wetting properties, the surface would be discarded. This cleaning solution would be active for no more than ~20 minutes before bubbling ceased, at which point it was cooled and discarded.

### **Cutting gold substrates**

It was often necessary to cut the larger substrates coated in the evaporation chamber into smaller sections for XPS or SPR measurements. This was accomplished with glass slides by simply inverting the substrate onto a clean, soft tissue and scoring the underside lightly once with a diamond scribe. This scored substrate would generally snap easily along the scoring by holding the edges of the slide with gloved fingers and bending it. If performed carefully, these substrates were used without further treatment.

### **Thiol Solution preparation**

Absolute ethanol used to dissolve the thiols was first degassed by bubbling nitrogen through for >20 minutes. Thiol compounds were removed from storage, allowed to reach room temperature, then weighed. Generally, ~3mg solid BAT was weighed; this and the amount of ethanol needed make a 1 mM solution using the actual amount of BAT measured was added to a polypropylene screw-top container (FW BAT = 717.54 gm/mol) This mixture was then placed into a sonicator bath and sonicated for ~10 minutes (clean/degas setting) until the majority of the BAT solids were dispersed. BAT is poorly soluble in ethanol so stock solutions that had been stored for some time were re-sonicated to break up any precipitate that may have formed. OEG and MHD thiol solutions were crafted similarly, except that in this case the thiols were liquids at room temperature (and needed to be melted after removing from storage) and the amounts were measured using an adjustable pipettor and adding them to a clean, dry polypropylene jar

stationed on a tared scale. In contrast to the BAT thiol, both the OEG and MHD thiols were readily soluble in ethanol so no sonication was needed.

Sufficient volumes of these 1 mM solutions were added to the polypropylene jars large enough to accommodate the substrates being used to achieve the desired solution thiol ratio at a final total thiol concentration of 0.1 mM. For example, if the bottles used for assembly would contain a final volume of 10 mL (it was found that 120 mL jars were large enough to accommodate microscope-slide-sized substrates, and that the reagent volume necessary to fully immerse the slides could be minimized by placing the bottles on their sides) and the solution thiol ratio desired was 90% OEG / 10% BAT, 100  $\mu$ L of the 1 mM BAT stock solution and 900  $\mu$ L of the OEG stock solution was added to 9 mL of degassed absolute ethanol.

### **Thiolate monolayer assembly**

Clean gold substrates were rapidly immersed in the thiol solutions such that the substrate would be “face-down” if the bottle were placed on its side. These solutions were stored under nitrogen during assembly by flushing the bottles with a nitrogen stream. Assembly was allowed to continue overnight, although occasionally assembly would be allowed to continue much longer (up to 4 days.) Substrates were then removed, rinsed with absolute ethanol and blown dry under a nitrogen stream or for hydrophobic surfaces first rinsed in hexanes and then ethanol, and dried under Ar or N<sub>2</sub>. Drying the substrates using this means was best accomplished by blowing at an oblique angle across the surface to “chase” the liquid off the surface. If the surfaces were blown dry with the

stream perpendicular to the surface normal, visible residues would usually be noted.

Should this occur, the substrates would be re-immersed in the assembling solution for >1 hour, then again removed and rinsed so that no residue remained.

### **Surface handling and storage**

Surfaces with completed alkylthiolate monolayers were used immediately for surface analysis or protein adsorption. Generally speaking, substrates would be transported between laboratory settings in a plastic Petri dish wrapped in aluminum foil to minimize exposure to UV radiation. Little care was taken to protect the alkylthiolate monolayers from ambient conditions (atmosphere, humidity, etc.) other than light and general surface contamination. Surfaces that could not be used within ~24 hours were discarded.

### ***Thiolate Monolayer Surface Analysis***

**XPS Measurements.** XPS measurements were made at the University of Washington NESAC/BIO surface analysis facility using a monochromatic Al K<sub>α</sub> X-ray source as described previously (Nelson, Gamble et al. 2001). Briefly, initial survey scans (0 - 1000 eV binding energy) were followed by detailed scans for carbon, gold, nitrogen, oxygen, and sulfur (150 eV detector pass energy, 20 eV windows, centered at 285, 84, 400, 532 and 161 eV binding energy, respectively). High-resolution sulfur spectra were collected essentially as described above except that the detector pass energy used was 50 eV, while the high-resolution carbon spectra were collected with a detector pass energy of either 50 eV or 25 eV. Angle-resolved XPS spectra were collected using the

instrument parameters described above at take-off angles  $\theta$  of 0, 39, 55, 68, and 80 degrees between the detector lens axis and the sample surface normal, with a 12 degree aperture placed over the analyzer lens. The number of scans taken at different angles was adjusted to optimize the signal-to-noise ratio while minimizing x-ray induced sample damage to the OEG thiolates, which were found to be susceptible to beam damage as indicated by a decrease in oxygen percentage in survey scans taken before and after composition analysis (data not shown). To provide a clean Au reference signal for XPS thickness measurements, a freshly prepared gold surface was sputtered in the XPS analytical chamber for 5 minutes under Xe ( $3 \times 10^{-7}$  torr) with an accelerating voltage of 1 keV. The C1s signal was measured after the first 3 minutes of sputtering, then every minute thereafter until the carbon signal no longer decreased upon further etching. Unconstrained least squares fitting of the XPS thickness data to the equation derived in the text (Eq. 6, below) using a chi-square minimization algorithm with  $N_{\text{tot}}^{\text{D}}$ ,  $N_{\text{tot}}^{\text{B}}$ ,  $V_{\text{D}}$ , and  $V_{\text{B}}$  as fitting parameters and the surface mole fraction of BAT ( $\chi_{\text{B,sur}}$ ) as the dependent variable is shown and described in detail in the text.

**Near Edge X-ray Absorption Fine Structure (NEXAFS).** The near edge x-ray absorption fine structure experiments were done at the National Synchrotron Light Source U7A beamline located at Brookhaven National Laboratory. This beamline uses a monochromator and 30/30 slits which gave a full-width at half-maximum resolution of  $\sim 0.15$  eV at the carbon K-edge ( $\sim 285$ eV). The monochromator energy scale was calibrated by setting the peak for the C1s $\rightarrow\sigma^*$  transition in the graphite carbon K-edge

NEXAFS spectrum to 285.35 eV (Nelson, Gamble et al. 2001). All NEXAFS spectra were normalized by the photocurrent from a gold coated, 90% transmission grid placed in the incident X-ray beam. Partial electron yield (PEY) was measured by a channeltron with the cone negatively biased (-100 to -150 eV). Rotation of the sample changed the angle ( $\phi$ ) between the x-ray beam and the sample surface. Normal incidence of the x-ray beam on the surface corresponds to a polar angle of  $90^\circ$ , while glancing incidence x-ray beam corresponds to a polar angle of  $20^\circ$ . This definition of the polar angle for NEXAFS should not be confused with the definition of the XPS photoelectron takeoff angle. The electric field vector (E) is perpendicular to the x-ray beam, such that for normal incidence, the E vector of the x-ray beam lies parallel to the surface.

#### **ARXPS data deconvolution analysis**

Depth profile deconvolution analysis using Bonnie Tyler's algorithm has been described previously (Tyler, Castner et al. 1989; Tyler, Castner et al. 1989). See these references for details.

#### ***SPR measurements***

The SPR system used here has been described and characterized previously (Jung, Campbell et al. 1998). Briefly, the SPR measurements of protein adsorption were performed by index-matching the SAM functionalized sample slide to the coupling prism under a Plexiglas flow cell essentially consisting of a silicone gasket that creates an 80  $\mu$ l channel. One ml samples of degassed buffer solution (0.15 M PBS at pH 7.4) were

delivered to the sensor surface at a rate of 10 ml / min. Once the baseline resonance wavelength stabilized, the buffer above the sample was rapidly exchanged with PBS (1.25 ml at 10.0 ml / min) containing 0.1 or 0.05 mg/mL recombinant core streptavidin. After injection the flow was stopped and the protein sample was allowed to remain in contact with the surface. A shift in the coupling wavelength was indicative of protein binding to the surface as discussed in (Jung, Campbell et al. 1998). The absolute wavelength shift of the SPR minimum was converted into protein coverage in  $\text{ng}/\text{cm}^2$  according to the formalism presented in (Jung, Nelson et al. 1999). The wild-type streptavidin/biotin off-rate is too slow for competitive dissociation to be measured over the time scale of SPR, so the desorption kinetics of engineered streptavidin binding mutants with decreased affinity for biotin was studied instead. To initiate desorption (competitive dissociation) of these mutants after their adsorption on a SAM, a PBS solution containing an excess of biotin (1.0 mM) was injected into the flow cell, while monitoring the resulting decrease in SPR wavelength (protein coverage).

### **Protein binding quantitation**

The SPR response of the device used for protein binding experiments has been calibrated to changes in refractive index at the substrate/solution interface as described previously (Jung, Campbell et al. 1998) The amount of protein that bound to a surface was calculated based on this calibration and the known refractive index for this class of proteins (1.55.) The film thickness was thus determined from the change in the SPR minimum wavelength as follows: (Jung, Campbell et al. 1998)

Protein coverage was determined by converting this film thickness to the amount of protein in ng/cm<sup>2</sup> based on the known molecular weight of the protein as follows:

### ***Cell culture***

#### **General cell growth maintenance**

Generally accepted laboratory safety precautions were exercised for all cell culture experiments (biological containment hood, personal protective equipment, sterilization and decontamination procedures, etc.)

Adhesion-dependent M21-derived human melanoma cells (Mo and Mo $\alpha_v$ ) were grown in tissue culture flasks (Corning or Falcon) in Dulbecco's Modified Essential Medium (DMEM) fortified with 10% fetal calf serum (various sources), 5 mM L-glutamine and 1mM each of penicillin / streptomycin, in a water-jacketed incubator at 37°C, 95% RH, 5% CO<sub>2</sub>. Cells were passaged 1:3 to 1:5 at confluence (generally every 3 – 4 days.) Unused cells were discarded in 10% bleach solution.



### **3. Alkylthiolate Monolayer Assembly and Characterization**

The overall objectives of these first experiments were to create and characterize alkylthiolate molecular monolayers on gold substrates that would affect control over the chemistry and therefore the relevant protein binding properties at the interface. There were two principle surface properties to be controlled: 1) the propensity of the surface to promote or resist non specific protein binding and 2) the propensity of the surface to specifically (i.e., mediated by biotin) bind streptavidin from solution (see Figure 3-1).

Control over the interfacial chemistry was achieved by varying the identity and proportion of the thiols in the solution used for monolayer preparation. With the exception of “pure” or single-composition monolayers used as test cases for surface analysis, biotin-containing monolayers (BCMs) were prepared with two thiols (“binary” composition monolayers), one thiol for control over each of the two axes shown in Figure 3-1.

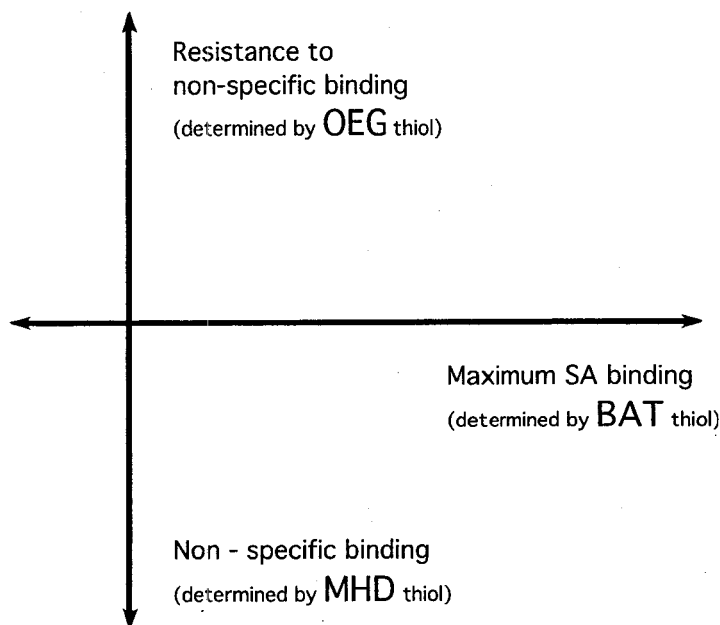


**Figure 3-1: Axes of control over surface/protein interactions, determined by selection and proportion of thiols used.**

The two axes shown represent two fundamental surface properties that need to be controlled to achieve our objectives of controlling the interaction between cells and proteins on a surface: non-specific and selective protein adsorption. See text for details.

For the purposes of this research, the protein that was specifically adsorbed was streptavidin. The amount of streptavidin that may be specifically adsorbed to the surface was expected to be determined by the proportion of the biotinylated thiolate on the surface. The proportion of BAT in the surface monolayer was itself be controlled by the addition of various amounts of a “diluent” thiolate. The diluent thiolate also affected control over the propensity of the surface to resist or promote non-specific protein adsorption, depending on whether the MHD (aliphatic and hydrophobic) thiol or the OEG (oligo (ethylene oxide), shown to resist non-specific protein adsorption) thiol is selected. It was expected that the proportional contribution that each axis would to the overall

surface chemistry and functionality would be controlled by the proportion of the thiol associated with that surface property that was present in the completed monolayer. However, it was not expected that the surface properties necessarily would be a linear combination of the proportion of the thiols present in the mixed adlayer; the actual surface properties were determined empirically. As will be shown in this document, all efforts were made to correlate the surface properties to the underlying surface chemistry.

The results presented in this chapter characterize the structure and chemistry of alkylthiolate monolayers that self-assemble when gold surfaces are immersed in solutions containing of a mixture of the component thiols (see Figure 1-1). The general questions that we set out to answer are: 1) is the surface chemistry controllable using these thiols, 2) can the surface chemistry be varied in a predictable manner, 3) are the thiols assembling properly, so that the functional properties of the monolayer are determined by their terminal groups, and 4) do the monolayers also present unexpected or undesirable chemical functional groups at the interface in an uncontrollable fashion?

More specifically, this chapter will characterize the surfaces with respect to these guidelines:

1. Does the elemental composition of the alkylthiolate monolayers agree with the expected composition based on the known chemical formula of the thiols?
2. What is the correlation between the solution thiol ratio used to create mixed monolayers to the ratio of thiols in the resulting monolayer?

3. Do the chains present the terminal chemistry at the surface of the monolayer (that is, with the biotin or OEG terminus actually present on the opposite side of the monolayer from the gold surface?)
4. How well is the interfacial chemistry controlled by the thiolate end-groups; that is, are there unexpected surface chemistries present because the monolayer is not “close-packed”?

### *Specific aims*

The goals for evaluating the structure and properties of the films can be restated in terms of the following quantifiable outcomes:

1. Verify that the interfacial chemistry of gold substrates can be controlled in a reliable, regular, predictable fashion using self assembly of single and mixed alkylthiols
2. Determine the correlation between the solution ratio of the thiols in the assembling solution to the composition of the self-assembled monolayer.
3. Describe the orientation of the thiolates in the film with respect to the surface normal, particularly the location of the biotin endgroup of the BAT thiol.
4. determine the degree of uniformity of orientation among the thiolates in the film.
5. Determine the thickness (the packing density) of the thiolates in the film as a function of monolayer composition and mixed monolayer thiolate ratio

By answering these questions, the experimental data described in this chapter contributes to an overall picture of how the thiols self assembled under various conditions and serve to establish the chemical and architectural basis for understanding the protein binding characteristics of the completed monolayers.

### ***XPS Surface Characterization of Alkylthiolate Monolayers***

This section details the combined results of the XPS experiments undertaken to characterize the chemistry and structure of single- and mixed-composition SAMs.

#### **X-ray photoelectron spectroscopic measurement of surface chemical composition**

A key step in controlling the protein binding activity of our model surfaces is to control the chemistry (i.e., the atomic composition and chemical functional groups) of the interface. As described in detail in the introduction, control over the interfacial chemistry is to be affected by the self-assembly of a defined set of alkylthiolate monolayers on a gold substrate. Once the different thiols were obtained and a relatively reliable means for preparing gold surfaces was available, preparing the surfaces is as simple as putting a gold surface in the thiol solution overnight. This method of surface modification thus offers the advantages of being quite simple and straight-forward, provided, of course, that it does indeed robustly and predictably control surface chemistry. Validation of this method for controlling surface chemistry is the focus of the results presented in this section.

To verify that the interfacial composition is controlled by assembling a monolayer of these particular thiolates, the elemental composition of the gold surfaces used to create the SAMs were compared to their elemental composition measured following SAM formation. Figure 3-2 compares the XPS composition survey scans taken from “bare” gold surfaces and from single-thiolate SAMs created using each of the three different thiols.

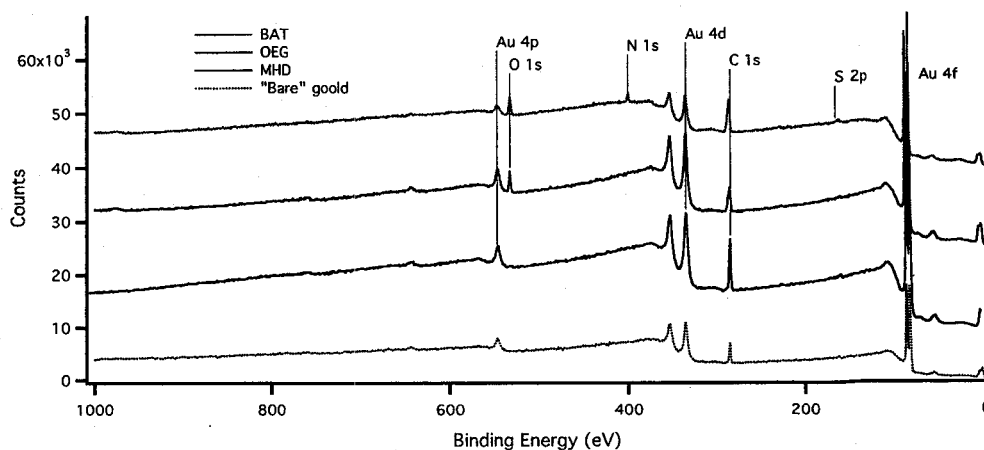


**Figure 3-2: XPS survey scans of single composition SAMs.**

The elemental composition of single composition self-assembled monolayers created from each of the three thiol species were measured by XPS. Peaks are identified as shown (gold doublet peaks are not individually labeled.) The MHD, OEG, and BAT traces have been offset by 9000, 25000, and 40000 counts (respectively) for clarity. The sulfur peak (162 eV) is not readily detectable the figure, although it is measurable in XPS detail scans (not shown.)

The results in Figure 3-2 compare the elements present on the surface of the three different single-composition SAMs to the elements present on a “bare” gold surface.

Whereas on the gold control carbon is the principally detectable element (i.e., greater

than approximately 0.5 atom percent), on the pure MHD surface both carbon and sulfur are present (and no other elements besides gold.) Carbon, oxygen, and sulfur are the only elements detectable in the OEG SAM, and carbon, oxygen, nitrogen, and sulfur are the only elements detectable in the BAT SAM. The sulfur 2p signal is very weak against the background counts and is most detectable in the BAT trace. This result is consistent with the fact that the BAT thiol contains an additional sulfur molecule compared to MHD and OEG (see Figure 1-1).

One notable feature in Figure 3-2 is that the gold substrate contains a significant fraction of carbon. This is a commonly observed result for gold surfaces that have been exposed to the lab environment, mainly the atmosphere, as a result of typical handling methods. It is essentially unavoidable without taking extreme measures for maintaining a contaminant-free atmosphere. Indeed, this method for surface modification would be less useful (and appealing) should such extreme precautionary measures be necessary to make it work. Having said that, though, the data shown in Table 3-1 provides support to the argument that given a modicum of care, the gold surfaces with a small amount of carbon contamination appear to support self-assembly perfectly adequately. The same cannot be said for gold surfaces that have been exposed to ambient conditions for a long period (>1-2 weeks) which do not support self-assembly (see the Materials and Methods section for protocols for removing adventitious contaminants from a “dirty” gold surface.)

This result lays the groundwork for pursuing this method of surface modification by validating a relatively unexciting yet centrally important fact: the only peaks detected in

the completed SAMs (i.e., the only elements present on the surface) are those contained in the thiols used to prepare them. In addition, the proportions of the elements on the surface are the same as those in the thiols; see Table 3-1.

**Table 3-1: Elemental composition of thiols (bulk and as assembled)**

Atomic percentages for pure thiols are determined from molecular formulas (see Figure 1-1) and empirically determined by XPS measurements of SAMs made from the indicated thiol.

	% C		% N		% O		% S	
	Bulk	SAM	Bulk	SAM	Bulk	SAM	Bulk	SAM
Gold	0.0	67.64†	0.0	0.0	0.0	0.0	0.0	2.01†
MHD <sup>a</sup>	94.12	96.4	0.0	0.0	0.0	0.00	5.88	3.6
OEG <sup>a</sup>	76.0	74.5 ± 2.0	0	0.0	20.0	23.6 ± 2.3	4.0	2.0 ± 0.5
BAT <sup>a</sup>	74.47	73.4 ± 2.1	8.51	9.3 ± 0.7	12.77	14.3 ± 1.6	4.26	3.0 ± 0.6

<sup>a</sup> Based on pure, bulk compound †adventitiously adsorbed

As shown in Table 3-1, the expected composition of the surface matches the known proportion of elements in the thiols very closely. The minor differences between the observed and the expected percentages listed in Table 3-1, principally the amount of sulfur present, is attributable to the attenuation of photoelectrons originating from below the surface of the film (Bain and Whitesides 1989). This attenuation leads to a decreased apparent percentage of the elements lower in the film and a concomitant increase in the percentages of elements near the upper surface of the adlayer. Of course this explanation presupposes that the thiolates have assembled properly (i.e., with the sulfhydryl group chemisorbed to the gold surface). This assumption will be validated in the results presented later in this chapter.



To reiterate, this data confirms and validates that self-assembly of these alkylthiols controls the surface elemental composition as expected.

### **High resolution XPS spectral analysis of pure SAMs**

In addition to the general elemental composition of the film, XPS can be used to verify that the chemical bonds made between the elements in the surface layer are consistent with what is known about the chemical structure of the material. The core electrons associated with atoms covalently bonded to heterogeneous atoms (e.g., carbon bonded to oxygen) are bound to their nuclei with slightly different energies than those bound to atoms covalently bonded to homogeneous nuclei. Therefore the emitted photoelectrons from the former atomic species will possess a slightly different kinetic energy than those from a pure, bulk sample. As a result of this, the interatomic chemical bonding patterns are manifested in the fine structure of the photoelectron energy spectra. This is known as the “chemical shift” of the photoelectron binding energy. Reference materials are used to assign chemical identities to peaks contributing to more complex XPS spectra; these known energies are used to identify chemical bonding patterns in experimental samples. To further demonstrate and validate that alkylthiol self-assembly achieves control over surface composition and chemistry, and to verify that the thiolates are bound to the surface as expected, the fine structure of the XPS spectra obtained of the pure SAMs for carbon and sulfur will be examined in detail.

The high-resolution carbon spectrum from an MHD SAM is shown in Figure 3-3. Also shown in this figure is a single Gaussian peak fit. Note close fit between the carbon

spectrum and the single Gaussian peak. This strongly suggests that there is only one carbon species (equivalent to aliphatic hydrocarbons) present in the sample that can be distinguished by XPS. (As the chemical shift is dependent on the type of heterogeneous atom that his bonded to the nucleus in question, some shifts, such as C-S are not readily distinguishable using the available instrumental apparatus.) The presence of a single carbon peak is obviously consistent with both the composition survey (see Table 3-1) for the MHD film as well as the chemical structure of MHD (see Figure 1-1.)

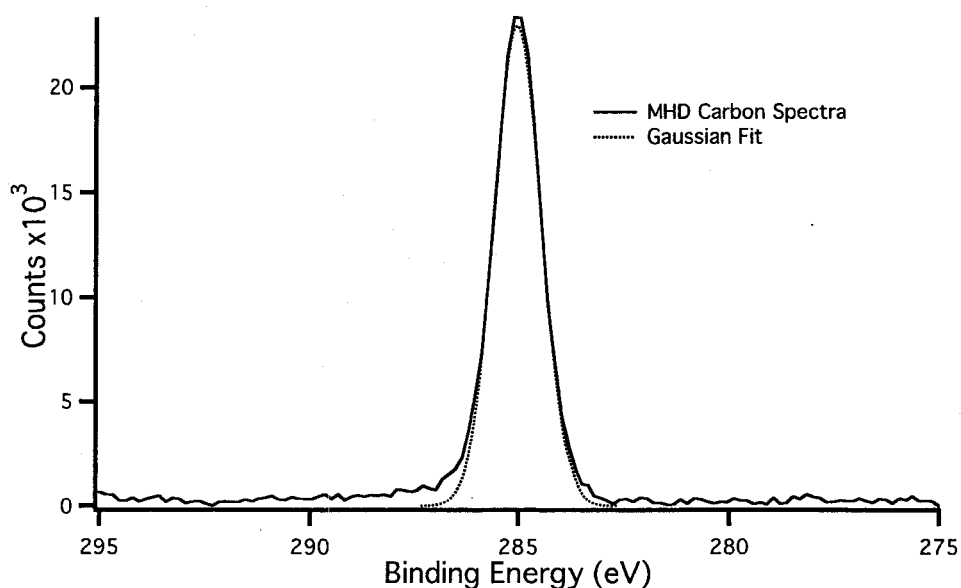


**Figure 3-3: XPS high resolution carbon spectrum from a pure MHD SAM.**

This spectrum is collected with an instrument resolution of 0.16 eV/point, centered around a binding energy of 285 eV. Bulk carbon is generally measured at 285 eV, whereas carbon atoms bonded to other elements (such as oxygen or nitrogen) are detected at slightly higher binding energies. The absence of these higher-energy photoelectrons indicates that only aliphatic hydrocarbons are present in detectable levels

in this sample. The peak fit energy is centered at 285.01 eV, with a FWHM of 1.32 eV. This is highly consistent with graphite carbon spectra.

Likewise, the carbon spectra from the OEG SAM is shown in Figure 3-4. In contrast to the MHD carbon spectrum, the OEG SAM shows two distinct peaks centered at 284.4 and 286.2 eV. These are assigned to aliphatic and ether carbons (respectively). The ratio of the area of the hydrocarbon peak to the ether carbon peak is 0.86, very close to the expected value of 0.9 based both on the chemical structure of the OEG thiol (there are 9 ether carbons oxygens for every 10 aliphatic carbons.) This chemical bonding pattern of the carbon atoms requires (assuming the chemical structure shown in Figure 1-1) a composition of 5 oxygens for every 19 carbons--26.32%-- which is precisely what is seen in the composition survey that gives the surface oxygen percentage as 14.7% and the surface carbon percentage as 53.05% ( $14.7/53.05 = 0.26$ ).

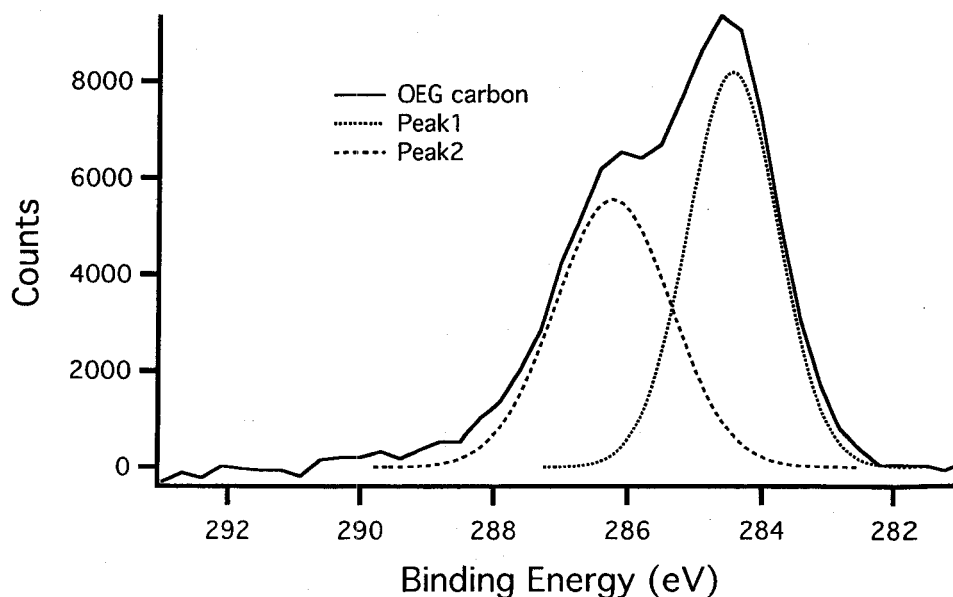


**Figure 3-4: XPS high resolution carbon spectrum obtained from OEG SAMs.**

This carbon spectrum was fit using two Gaussian peaks. The fit algorithm was unconstrained and resulted in peak maxima of 284.43 (C-C) and 286.2 (C-O), with FWHM of 0.96 and 1.22 eV, respectively. Their calculated areas are 13978 (C-C) and 12031 (C-O). This gives a ratio of 0.86 ether carbons for each aliphatic carbon, slightly lower than the expected value of 0.9. Peak fitting was performed using Igor 4.07 (with baseline correction).

As with the MHD, this result confirms that the surface elemental composition and carbon bonding pattern can be controlled by self-assembly of OEG thiolates on gold.

Moving now to the last thiol, the high-resolution carbon spectrum taken from a pure BAT SAM is shown in Figure 3-5. In comparison to the previous two thiols, this high-resolution carbon spectrum is a complex convolution of a number of different functional groups. They have been identified by peak fitting, constraining the peak widths to approximately 1.2 eV to be physically reasonable (lack of baseline separation between the different chemical species makes the fitting algorithm somewhat unstable, occasionally resulting in the creation of fitting peaks 3 eV wide, particularly in the higher binding energy region (> ~288 eV.)

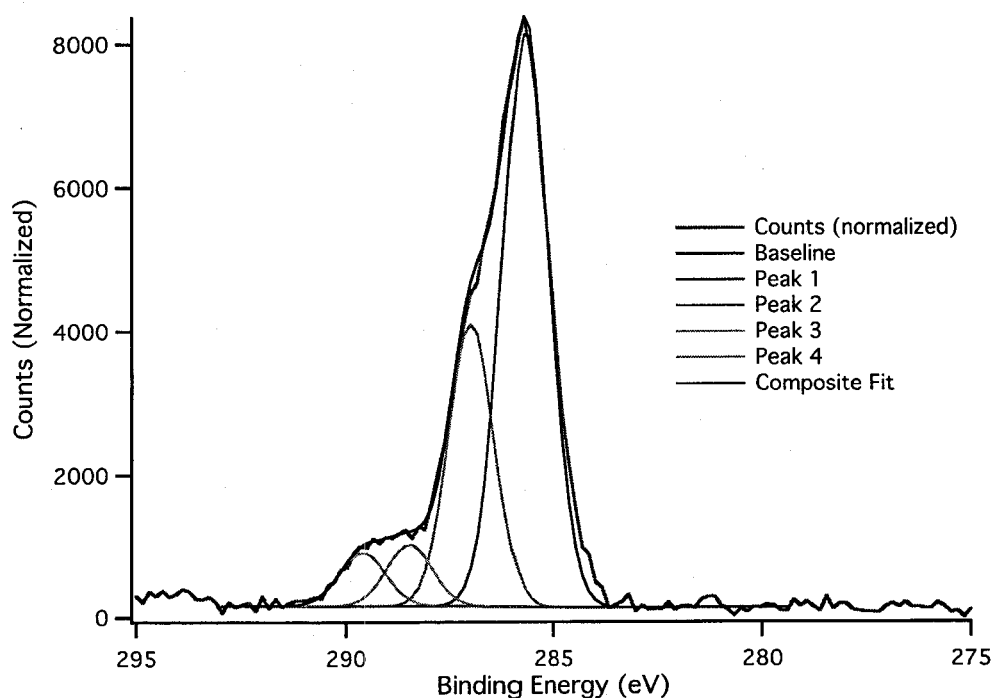


**Figure 3-5: XPS high resolution carbon spectrum from pure BAT SAM**

This spectrum is good example of the fine structure present in SAMs assembled from a solution containing the BAT thiol. The normalized spectrum can be fit with four peaks corresponding to the four carbon functional groups (based on the structure of the BAT thiol) distinguishable using XPS. See Table 3-2 for peak assignments and fitting parameters. Peak fitting in this case was performed by Phi data analysis software bundled with the XPS measuring equipment.

As in the two previous examples, this experimental data confirms the presence of the principle hydrocarbon peak and the expected chemical shifts assigned to ether carbons, amide carbons, and ureido carbons. Table 3-2 contains the peak fit values and compares them to the data expected from the structure of the BAT thiol. As shown, the peak fits correspond well to the expected ratio of functional groups based on the chemistry of BAT.

**Table 3-2: BAT SAM XPS carbon spectrum curve fit values.**

Chemical shift assignments for the peaks used to fit the normalized spectrum are given in terms of the types of carbon functional groups expected (based on the known chemical structure of BAT), the binding energy at fit peak maximum, full-width-at-half maximum, the percentage contribution of the peak to the composite fit, and offers a comparison to the expected percentage of that functional group based on the thiol's elemental composition.

Carbon bonding	Binding energy	FWHM (eV)	Percentage of composite fit	Expected percentage
C-H, C-S	285.73	1.34	60.2	62.9
C-N, C-O	287.05	1.27	28.0	28.6
CNHO	288.53	1.29	6.3	5.7
CN <sub>2</sub> O	289.67	1.32	5.5	2.9

As for the OEG and MHD SAM spectra, this data confirm the expected proportions of chemical shifts due to the different functional groups of the BAT thiol. In conjunction with close agreement of the measured surface composition to its expected value, this validates that these thiols can be used to prepare a molecular film on a gold surface with a defined chemical composition. It is worth acknowledging that, in the more complex case of the BAT carbon spectrum (relative to the OEG and MHD thiols), which contains more than two apparent chemical species, there is no way of determining solely on the basis of this data the exact identity of the chemical bonds. For example, the data does not indicate which other atoms the ureido carbons are bonded with. However, since the proportion of functional groups closely matches those taken from the chemical structure of the thiol, and since it is hard to imagine how the thiol's covalent bonds could be rearranged under these mild assembly conditions, the presumption that the structure of the BAT thiol is the same as it was when determined by proton NMR is quite reasonable.

### High resolution sulfur XPS data

Another important confirmation of the proper assembly of these SAMs is that the thiols are indeed chemisorbed (chemically coordinated) to the gold surface, rather than simply physisorbed (physically proximal; in other words, “just lying there”). Previous studies have shown that the sulfur spectrum of alkylthiol SAMs shifts as a result of chemical coordination of the sulfhydryl endgroup to the gold surface (Castner, Hinds et al. 1996). Basing our analysis on this result, the high-resolution sulfur spectra taken from the three different pure SAMs are shown in Figure 3-6.

The detailed scans of the sulfur binding energy region confirm the presence of one major peak (actually a doublet) present in the assembled MHD and OEG SAMs centered around ~162 eV. This has been assigned to the “bound” (chemisorbed) sulfur species (Castner, Hinds et al. 1996). Somewhat in contrast, the BAT SAM sulfur signal is dominated by a peak at ~164.5 eV that has been assigned to an “unbound” sulfur species. However, a small shoulder is apparent in the spectra around 162 eV, indicating the presence of bound sulfur in this SAM as well. The predominance of the “unbound” sulfur species is attributed to the additional sulfur atom in the biotin moiety of the BAT thiol.

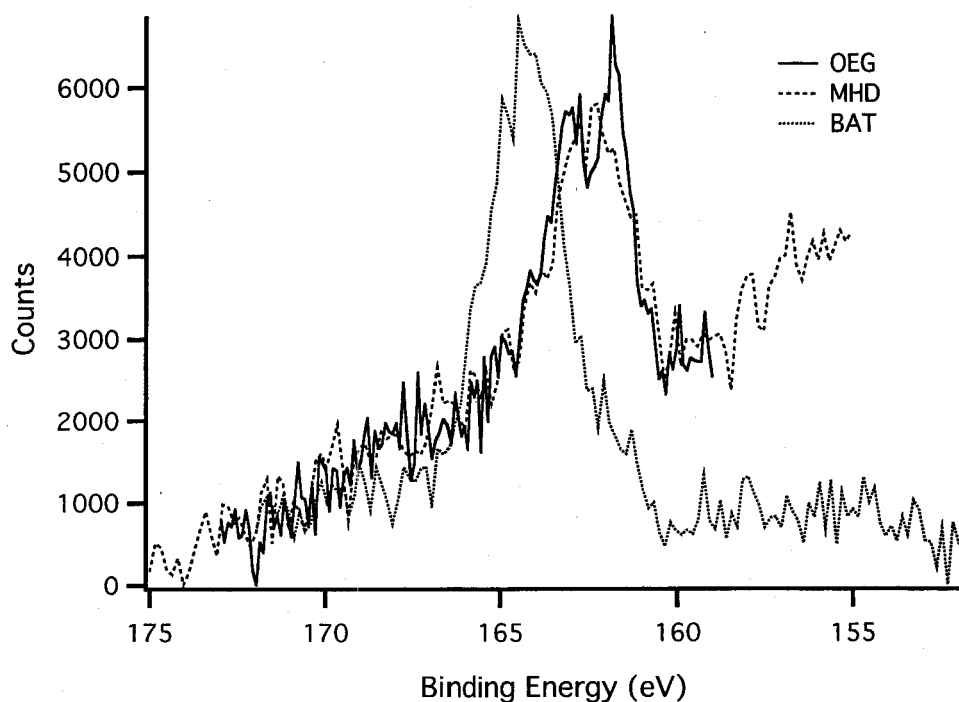


**Figure 3-6: Comparison of XPS sulfur spectra from pure SAMs**

Three high-resolution sulfur spectra collected from three separate samples are overlaid for comparison. Not shown are the carbon spectra collected from the same samples that verify no surface charging has taken place (validating the binding energy comparison between the three samples.) The data shown have not been normalized by intensity. It is unclear why the OEG and MHD baselines appear to slope downward as the binding energy increases (though this was a commonly observed result.)

This evidence complements the raw elemental composition of the surfaces by showing that the thiolates are bonded to the surface as expected, further verifying this method for controlling the chemistry of the surfaces, as well as its potential for using as a robust tissue culture substrate, as the binding energy of thiolates on gold has been estimated to be on the order of  $\sim 28$  kJ/Mol (Sellers, Ulman et al. 1993)



### **Determining whether the biotin sulfur can bind to the gold interface**

Studying the binding of BAT to gold raises an obvious question as to whether the naturally occurring sulfur in biotin could chemisorb to the gold surface in the same way that the sulfhydryl group on the opposite end reliably does (indeed, some studies have reported the self-assembly of dialkylthiols—albeit to low density—which would be closely analogous to the binding of the biotin sulfur (Nuzzo, Fusco et al. 1987; Nuzzo, Zegarski et al. 1987) .) This answer to this question is fundamentally important to the success of this surface modification strategy since if the biotin sulfur does bind to gold then the key biotin functionality can be buried at the gold interface and inaccessible to potential binding partners.

The experimental plan described in this section that was developed to determine whether biotin can bind to gold again depends the chemical shift observed in the sulfur photoemission spectrum when sulfhydryl molecules chemisorb onto gold. As mentioned previously, reports published at the time of these experiments had shown that chemisorbed alkylthiolate sulfur photoemission spectra contained one main peak centered around 162.2 eV, whereas the spectrum of unbound sulfur centered around 167 eV. Detecting this shift would be evidence of sulfur chemisorption, while its absence would suggest that no chemisorption was taking place.

The experimental plan can be summarized as follows: compare the XPS sulfur photoemissions observed from a preparation of reagent quality biotin (with no gold present) to a “bare” gold control, a gold surface that had been dosed with biotin, and a

gold surface that had been similarly treated with biotin and subsequently used to assemble a MHD SAM. The reasoning is that if a comparison of the sulfur spectra from the “plain biotin” (i.e., with no gold present) to the biotin treated gold showed a similar chemical shift as is observed when the gold surface is treated with MHD, this would suggest that the biotin sulfur was interacting with the gold surface in a similar fashion as the thiolate sulfhydryl group. The results of this analysis are shown below, beginning with the sulfur photoemission spectrum for pure biotin (Figure 3-7.)

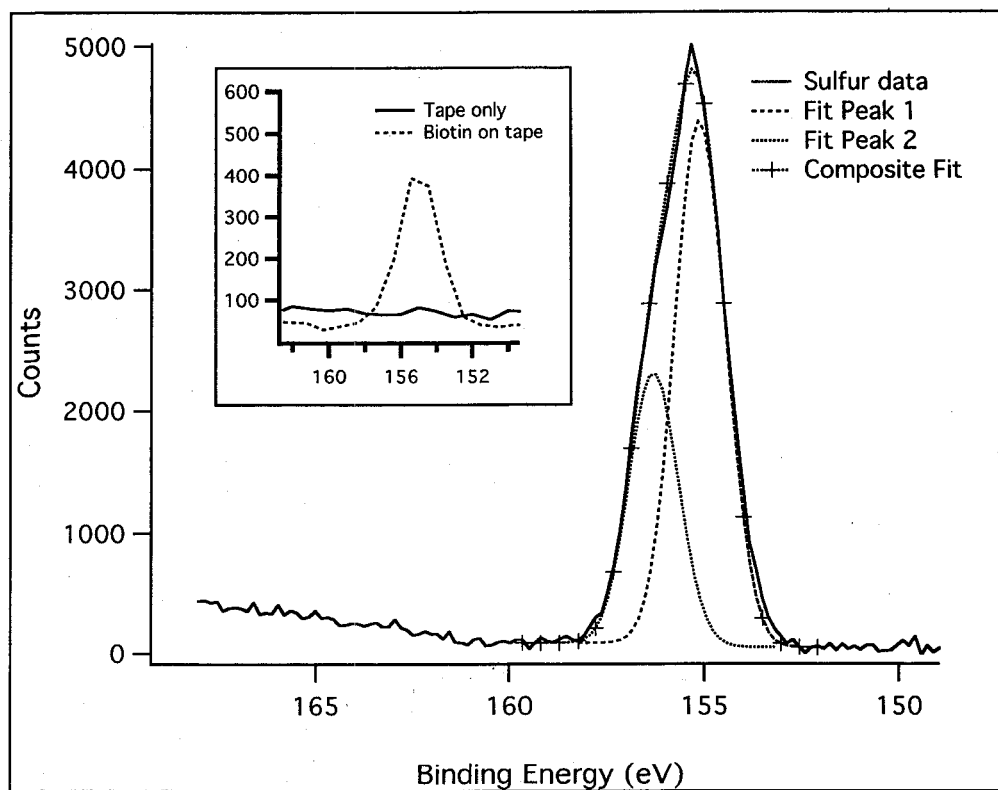


**Figure 3-7: Biotin sulfur photoemission spectrum.**

This spectrum was collected by treating a small piece of double-stick tape attached to the analyzer stage with a thick coating of powdered biotin. The sulfur binding energy region of the tape is shown in the inset as a control. Data were acquired using a 5 eV flood gun potential due to the insulating properties of the mounting mechanism.

As expected for a single sulfur 2p species, the sulfur signal can be fit using two peaks, approximately 1.25 eV apart, in a ratio of 2:1 (Castner, Hinds et al. 1996). Based on this result, native biotin sulfur photoemission energy is 162.65 eV (the data was acquired under a 5 eV flood gun to alleviate surface charging; however, the hydrocarbon reference maximum was detected at 277.1 eV, establishing a 7.4 eV rather than 5 eV offset; the reason for this discrepancy is unknown). In addition, only one sulfur species is detected. As this was the best available comparison for "unbound" sulfur in biotin, it was used as a basis for comparison to similar measurements taken from a gold surface treated with biotin. This data from this measurement is shown in Figure 3-8.

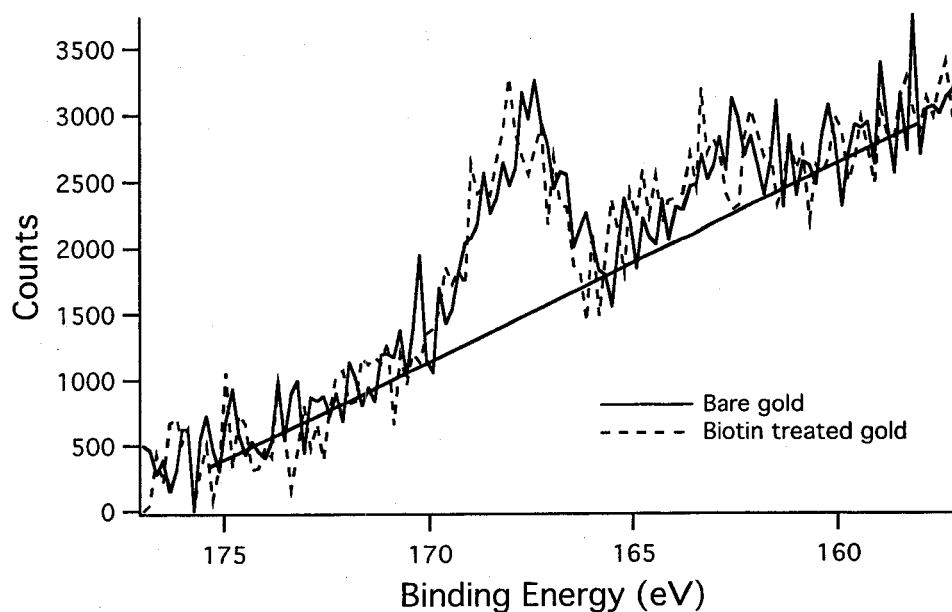


**Figure 3-8: High resolution sulfur spectra from gold and biotin-treated gold surfaces.**

Two spectra are shown, 1) from a “bare” gold surface (albeit exposed to atmospheric contaminants that are almost certainly the source of the sulfur compounds detected in the XPS spectrum), and 2) from a gold surface that had been treated with a 2 mM solution of biotin in ethanol for an hour followed by an ethanol rinse. Both spectra show evidence of bound (162 eV) and unbound (167 eV) sulfur compounds.

The first thing to note from these spectra is that the majority of the sulfur signal represents “unbound” gold, with lesser but still detectable amount of “bound” sulfur. The next most significant finding is that the two spectra are essentially identical, particularly when comparing the absolute and relative sizes of the two sulfur peaks. The simplest explanation for these observations is that the biotin compound has not contributed to the sulfur signal observed in the biotin treated case (in other words, there was no difference between the control and experimental surfaces.) The carbon and nitrogen spectra also

support this interpretation, as shown first in the carbon photoemission spectra (Figure 3-9.)

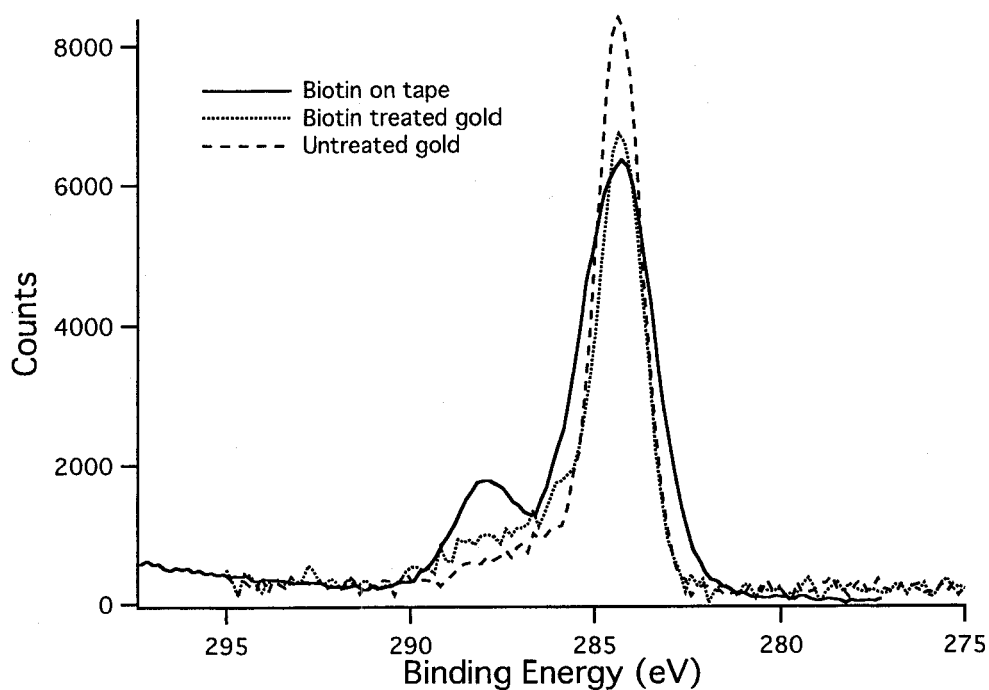


**Figure 3-9: High resolution carbon spectra comparison between gold, biotin-treated gold, and biotin.**

Three carbon binding energy region XPS detail scans are shown (see legend): 1) biotin on double-sided tape, 2) gold surface treated with an ethanolic solution of biotin, and 3) an untreated gold surface. The biotin only spectra was offset by +7.4 eV to facilitate comparison with the carbon spectra from the other surfaces (this shift is likely a result of uncorrected surface charging.)

Note the strong shoulder present at ~288.5 eV in the biotin spectrum which is indicative of ureido groups. This ureido peak is not nearly as prominent on either the gold control or, most importantly, on the biotin treated gold. In particular, note that the ratio of the peak heights between this ureido peak and the main aliphatic peak in

comparison to the ratio of peak heights from the gold and biotin-treated gold spectra. Since the latter two peak height ratios are clearly dissimilar to the biotin spectra, it is extremely unlikely that the higher energy shoulder of these two spectra represent the same ureido chemistry resulting from significant amounts of biotin present on the surface.

Similarly, to the carbon spectra, comparison of the nitrogen spectra show that the signal on the bare gold is much stronger than the biotin treated gold (Figure 3-10). The most likely explanation is that there is more nitrogen present on the "bare" gold than on the biotin-treated gold. This would not be the case if biotin did chemisorb to gold, therefore this nitrogen signal is likely the result of nitrogen-containing adventitious contaminant. Whereas the nitrogen signal on the tape is very strong, direct comparison is difficult as the amount of biotin present on the tape is much greater than the amount of biotin present on either gold surface.

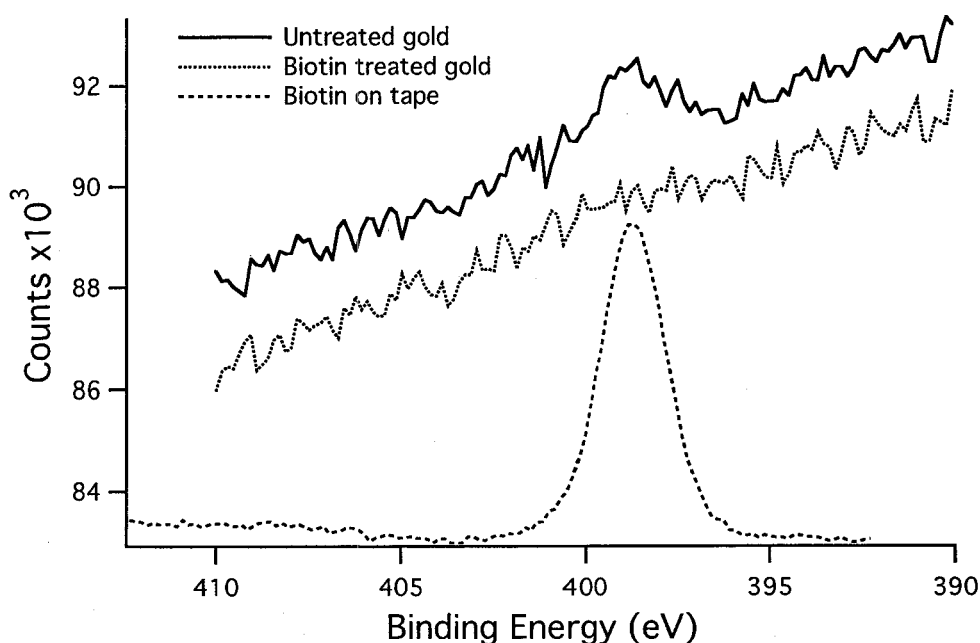


**Figure 3-10: High-resolution nitrogen spectra comparing gold, biotin-treated gold, and biotin.**

Note the conspicuous absence of a nitrogen signal on the biotin-treated gold sample. The absence of this nitrogen signal strongly argues for the absence of chemisorbed biotin remaining following treatment of this surface with biotin. As in the previous example, the plain biotin spectrum has been offset by +7.4 eV for comparison with the other spectra.

We note the difference between the greater amount of nitrogen present on the “bare” gold spectra and the greater amount of carbon present on the biotin-treated surface. This difference may be reasonably attributed to different adventitious organic contaminants on the gold surface, with the “bare” gold surface happening to collect a somewhat higher level of nitrogen than the former, whereas the biotin-treated surface collected a different composition of carbon. This explanation is consistent with the evidence from the carbon spectra. Comparing of the spectra in Figure 3-9, the most obvious difference is the

presence of a much stronger peak at ~288.5 eV peak (probably CNHO) in the biotin spectra, and a broader FWHM of the more prominent hydrocarbon peak. The absence (or very minimal presence) of these signals in the biotin-treated gold sample suggest at the very least that nearly undetectable amounts of biotin bound to the gold substrate, if any did at all.

It is worth noting that in order to compare the spectra obtained from the biotin on double-sided tape to the one obtained from biotin treated gold, the pure biotin spectra needed to be offset by 7.3 eV, 2.3 eV greater than the potential provided by the flood gun (the carbon and nitrogen spectra also support this conclusion.) This correction brings the "unbound" sulfur signal coming from the biotin sulfur directly into alignment with the "bound" sulfur signal obtained from sulfhydryl groups coordinated to the gold interface. Assuming then that the sulfur binding energy caused by the presence of biotin is not affected by close proximity to a gold surface, the "bound" sulfur signal detected in the BAT SAMs could be the presence of sulfur in biotin that is fact not bound to the gold. Indeed, assuming that this chemical shift (i.e., from "unbound" at 167 eV to "bound" at 162 eV) occurs when the sulfur atom is coordinated via some electron sharing mechanism (though not necessarily a covalent bond), since plain biotin already photoemits at the "bound" energy, it may not have an available binding mechanism to further coordinate with gold. It is, however, difficult to reconcile these results with those obtained from the BAT SAMs, which clearly show a strong peak at 167 eV and a smaller one at 162 eV. Moreover, as will be shown in the SPR chapter, it is clear that wild-type



streptavidin bound to BAT SAMs does not dissociate except over very long time periods which indicates the BAT thiols are strongly attached to the surface.

Nevertheless, while this is an argument rather than a direct proof, the preponderance of the evidence from the carbon, nitrogen, and sulfur signatures obtained from the biotin treated gold surface do not differ significantly from those from an untreated gold surface. Therefore, due to the lack of directly comparable signatures between pure biotin and biotin treated gold, the most reasonable conclusion is that biotin does not bind to gold nearly as well as the sulfhydryl group on the thiols do (or that biotin can be readily displaced physically through rinsing.) One result that is left an open question is the presence of two sulfur species, bound and unbound, in the sulfur photoemission spectra from BAT SAMs. This will be revisited in the section detailing the angle-resolved XPS data.

### **OEG Thiolates Are Damaged by X-Ray Exposure**

As a standard method of precaution against experimental artifacts, survey spectra were always collected both before and after composition analysis during initial SAM characterization. Usually, the spectra (and composition analysis based on them) were identical within instrument stability and precision. However, in the case of the OEG SAMs, noticeable degradation of the overlayer was observed. Figure 3-11 highlights the differences in the carbon, gold, and oxygen peak intensity following data acquisition (and requisite X-ray exposure) from a pure OEG SAM.

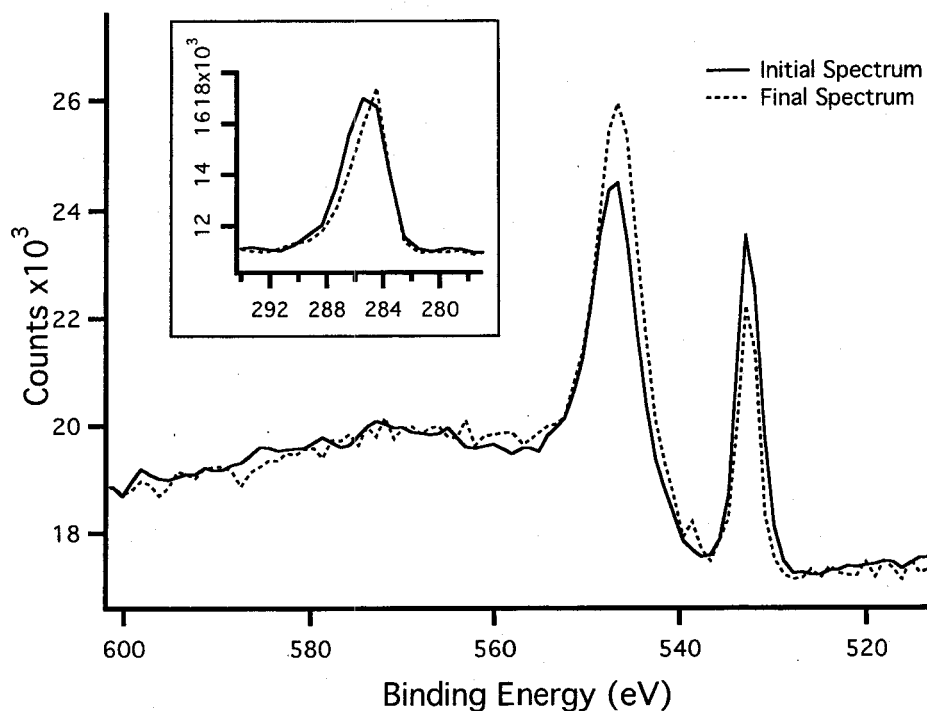


**Figure 3-11: Change in gold and oxygen intensity following extensive X-Ray exposure.**

The binding energy range from the initial and final survey scans (1000 eV range) shown is restricted to highlight the change to the oxygen and gold peak intensity. The inset shows the carbon binding energy range; the legend applies similarly to both the main data and the inset. The final spectrum was taken after 202 scans 20 eV wide (128 points  $\sim 0.16$  eV/point).

Figure 3-11 clearly illustrates how the gold 4d 7/2 peak has increased and the nearby oxygen peak decreased in intensity following data acquisition. This change in the spectral data suggests that the OEG films are susceptible to X-ray damage resulting in a loss of oxygen and subsequent decrease in film density. Additional evidence is shown in the inset in Figure 3-11 which compares the carbon binding energy range of the initial and final survey scans peak area measurements (not shown) indicate that the carbon peak

has lost ~0.75% of its area, similar to the decrease in the area of the oxygen peak (99.5% of initial). Consistent with the supposition that the OEG thiolates are deteriorating, the gold signal increases following prolonged X-ray exposure as a result of decreased inelastic scattering of the gold photoelectrons (attenuation) through the sparser adlayer. This observation led to estimations of the degradation rate so as to establish safe data acquisition parameters (described in more detail below.)

Figure 3-12 more clearly illustrates the difference in the relative peak heights of the hydrocarbon vs. ether carbon peaks after prolonged X-Ray exposure. The data suggest that the surface is losing oxygen atoms.

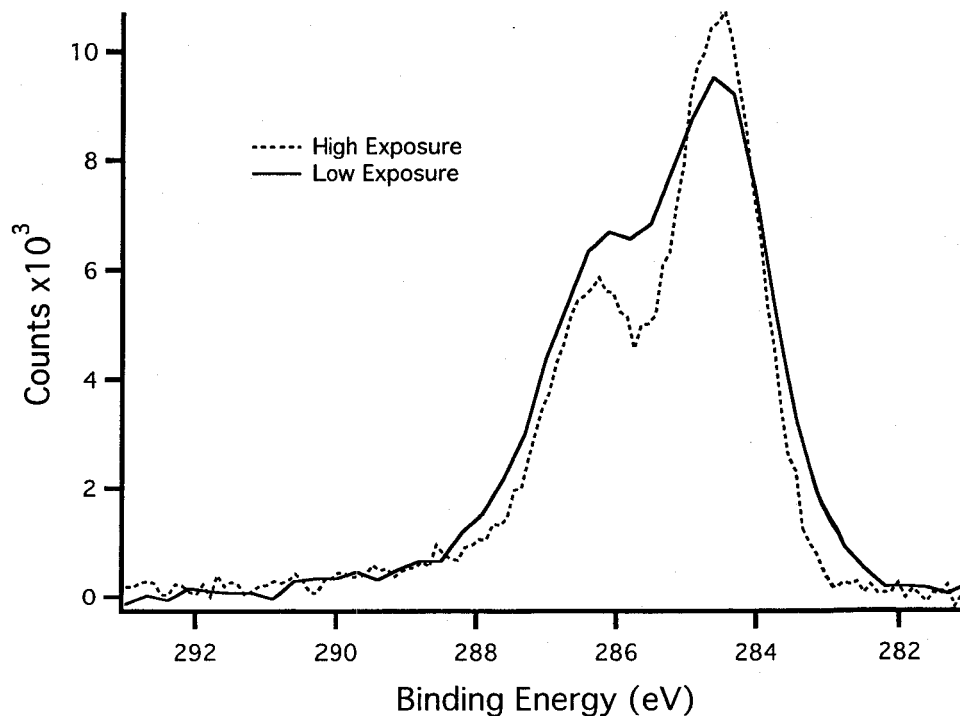


**Figure 3-12: Difference in high resolution carbon spectrum taken from OEG SAMs experiencing different X-Ray exposure times.**

Traces are taken from two different samples. The first, "High exposure" trace was collected before the lability of OEG was in question, the second, "Low exposure" trace was collected following minimal X-ray exposure. Note the significantly different C-C and C-O peak ratios resulting from higher X-Ray dosage.

The two spectra in Figure 3-12 were fit using similar Gaussian peak fit parameters to get a quantitative idea of the amount of degradation the surface undergoes for a given amount of X-Ray exposure (peak fits are not shown for clarity). The results of the peak fits are given in Table 3-3.

**Table 3-3: Peak fit parameters for OEG XPS high-resolution carbon spectra.**

The compound spectra were fit using two peaks assigned to the C-C and C-O binding energies. Peak fit results are tabulated; the ratio of the peak areas indicates the ratio of ether to aliphatic carbons in the film (expected value = 0.9). Increased X-ray exposure results in the loss of the ether carbons. The "low exposure" results were taken after a total of 2 survey scans (1.0 eV/point, 1000 eV energy range) and 4 detail scans (0.16 eV/point, 12 eV range), whereas the "high exposure" results were taken after 2 survey scans and 100 detail scans.

X-ray dose	Peak	Maximum (eV)	Width (eV)	Amplitude (counts)	Area (counts <sup>2</sup> )	Peak area ratio
Low	1	284.5	0.96	8195	13982	0.861
	2	286.2	1.22	5549	12038	
High	1	284.5	0.802	10200	14492	0.681
	2	286.3	1.06	5252	9866	

The amount of degradation of the OEG SAM has been estimated by plotting the change in the O/C ratio as a function of the number of "points" scanned between the end

of the initial and the beginning of the final measurement. The results are shown in Figure 3-13.

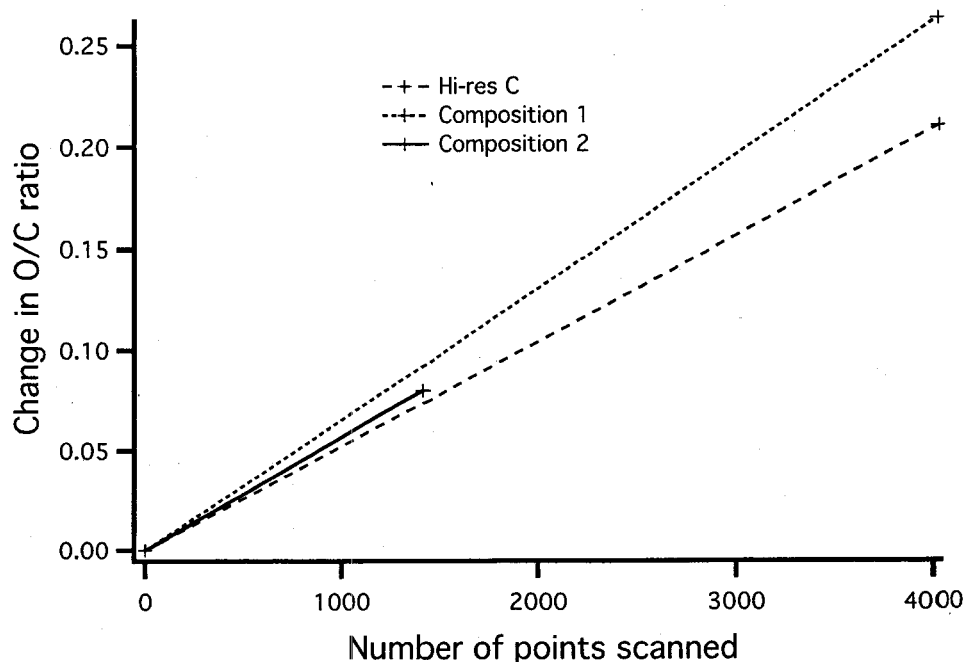


**Figure 3-13: rate of change in O/C ratio of OEG SAMs resulting from X-Ray exposure.**

This plot compares the difference in the oxygen/carbon ratio as determined before and after substantial X-ray exposure. Three pairs (initial and final) of data are shown: two composition survey measurements taken from different spots on the same surface and the high resolution carbon peak fit ratios taken from a different surface. The initial data are normalized to zero change: it assumes that the “true” initial ratio has not been affected by the scans occurring during initial data acquisition. The slope (rate of damage) is equal to 0.0567 per 1000 points scanned

The close agreement in the different slopes suggests that the rate of degradation is fairly uniform for the OEG SAMs. This plot is useful for adjusting composition data to its “true” initial value under circumstances that require prolonged X-ray exposure to a surface for sensitive measurements.

### **XPS data analysis of binary composition “mixed” SAMs**

As detailed in the introduction to this chapter, the surface properties of properly assembled SAMs are determined by the thiolate end groups. By extension, the properties of mixed SAMs (i.e., assembled from a mixture of two thiols) might be expected to be essentially the weighted average of the single composition SAM's surface characteristics based on the proportions of each of the different thiolate chemistries present in the mixed monolayer. This section will focus on characterizing the how the chemical composition of the adlayers were affected by the assembling solution conditions, i.e. the proportion of the two thiols used to create the mixed monolayer.

### **Correlation Between Solution and Surface Thiol Composition As Measured By XPS Quantification of SAM Nitrogen**

Quantitation of the surface proportion of the different thiolates in a mixed SAM is achieved using XPS measurement of the amount of nitrogen in the adlayer. This method is enabled by the observations, tabulated in Table 3-1, that neither the OEG or MHD SAMs contain any detectable nitrogen, whereas the addition of BAT molecule, which is 8.5% nitrogen, to the assembly solution establishes the presence nitrogen in the composition of the film. Importantly, as the proportion of BAT to the diluent thiol in the assembling solution increases, the amount of nitrogen measured in the film increases to equal the proportion in the molecule (within instrument precision and photoattenuation-related artifacts, see Table 3-1). Since BAT is the source of nitrogen in films that contain it, measuring the amount of nitrogen in the film determines the quantity of BAT present.

To calculate the fractional coverage of BAT in mixed BCMs we assumed that the total number of molecules in a fully assembled SAM is roughly constant so the fraction of nitrogen in the film compared to the maximum amount present in pure BAT films determines the fraction of BAT in a mixed BCM. Figure 3-14 shows an important and useful result: the correlation between the solution mole fraction of BAT and the amount of surface nitrogen (thus the surface mole fraction of BAT) in mixed BAT / OEG and BAT / MHD SAMs.

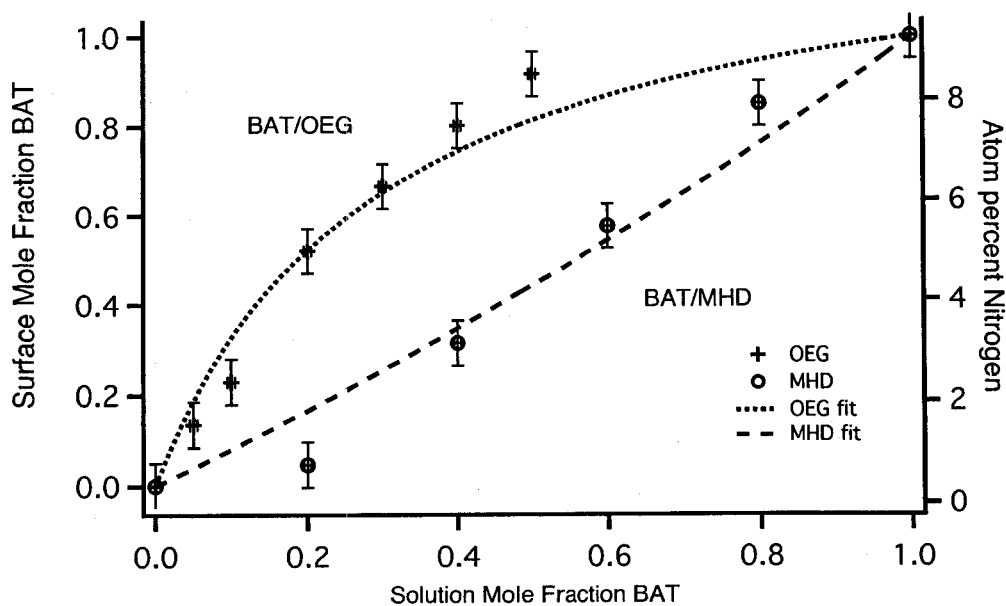


**Figure 3-14: Correlation between solution and surface thiol ratio for mixed BAT SAMs**

The amount of nitrogen in the mixed SAMs generated with a given solution thiol ratio as measured in vacuum by XPS is used to determine the proportion of BAT in the completed alkylthiolate monolayers. The data have been fit to a function derived from assumptions about the rate of adsorption of the two thiols in the solution (see text for further details.) Y-error bars are  $\pm 5\%$  due to precision of XPS measurements, X-error

bars are smaller than marker, precision along this axis is mainly limited by accuracy of volumetric measuring equipment.

This result enables both the prediction of the surface composition based on the assembly solution thiol ratio (obviating the necessity for further expensive XPS measurements) and the ability to compare surface properties between mixed SAMs containing either the BAT or MHD diluent on the basis of the proportion of the BAT / diluent ratio on the surface itself.

A mathematical relationship was derived between the proportion of thiols in a mixed solution and proportion of thiols in the film it produces. To do so, the solution mole fraction of BAT,  $\chi_{BAT,sol}$ , was defined for the mixture of thiols used for SAM assembly, and similarly  $\chi_{BAT,sur}$  was defined as the surface mole fraction of BAT in a mixed SAM. Assuming that the adsorption of the two thiols, BAT and a diluent thiol, are both irreversible and follow first-order Langmuir kinetics, then at saturation the ratio of their surface coverages should be proportional to the ratios of their adsorption rate constants,  $R = k_{BAT}/k_{diluent}$ , times the ratio of their concentrations in the bulk solution:

$$\frac{\chi_{BAT,sur}}{\chi_{diluent,sur}} = R \left( \frac{\chi_{BAT,sol}}{\chi_{diluent,sol}} \right) \quad (1)$$

Since  $\chi_{BAT} + \chi_{diluent} = 1$  in both phases, this simplifies to:

$$\chi_{BAT,sur} = \frac{R\chi_{BAT,sol}}{1 + (R - 1)\chi_{BAT,sol}} \quad (2)$$

The surface composition estimated from the XPS nitrogen data collected from the BAT/OEG SAMs were well fit to this function (Figure 3-14, dotted curve). This fit



yields  $R = 4.22$ . The fit to the nitrogen data for mixed BAT/MHD SAMs is also shown in Figure 3-14 (dashed curve) yielding  $R = 0.80$ .

The differences in the shapes of the two curves (BAT / MHD and BAT / OEG) can be understood by considering the relative solubilities of the different thiols in ethanol. Whereas the MHD thiol is strictly aliphatic and therefore of moderate solubility in ethanol, the higher molecular weight of the BAT thiol is balanced by the inclusion of functional groups with higher solubility in polar solvents. In contrast, the OEG thiol is both shorter and has a higher relative percentage of polar or hydrophilic (capable of hydrogen bonding) groups, and is thus relatively well-solvated in ethanol, particularly compared to the BAT thiol. These functions were used in subsequent experiments to estimate the surface thiolate ratio generated from a particular solution thiol ratio without further XPS analysis.

#### **High resolution carbon spectra reflect increasing proportion of BAT in mixed SAMs**

The increase in the amount of BAT in mixed SAMs created from assembling solutions containing increasing proportions of BAT, measured by the nitrogen content of the film in the previous section, was verified by means of high-resolution carbon XPS spectra. These comparisons showed that not only did the proportion of nitrogen in the films increase, but that the nitrogen was associated with the carbon chemistry expected based on the high-resolution carbon XPS spectrum taken from a pure BAT SAM (Figure 3-5.) As shown in Figure 3-15, the peaks associated with amino and uriedo carbons increased smoothly with increasing amounts of BAT in mixed BAT / MHD SAMs.

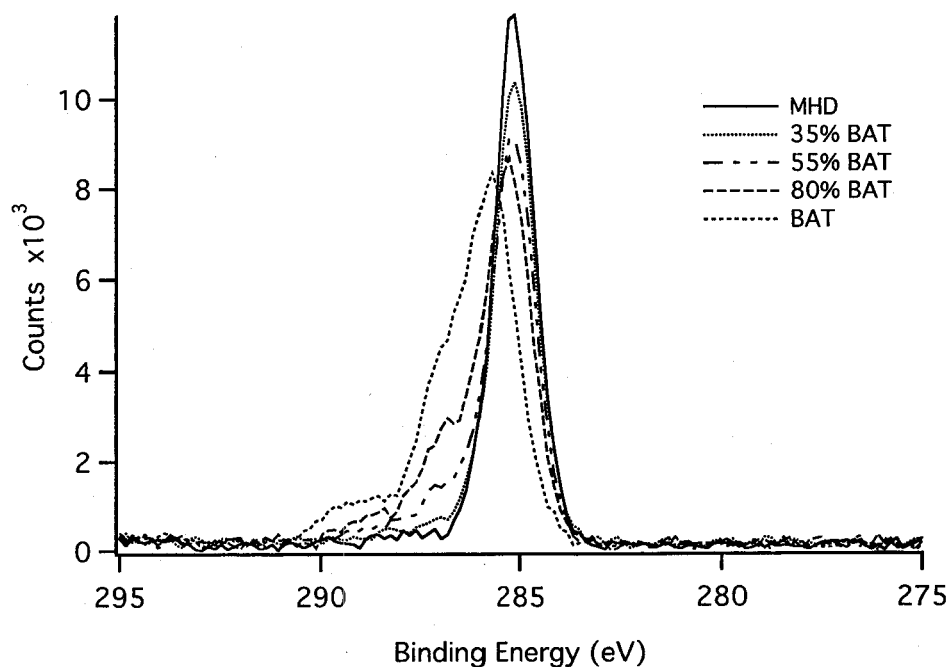


**Figure 3-15: High resolution XPS carbon spectra from BAT / MHD SAMs**

The peak shoulder intensity between  $\sim 287$  and  $\sim 291$  eV increase with the amount of BAT in the SAM. The leftward shift of the main  $\text{CH}_x$  peak of the pure BAT spectra is likely due to slight charging of the surface during data acquisition.

The shape of the XPS spectra indicates that the carbon chemistry of the films is changing predictably as a result of the increasing surface mole fraction of BAT in the film, further confirming the increasing amount of BAT in these mixed SAMs.

(The shift in the pure BAT SAM spectra toward slightly higher binding energy is most likely due to surface charging as electrons are ejected from the surface and may have resulted from poor electrical conductivity between the surface and the sample holder; this result is not representative of most experiments. A similar plot is not shown for mixed BAT / OEG SAMs since, as previously discussed, the OEG thiolates are

photolabile, which will introduce artifacts to the data that vary with the percentage of OEG in the mixed SAM, making drawing conclusions difficult.)

**Summary of key observations and conclusions mixed BAT/MHD and BAT/OEG SAMs:**

1. Self-assembly of these thiols on a gold surface will define the interfacial chemical composition.
2. The XPS nitrogen signal from SAMs generated from solutions of both thiolate mixtures varied from 0% to 9.5 % as the proportion of BAT in the assembling solution was varied from 0 to 1. This dependence on the presence of BAT in the solution for a nitrogen signal in the film means that the proportion of thiolates in mixed SAMs can be inferred by quantitating the percentage of nitrogen present in the film using XPS.
3. The empirical correlation between the surface percentage of BAT and the solution percentage BAT differed when using the OEG diluent compared to the MHD diluent.
4. Knowing the correlation between the solution thiol ratio and the resulting surface composition enables the proportion of thiolates in mixed SAMs to be controlled simply by choosing a specific ratio of thiols for the assembling solution.
5. A mathematical model derived from basic assumptions about how the thiols deposit on the surface from solution has been derived can be used to estimate the correlation between the solution and surface thiol ratios. This correlation has

proved very useful for comparing the protein binding behavior of mixed SAMs without needing to measure their surface composition in the XPS chamber.

6. Biotin does not coordinate to gold through its sulfur moiety to any appreciable extent.
7. OEG thiolates are susceptible to X-ray damage. This should be taken into account when using XPS to quantitate surface compositions of films containing the OEG thiolate.

This analysis completes this chapter's specific aims 1 and 2 by conclusively demonstrating that the surface chemistry can be reliably and predictably controlled using this surface modification technique.

### ***Angle-resolved XPS thiolate orientation analysis***

Once the surface composition of the SAMs had been verified and the composition of mixed SAMs could be estimated from the solution thiol ratio, focus was switched to confirming that the interfacial properties of the substrate were determined by the thiolate end groups. This is extremely important since if the endgroups are not in fact present at the new interface formed by self-assembly, then they will not define the chemistry and characteristics of the surface, debilitating control over the properties of the interface.

Work to confirm that the thiolate endgroups were present at the interface began by measuring the elemental composition of the SAMs as a function of photoelectron take-off angle. These angle-resolved XPS measurements gave supporting evidence that,

at least in the high-vacuum environment of the XPS chamber, the end groups of the thiols were usually present at the surface of the adlayer.

### Alternative models for bond packing uniformity and chain extension for pure BAT SAMs

The analysis carried out in this section were undertaken to distinguish between two potential and fundamentally different film “architectures” illustrated in Figure 3-16.

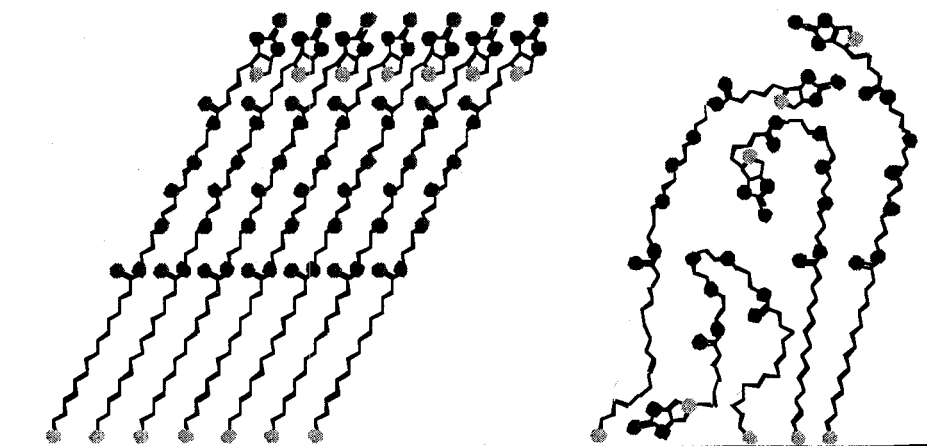


**Figure 3-16: Potential orientations of biotin-terminated thiolates to illustrate potential outcomes of ARXPS experiments.**

Two potential outcomes of BAT self assembly are shown: 1) regular, close-packed, all trans methylene bonds in an extended chain canted approximately  $30^\circ$  from the surface normal (as observed for pure MHD SAMs) and 2) irregular, loosely packed thiolates with the biotin end groups randomly oriented relative to the gold interface. The density of thiolate packing in the second case would probably be higher than depicted, as would be the amount of chain conformational irregularity. Color code is as follows: yellow = sulfur, red = oxygen, blue = nitrogen, black = carbon

This figure illustrates how the distribution of elements in the films would vary depending on the average orientation of the thiolates in the adlayer. In the first (left),

regular, uniform close packing of the BAT thiolate chains would result in similarly regular distribution of the elements in the film, with nitrogen and oxygen concentrated near the interface. In the second (right), non-uniform, random packing of the BAT chains would lead to a more uniform distribution of elements throughout the depth of the film.

To differentiate between the two opposing models shown in Figure 3-16, angle-resolved XPS experiments were undertaken to characterize how the elements were distributed within the pure and mixed BCM adlayers. Particularly for the BAT thiolate, a higher concentration of oxygen and nitrogen near the surface would suggest the former, more regularly oriented thiolate architecture, whereas a more uniform (or inverted!) distribution of elements would suggest the more disordered, irregularly oriented thiolate architecture. It is important to note that the heteroatoms (i.e., non-carbon) atoms are relatively widely distributed in the BAT thiolate, somewhat limiting the resolution of this type of depth-profile analysis. Nevertheless, in conjunction with other types of experimental data (to be discussed in detail later in this section), the ARXPS results provide a useful data set for determining how the thiolates are organized and oriented in the different pure and mixed SAMs.

#### **Angular dependence on nitrogen to carbon ratio as a function of surface mole fraction BAT**

XPS measurements of the proportions of elements in a surface will change as a function of the photoelectron take-off angle if the distribution of elements in the surface varies as a function of depth from the surface. This is a result of the increase in path

length of photoelectrons emitted as a function of the depth of emitting atom according to the relationship

$$I = I_0 e^{-\frac{d}{\lambda \cos \theta}} \quad (3)$$

where  $d$  is the depth below the surface,  $\lambda$  is the mean free path of the photoelectrons (which has the same units as  $d$ , Å in this case), and  $\theta$  is the angle in degrees between the surface normal and the detector aperture.

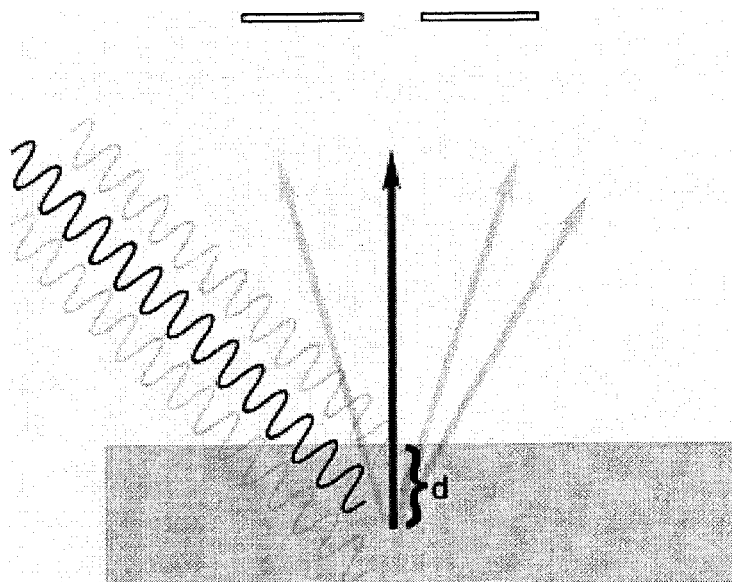


**Figure 3-17: Basis for ARXPS composition depth profile measurements**

Incident X-rays (from left) cause photoemission from elements (usually) below the surface. Since only unscattered (or elastically scattered) photoelectrons retain useful information, photoelectrons emanating from elements deeper within the film (increasing  $d$ ) are attenuated more than those from the surface. Rotating the sample so that the surface normal vector (black arrow) was directed away from the aperture (top of diagram), photoelectrons attenuation from below the surface is increased according to the relationship given in equation 3. Therefore, high-incidence photoemission is extremely surface sensitive.

XPS composition data (carbon, nitrogen, oxygen, sulfur, and gold) were collected from mixtures of BAT/MHD and BAT/OEG SAMs at three (0, 5, 80) or five (0, 39, 55, 68, 80) take-off angles (TOAs). Since the overall composition of these mixtures will change as the proportion of the various thiolates changes, in order to make comparisons between the elemental composition vs. take-off angle among different SAM mixtures, the *ratio* of nitrogen to carbon was used, with the ratios obtained at the various TOA were normalized to the ratio from that composition SAM obtained at normal incidence ( $\theta = 0$ ) (which was set to 1.) The results of this analysis are shown in Figure 3-18.

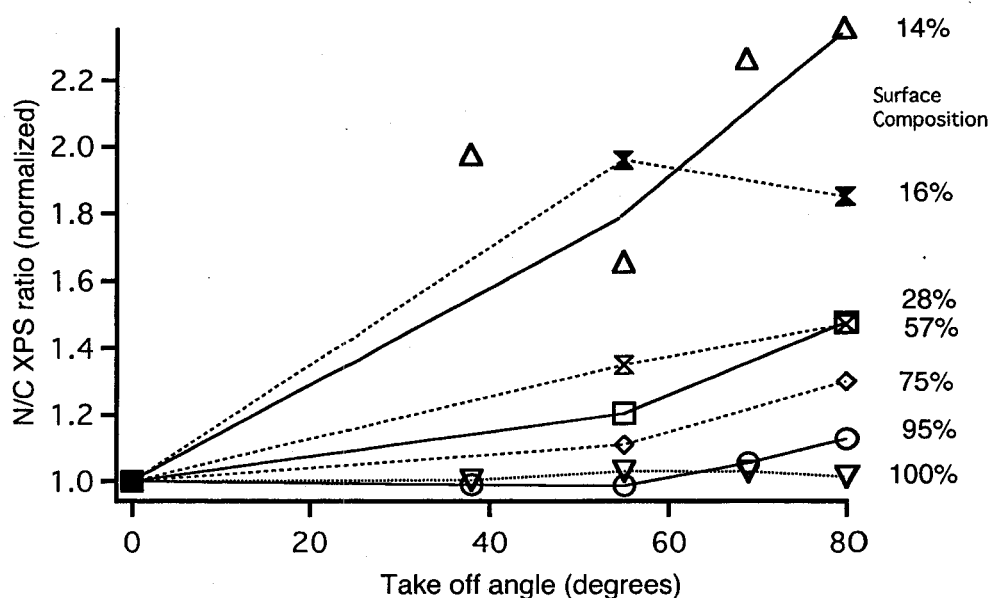


**Figure 3-18: ARXPS N/C ratios for different surface compositions of mixed BAT SAMs**

The orientation of the biotin containing thiolates is a function of the fraction of BAT in the film. The nitrogen / carbon ratio, normalized to the ratio measured at normal incidence between the detector and the surface normal, is plotted as a function of take-off angle. A high N/C ratio at glancing incidence indicates a concentration of nitrogen



near the surface of the film, implying that the nitrogen-rich region of the BAT is oriented away from the gold interface. As the proportion of BAT increases in the film, the degree of difference in the N/C ratio as a function of take off angle for both BAT/OEG (solid lines) and BAT/MHD (dotted lines) SAMs decreases.

The N/C ratio was chosen as an indicator of the position of the biotin moiety of the BAT molecule relative to the gold surface of the film because of the asymmetric distribution of nitrogen and carbon in the biotinylated thiol (see Figure 1-1 and Figure 3-16). For instance, if the biotin head groups of the BAT thiols in the SAMs are located near the surface, an increased N/C ratio would be expected when measuring at shallow TOA ( $\theta = 80^\circ$ ) relative to the N/C ratio taken at normal incidence ( $\theta = 0^\circ$ ), as the photoelectrons that are below 14 Å are greater than 90% attenuated at shallow TOA. As shown in Figure 3-18, the N/C ratio of the 100% BAT films does not vary with take off angle. This suggests that in these films the thiolates chains do not adopt a preferential orientation relative to the surface normal. In contrast, as increasing amounts of the OEG or MHD diluent are mixed into the SAM, the angular dependence was observed to increase. This indicates that 1) in mixed BAT SAMs, particularly those with low  $\chi_{\text{BAT,sur}}$ , the majority of the biotin headgroups can be found near the SAM surface, and 2) that in pure BAT SAMs, the biotin headgroups are uniformly distributed throughout the depth of the film.

High resolution C(1s) spectra (not shown) of 100% BAT films taken at normal ( $0^\circ$ ) and shallow take off angle ( $\theta = 80^\circ$ ) were essentially indistinguishable in the intensity of the peak(s) between ~288 – 288.5 eV (caused by the carbonyl- and ureido- type C atoms,

respectively) relative to the major unresolved doublet at 285 - 286.5 eV (resulting from alkyl- and ether-type C atoms, respectively.) Consistent with the data from elemental ratios, this lack of angular dependence in the high-resolution C(1s) spectra shows that the biotin is uniformly spread through the film depth.

To determine if this uniformity is caused by either "hairpinning" of the BAT by coordination of both the sulfhydryl and the biotin thioether to the surface or by non-specific physisorption of BAT, high resolution sulfur spectra were taken at both normal and glancing incidence from 100% BAT films. Whereas the spectrum taken at a take-off angle of  $80^\circ$  showed only one peak (actually a doublet) centered around  $\sim 164$  eV, the spectrum taken at a take-off angle of  $0^\circ$  had distinct peaks at 164 eV and 161.8 eV (see Figure 3-19.)

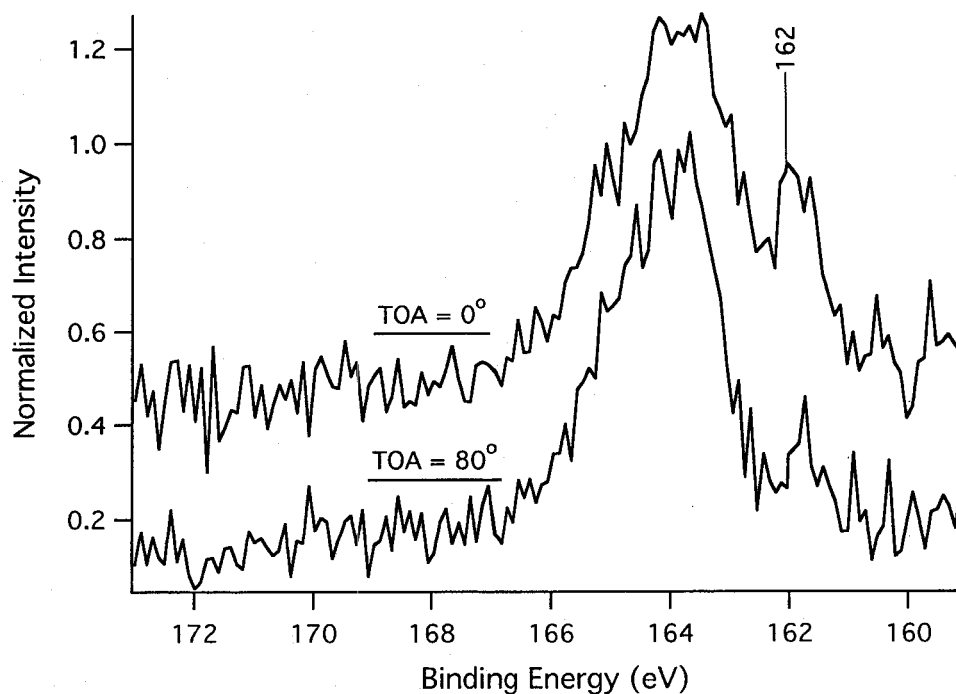


**Figure 3-19: High resolution sulfur spectra from BAT SAMs**

Sulfur photoelectrons collected at  $80^\circ$  TOA are predominated by a 164 eV binding energy, attributed to uncoordinated sulfur atoms. Spectra collected at normal incidence include a smaller peak centered around  $\sim 162$  eV, attributed to chemisorbed sulfur atoms.

The presence of the bound sulfur species that is detectable only at normal incidence indicates that the sulfur species near the gold/thiolate interface is indeed chemisorbed. The other S species that is not bound to gold ( $\sim 164$  eV) is clearly near the surface of the SAM since its signal is strongest at  $80^\circ$ . This demonstrates that the BAT thiol is chemisorbed at the gold / SAM interface and that only one end of the molecule is bound to the interface and not “hairpinned”. This result does not rule out the binding of the biotin thioether to the gold surface, but, as discussed previously, the thioether group in biotin binds to gold weakly, if at all, and it is readily displaced by sulfhydryl-based thiolates.

This depth profile analysis was further supported by the high-resolution oxygen spectra. Figure 3-20 shows how the intensity of the oxygen signal varies as a function of take-off angle for a representative series of BAT/MHD SAMs. In this case, it is the difference between the normal and glancing incidence that illustrates the variation in oxygen concentration. Note how the variation is greatest at intermediate  $\chi_{\text{BAT,Sur}}$ , and declines essentially no difference in pure BAT SAMs. An interesting point that will be relevant later when the SPR measurements of protein dissociation are discussed, is that the maximum difference in the high-resolution oxygen spectra occur at approximately 55% surface BAT.

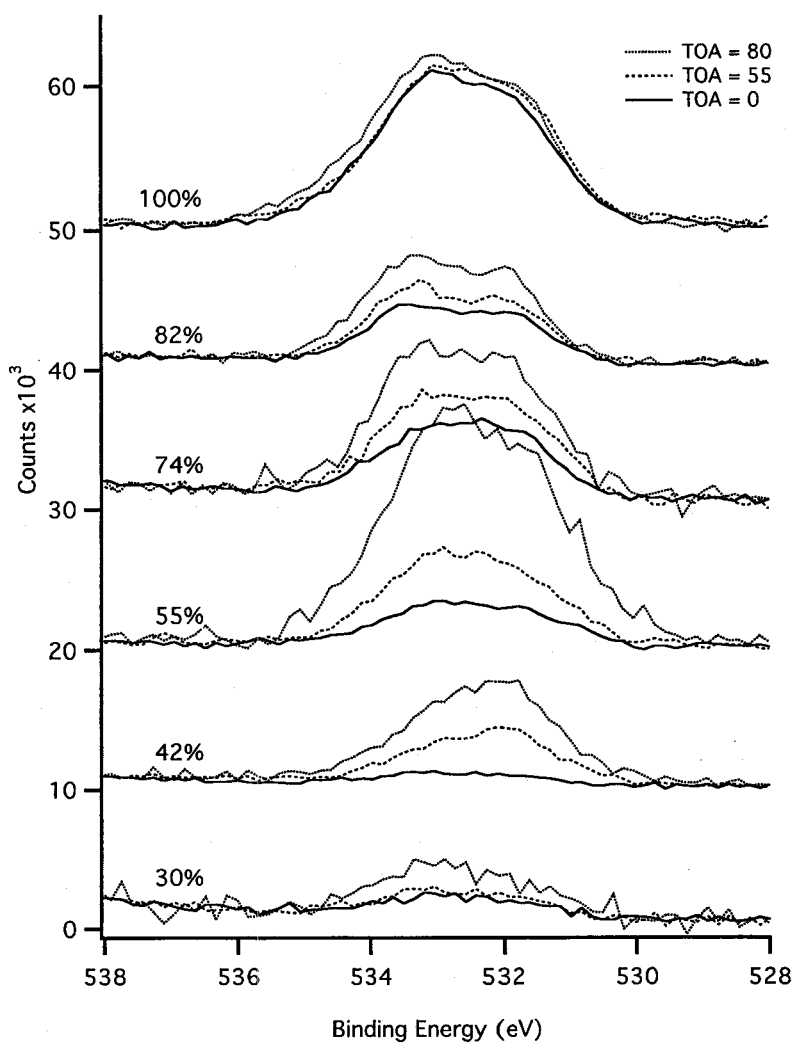


**Figure 3-20: Angular dependent XPS oxygen spectra from mixed BAT/MHD SAMs.**

The surface percentage of BAT in mixed BAT / MHD SAMs is shown. Those spectra from surface percentages greater than 30% are offset by multiples of  $10^4$  counts for clarity. The spectra collected from TOA  $> 0^\circ$  have been scaled so that the baselines match those from the normal incidence spectrum for comparison purposes. TOA from all the surface compositions are indicated in the legend.

This maximal difference between glancing and normal incidence indicates that at this surface percentage BAT, the highest proportion of BAT molecules were correctly oriented.

### **Depth profile analysis by deconvolution of ARXPS data**

Additional supporting evidence for the changes in thiolate orientation as a function of surface composition (i.e., the identity of the diluent thiolate) and surface composition was provided by carrying out a mathematical deconvolution of the angle-resolved composition data. This analysis is based on the tools developed by Tyler et. al and are described in detail elsewhere (Tyler, Castner et al. 1989). Briefly, a mathematical model was derived based on the known attenuation of photoemission intensity (Eq. 3) that attempts to deconvolute the composition data collected at the different TOA to create a model depth profile that best fits the data. Five different ARXPS data sets (from five different surface compositions) were fed into this deconvolution algorithm; the output from these analyses are presented in Figure 3-21 through Figure 3-25.

Beginning with a pure MHD SAM, the ARXPS deconvolution analysis suggests that the carbon in the film is concentrated near the surface, the sulfur is present mainly near the gold interface, and the film is approximately 18 Å thick (Figure 3-21). This is consistent with previous studies which have shown that MHD SAMs assemble into a highly ordered, regular, close-packed array (Bain and Whitesides 1988; Bain, Biebuyck et al. 1989; Bain, Troughton et al. 1989). (The thickness estimate determined by the deconvolution algorithm is obtained from the intersection of the carbon and gold traces

and is very sensitive to the value of the smoothing parameter used, and is therefore only approximate. Nevertheless, in this case the value is quite close to more direct measurements of the film thickness of  $\sim 16 \text{ \AA}$  (below) and to those reported in the literature ( $20 \text{ \AA}$ ).

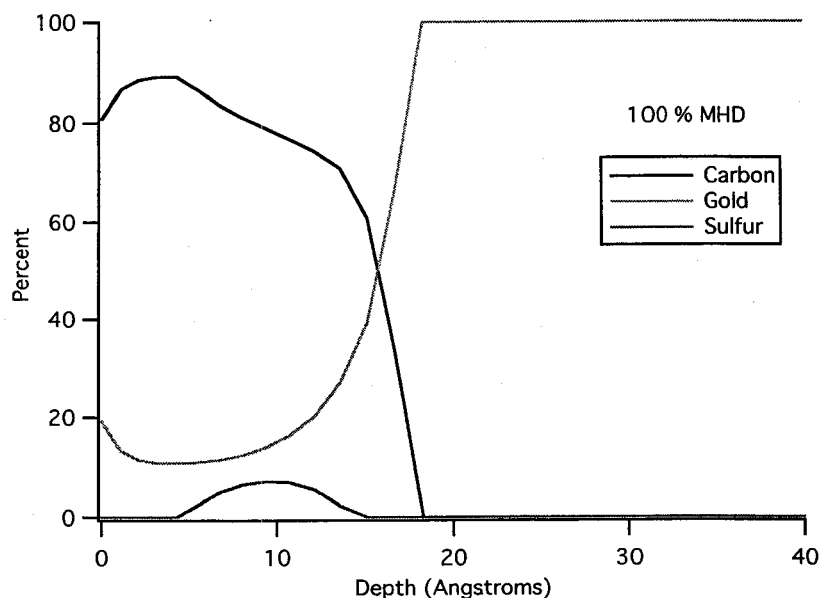


**Figure 3-21: Deconvolution analysis of 100% MHD ARXPS data**

The three traces represent the three elements measured in the XPS data: carbon, sulfur and gold.

The results shown in Figure 3-21 basically represent a test case for the deconvolution analysis. The MHD SAMs have been shown to be well-behaved, that is, that they assemble into regular structures with the sulfur strongly coordinated to the gold surface and the aliphatic regions close-packed and regularly oriented. According to the deconvolution results shown in Figure 3-21, carbon is concentrated at the interface and the upper regions of the film, sulfur is near the gold surface, and the films thickness is

around the expected value. The next case to test is a BAT / MHD mixture. Figure 3-22 shows the deconvolution analysis obtained from the angle-resolved composition data obtained from a ~55% BAT / 45% MHD SAM.

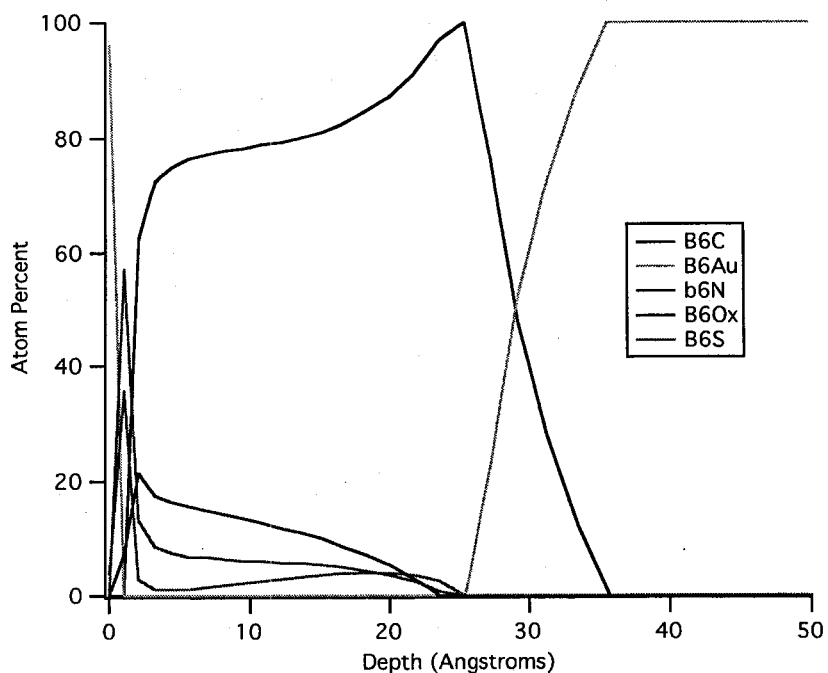


**Figure 3-22: Deconvolution analysis for 55% BAT / MHD ARXPS data**

The addition of the BAT thiolate brings nitrogen and oxygen into the equation. The spikes in the concentrations near the interface are artifactual and are caused by instability in the output of the mathematical model and can be safely ignored.

The following observations are made from this analytical result: 1) carbon is concentrated deep in the film, indicative of proper orientation of the mixed BAT/MHD SAM, 2) oxygen and nitrogen are enriched near the surface, again as expected for proper orientation of the BAT thiolates, and 3) the estimated film thickness is 29 Å, consistent with a SAM that contains roughly half BAT. These observations suggest that at this

composition, there is still some of the expected orientation of the BAT thiolates, leading to the increased oxygen signal at the interface. The relatively uniform distribution of the oxygen and nitrogen signals is consistent with the BAT thiolate's elemental distribution (see Figure 1-1), though it does suggest a modicum of disorder / random orientation of the BAT chains near the surface of the film. This would not be unexpected in a high vacuum environment in which the ends of the BAT chains are not close-packed (on account of the short-chain MHD diluent "spacers".)

Moving now to the pure OEG SAMs, the reader is referred to Figure 3-23.

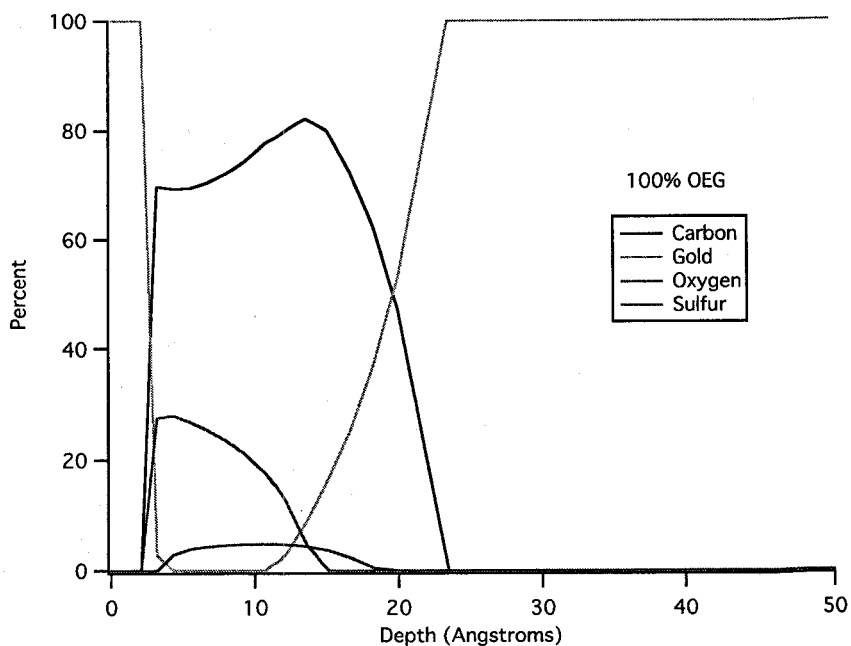


**Figure 3-23: Deconvolution analysis for 100% OEG ARXPS data**

As in Figure 3-22, the surface profile is unstable. Nevertheless, it is clear that oxygen is strongly enriched near the interface, and carbon is enriched further down in the film. The nearly uniform distribution of the sulfur signal is likely a result of the low density



of these films (see below) and the weak sulfur XPS cross-section which leads to relatively weak and noisy sulfur signal.

This ARXPS deconvolution result indicates that the OEG thiolates are oriented properly, concentrating the oxygen signal near the interface. Note that the estimated film thickness is  $\sim 20$  Å, only marginally thicker than the MHD film, suggesting a relatively low density for the OEG SAMs. This could be caused by a relatively high mean molecular area (MMA), which is further supported by independent measurements of film thickness (see below.)

Mixtures of BAT / OEG thiolates also appear to be relatively well-oriented, as shown in the deconvolution results in Figure 3-24

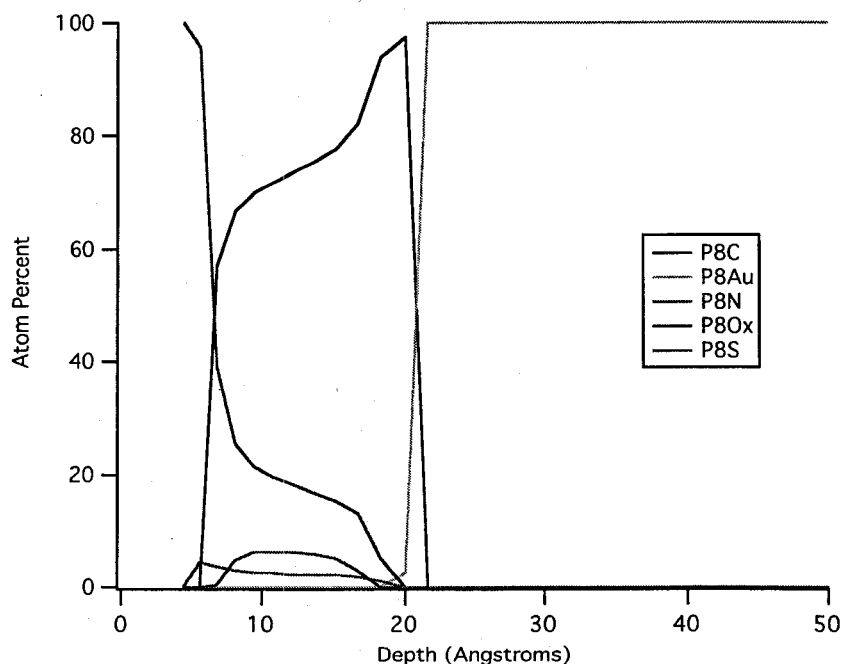


**Figure 3-24: Composition depth profile deconvolution plot of 45% BAT / OEG SAM**

In this case oxygen is quite highly enriched at the surface, as expected for properly oriented BAT and OEG thiolates. The strong oxygen signal at the interface, in comparison to the nearly uniform distribution of nitrogen, is almost certainly primarily caused by the OEG thiolates in the SAM.

From this result, we conclude that: 1) the oxygen signal is strongest at the surface, is much lower, though nearly constant, at intermediate depths of the film, and drops off rapidly 3-4 Å above the gold interface, entirely consistent with proper orientation of the OEG thiolates, 2) nitrogen signal is distributed essentially uniformly throughout the monolayer, but drops off significantly 3-4 Å from the gold interface, consistent with proper orientation of the BAT thiolates, 3) the highest carbon signal is at the gold interface, also consistent with orientation of the BAT / OEG thiolates.

This deconvolution result suggests that the monolayer assembled as expected, with the oxygen-rich termini of the OEG thiolates near the surface, and the BAT nitrogen signal distributed nearly evenly throughout the film. Interestingly, even though this film contains nearly half of the long chain BAT thiolates, the estimated film thickness is only 21 Å. This contrasts with other, more direct measures of film thickness, and could be the result of the strong smoothing parameter used by necessity to maintain stability of the model; stronger smoothing parameters were observed to decrease the estimated film thickness

The final case tested is a pure BAT SAM. The results of this analysis are shown in Figure 3-25. Here we see a nearly uniform distribution of the elements throughout the

depth of the film. This is consistent with the conclusions from the ARXPS N/C analysis (Figure 3-18) and the angle-resolved oxygen detail scans Figure 3-20)

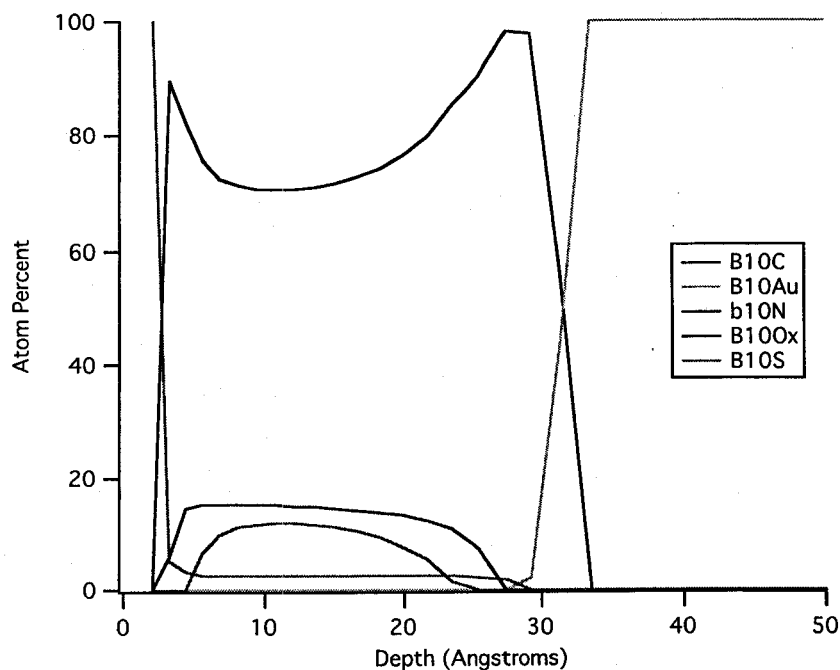


**Figure 3-25: Deconvolution analysis for 100% BAT ARXPS data**

Note the uniform distribution of the elements throughout the majority of the film, with a somewhat enriched proportion of carbon at the gold interface.

In addition to these observations, we note that the carbon signal increases near the surface (with the signal at the interface ignored due to known instability of the deconvolution algorithm). This leads to the proposal that the disorder / random orientation of the BAT thiolates is limited mainly to the region not directly tied to the gold surface via the sulfhydryl / gold coordination bond. Based on these observations, this analytical result suggests that the BAT thiolates are not fully extended nor uniformly oriented with respect to the surface normal.

These data are consistent with a structure of mixed BAT SAMs that has the functional endgroups at the interface, as desired, except in pure (and perhaps very high density) BAT SAMs, which do not appear to regularly orient the biotin groups toward the film surface.

Another structural characterization that complements the data already presented was performed at the synchrotron in Bethesda Maryland to evaluate the regularity of chain bond angles.

### ***NEXAFS evaluation of intra-thiolate bond orientation***

Chain packing arrangements within the monolayer can be regular or irregular. Figure 3-26 suggests how these two different arrangements could be visualized; the left illustration shows regular, ordered bond orientations that are uniform throughout the film, the right illustration shows how the bonds could be irregularly oriented in the film (but the biotin end groups, in this case, are still oriented away from the gold interface.) The protein binding activity of the mixed BCMs could be affected by whether the chain packing was regular or irregular mainly by affecting the availability of the functional end groups to potential binding partners (proteins) colliding with the surface. NEXAFS measurements were undertaken to evaluate the degree of uniformity of chain alignment in several different monolayer compositions. Depending on whether the NEXAFS spectra exhibited an angular dependence (that is, whether the data differed when collected at different angles between the incident beam and the surface normal,) the two possibilities

could be distinguished. Uniform bond orientation would lead to strong angular dependence, whereas random orientation would strongly suggest random chain orientation.

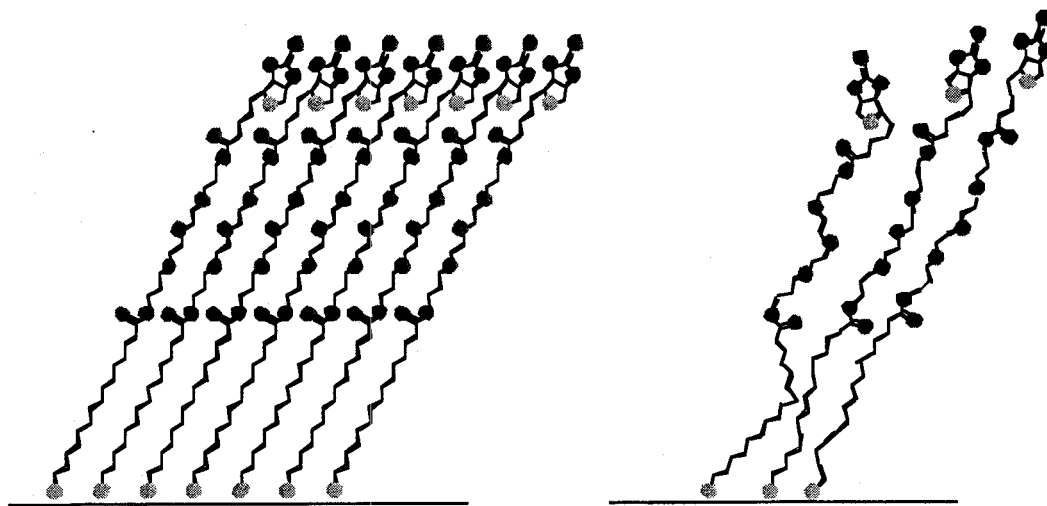


**Figure 3-26: Alternative models for chain packing and bond alignment**

The NEXAFS evaluation described herein was undertaken to distinguish between the two possible film “architectures;” regular bond packing and orientation (shown at left), and irregular orientation (right).

Beginning once again with the reliable test case using MHD SAMs, it was observed that these films indeed show a strong angular dependence in the absorption spectra (Figure 3-27) This is consistent with the previously described structure of MHD SAMs, which have been shown by various means to be close-packed and regularly aligned with respect to the surface normal.

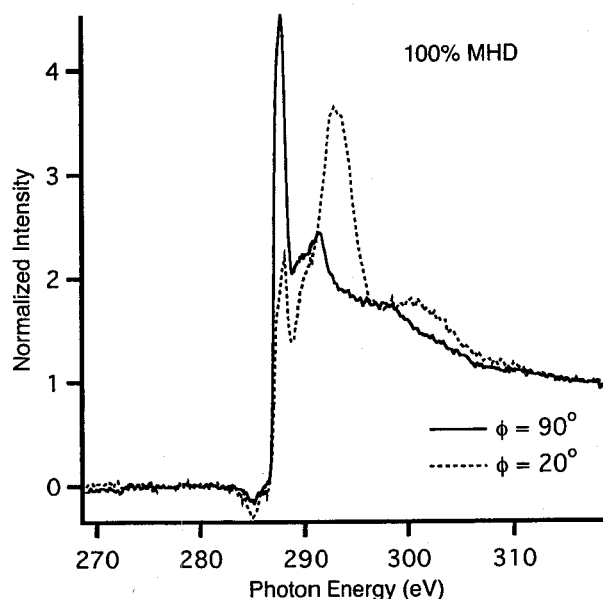


**Figure 3-27: Angle resolved carbon NEXAFS spectra of MHD SAM.**

Note the strong angular dependence at 288 eV and 294 eV (see Methods section for peak assignments.)

Comparing now the results in Figure 3-27 to those in Figure 3-28. The latter data come from a pure OEG SAM. In contrast to the MHD SAM, the OEG SAM exhibits very weak angular dependence in the carbon absorption spectra. This indicates that compared to the MHD thiolates, the OEG thiolates are less well ordered, if not nearly completely randomized. Incidentally, this random orientation of the OEG thiolates is one way to explain their ability to resist non-specific protein adsorption by invoking an argument that states that imposing a higher degree of order on them as a result of decreased mobility upon protein binding leads to a high energetic cost to protein binding, hence, resistance to protein binding.

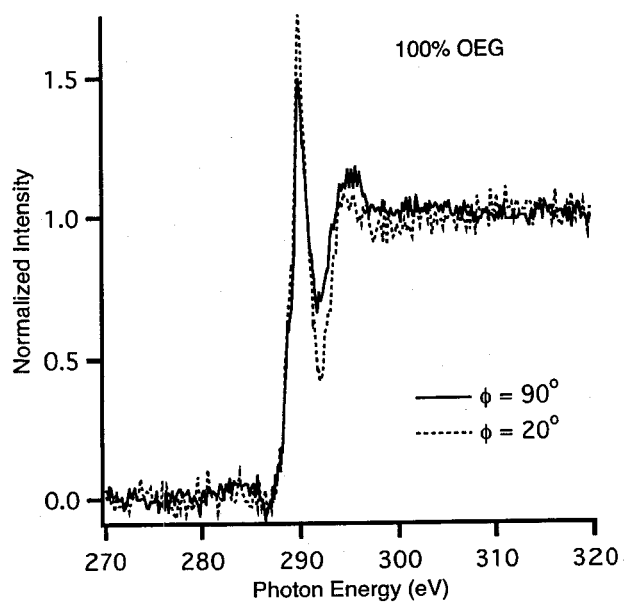


**Figure 3-28: NEXAFS spectra of OEG SAMs.**

Note the significantly weaker angular dependence compared to the MHD SAMs.

Moving ahead to the pure BAT SAMs in Figure 3-29, again the NEXAFS data suggest a weak, if not absent, average chain orientation. This is consistent with the ARXPS data and depth profile deconvolution analysis that suggest random *chain* orientation, which could only occur if the *bond* orientation is also random.

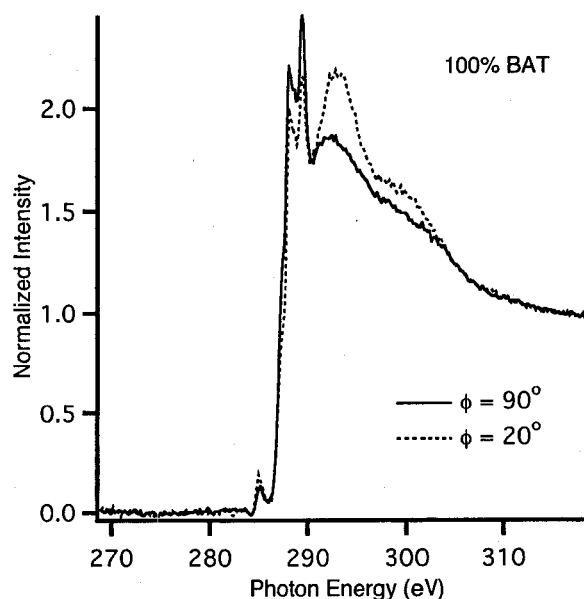


**Figure 3-29: NEXAFS spectra taken from pure a BAT SAM.**

NEXAFS spectra were also collected from mixed BAT / MHD and BAT / OEG SAMs. Figure 3-30 presents the data obtained from a mixed BAT / MHD SAM. The figure shows a relatively strong angular dependence in the carbon absorption spectrum. By comparison to the BAT NEXAFS spectra (Figure 3-29) we conclude that the aliphatic portion of this SAM well ordered, more similar to a pure MHD SAM than a pure BAT SAM. This suggests that the MHD chains are promoting close-packing the BAT thiolates. In contrast, the mixed BAT / OEG NEXAFS data (Figure 3-31) does not exhibit a strong angular dependence. It is concluded from this that, according to the ARXPS data, the OEG thiolates promote satisfactory orientation of the BAT chains, but



from the NEXAFS data, they do not induce regularity in the orientation of the bond angles.

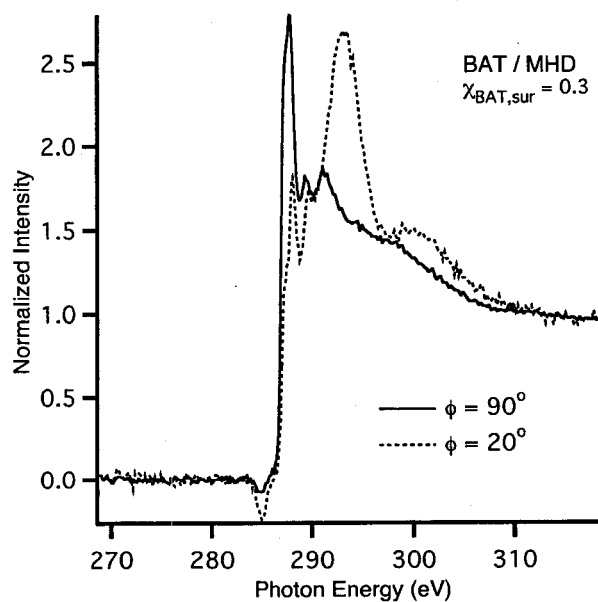


**Figure 3-30: NEXAFS spectra of mixed BAT / MHD SAM.**

Again a relatively strong angular dependence is seen, at least in the aliphatic regions of the SAM.

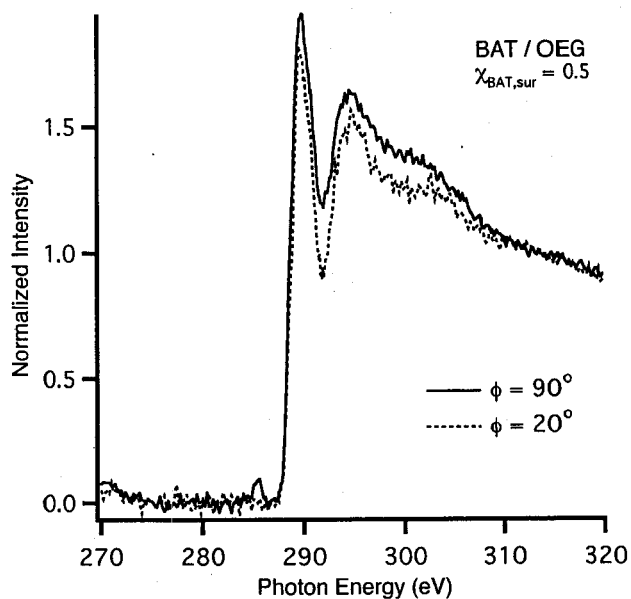


**Figure 3-31: NEXAFS spectra of mixed BAT / OEG SAM.**

Once again, consistent with the results obtained from the pure BAT and pure OEG SAM, weak angular dependence is seen, suggesting that the mixed BAT / OEG SAMs are not regularly structured.

In summary, the following observations and conclusions were made: 1) the degree of uniformity of bond alignment varied from a high degree to essentially undetectable, with a high uniformity of bond alignment occurring in SAMs containing the MHD diluent showed the highest degree of uniformity, 2) SAMs containing the OEG diluent or pure BAT showed the least amount of uniformity.

This data helps establish a more detailed understanding of the molecular architecture of the different film compositions, and suggests that the addition of the MHD thiol, but not the OEG thiol, induces tight packing, or, at least, regular bond orientation in mixed BCMs.

### ***Determining thickness of BAT / OEG and BAT / MHD SAMs***

The final structural characterization of mixed BCMs undertaken was a measurement of adlayer thickness. The reason for carrying out this analysis, in addition to basic characterization of the composition and structure of these films, is that their use for controlling the non-specific and selective immobilization of proteins is dependent on the ability to control the surface chemistry. The types of chemical groups exposed to solution will be determined, in part, by the packing density (thickness) of the monolayers. If the packing density is low, it is possible that undesirable properties, such as non-specific protein binding, will be exhibited by the monolayers. Conversely, if the packing density is high, it is less likely that chemical groups other than the end groups selected by choosing a specific thiol will contribute to the chemistry of the interface. Therefore, the packing density measurements will provide additional information upon which to develop a consistent picture of the architecture of the monolayers, and determine whether they would be effective at controlling the protein binding properties of the interface.

The packing density of SAMs of various composition were determined by two independent methods: XPS gold signal attenuation and SPR wavelength shift during SAM assembly.

The film thickness data for BAT/OEG SAMs as measured using photoelectron attenuation and SPR measurements is summarized in Figure 3-32.

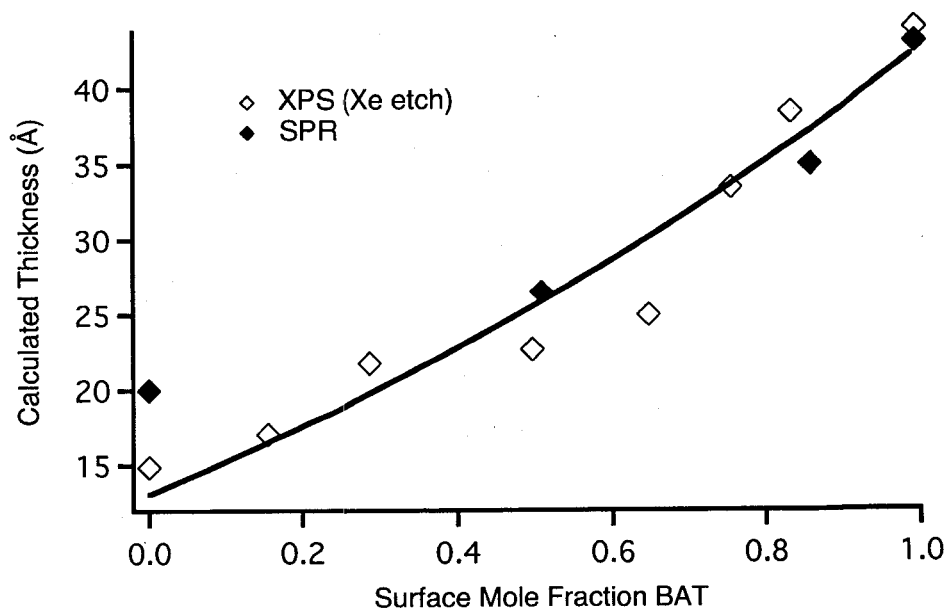


**Figure 3-32: BAT / OEG SAM film thickness as determined by XPS and SPR**

Film thickness was determined by comparing the XPS gold intensity of mixed SAMs before and after sputtering *in-situ* (open diamonds) and measuring the SPR minimum wavelength shift as the films adsorb from solution on a clean gold surface (filled diamonds.) These two different methods rely on different assumptions about the instrument response to film thickness; the first is dependent on assumptions made about the mean free path of gold photoelectrons in the different compositions of films, the second method relies on assumptions made about the index of refraction of the assembled monolayer. Note the good agreement of the two methods, despite their different assumptions, and the quality of fit to the thickness model (solid line.)

The thickness of the mixed BAT / OEG SAMs varied smoothly, as expected, with the addition of increasing amounts of the long chain constituent (BAT.) Notably, the thickness of the BAT SAM is  $\sim 45$  Å, consistent with a relatively low density chain packing (compared with MHD SAMs), in agreement with the data obtained by the ARXPS and NEXAFS results.

While apparently linear, we propose a model for explaining the film thickness data. This model is described in detail below.

### Mathematical model of thiolate film thickness

The thickness ( $d$ ) of BAT/OEG films was determined by relating the Au(4f) intensity measured while the film is present ( $I$ ) to the Au(4f) intensity after sputter cleaning the surface ( $I_0$ ) described in equation 3<sup>1</sup>:

$$I = I_0 e^{-d/\lambda \cos \theta} \quad (3)$$

where  $\lambda$  is the mean free path of Au photoelectrons (42.5 Å with 1486.6 eV photons) and  $\theta$  is the angle in degrees between the surface normal and the detector aperture. The thicknesses are shown versus  $\chi_{\text{BAT,sur}}$  for the BAT/OEG films in Figure 3-32. To fit this data, a relationship has been derived between the composition of a mixed SAM composed of thiols with different lengths and its average thickness,  $d$ , which is:

$$d = f_B t_B + f_D t_D \quad (4)$$

where  $f_i$  is the fraction of the surface area occupied by thiolate  $i$ ,  $t_i$  is the thickness of a pure SAM composed of thiolate  $i$ , B is BAT and D the diluent thiolate (OEG in this case). Note that  $f_i = A_i N_i$  where  $N_i$  is the total number of thiulates  $i$  per unit area and  $A_i$  is

---

<sup>1</sup> This is the same equation as stated earlier in the depth profiling section and is restated here for convenience. The equation number used is the same for both.

the area occupied per thiolate  $i$ , which we will assume here to be equal to  $A_i$  in a pure monolayer of  $I$  (i.e. we assume that each type of molecule on the surface occupies the same area, independent of its neighbors). If  $N_i$  is expressed as  $\chi_{i,sur} * N_{tot}$ , where  $N_{tot}$  is the total number of thiolates (B+D) per unit area, then:

$$d = (A_B t_B \chi_{B,sur} + A_D t_D \chi_{D,sur}) N_{tot} \quad (5)$$

$A_i t_i$  is the molecular volume,  $V_i$ , and  $N_{tot}$  is just  $N_{tot}^B \chi_B + N_{tot}^D \chi_D$ , where  $N_{tot}^i$  is the packing density of a pure  $i$  SAM, so that:

$$d = (V_B \chi_{B,sur} + V_D \chi_{D,sur}) (N_{tot}^B \chi_{B,sur} + N_{tot}^D \chi_{D,sur}) \quad (6)$$

Equation 6 was used to fit the thickness data from the BAT/OEG SAMs versus *surface* percentage of BAT as shown by the curve in Figure 3-32. The fit results in values of 0.0238 molecules/Å<sup>2</sup>, 0.0423 molecules/Å<sup>2</sup>, 557 Å<sup>3</sup>/molecule, and 985 Å<sup>3</sup>/molecule for the parameters  $N_{tot}^D$ ,  $N_{tot}^B$ ,  $V_D$ , and  $V_B$ , respectively. These values of  $V_D$  and  $V_B$  correspond to bulk densities of 1.12 gm/cm<sup>3</sup> and 1.21 gm/cm<sup>3</sup>, respectively. This value for OEG compares well to the measured bulk density of 1.13 gm/cm<sup>3</sup>. Note that the packing densities estimated from the XPS thickness of the pure OEG and pure BAT SAMs (using these bulk densities) are  $2.7 \times 10^{14}$  molec./cm<sup>2</sup> and  $4.0 \times 10^{14}$  molec./cm<sup>2</sup>, respectively. The inverse of the parameters  $N_{tot}^D$  and  $N_{tot}^B$  give the mean molecular areas ( $A_i$ ) for OEG and BAT,  $\sim 42$  Å<sup>2</sup>/molecule and  $\sim 24$  Å<sup>2</sup>/molecule, respectively.

Also shown in Figure 3-32 are thickness of pure and mixed SAMs, measured in-situ by following the shift in the SPR wavelength upon adsorption from ethanol solution. (These shifts were converted to absolute thickness following (Jung, Campbell et al.

1998), using a refractive index for OEG of 1.48 measured in (Jung, Campbell et al. 1998; Nelson, Gamble et al. 2001). We assumed here a refractive index for the BAT of 1.49 to give the same thickness for the pure BAT film as measured by XPS. We also assumed that the BAT and OEG had the same densities, 1.13 (Jung, Campbell et al. 1998; Nelson, Gamble et al. 2001)). These SPR thickness are similar to those from XPS. For comparison, a thickness of 2.5 nm was reported based on XPS for a thiol identical to this OEG but with two more  $-\text{OCH}_2\text{CH}_2-$  units; and an ellipsometric thickness of 3.5 nm was reported for a pure monolayer of a molecule identical to this BAT but shorter by one  $-\text{CH}_2\text{CH}_2\text{O}-$  unit.

To summarize, the results of the film thickness analysis have shown that in general, the data resulting from the XPS and SPR measurements, based on very different assumptions, were in agreement. The thickness of the different films increased with increasing proportion of the long-chain BAT thiolate in the film, varying from a thickness commensurate with the length of the short-chain diluent to the length of the BAT thiolate itself. The overall thickness of the BAT SAM was significantly less than expected assuming that the chain is fully extended and canted at  $30^\circ$  from the surface normal, as has been reported elsewhere to be the case for pure MHD SAMs.

### ***Chapter Summary and Conclusions***

Taken together, the results presented in this chapter helped us to develop an understanding of both the chemistry and the structure of single- and binary-composition

and binary composition self-assembled monolayers generated from the thiols we chose. While the chemistries of the SAMs, strictly in terms of the elemental composition of the adlayer, was a relatively straight-forward outcome, the structure of the films was determined to be remarkably varied. Figure 3-33 depicts the different structural models developed from the surface analysis data.

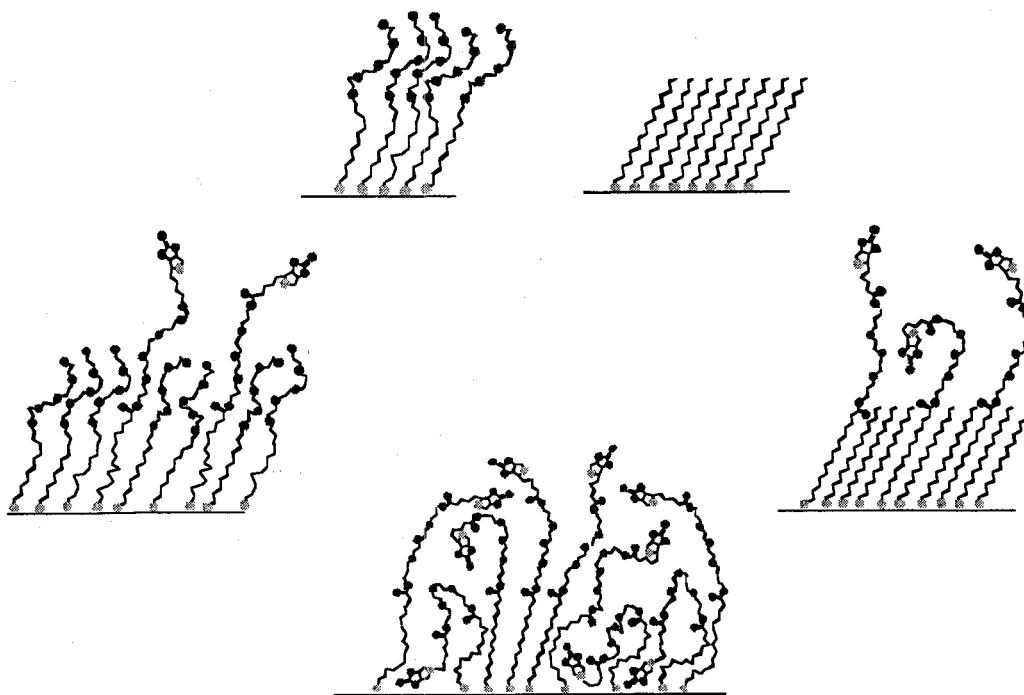


**Figure 3-33: Conceptual illustrations of five representative pure and mixed SAMs**

Clockwise from upper right: 1) pure MHD, 2) mixed BAT / MHD, 3) pure BAT, 4) mixed BAT / OEG, and 5) pure OEG. The diagrams are meant to suggest possible configurations of the thiolate chains that are consistent with the ARXPS and NEXAFS data.

The five different illustrations in Figure 3-33 were chosen to represent the five different test cases for which data was presented in this chapter: each of the three single-composition SAMs, and the two mixed composition SAMs. To generalize our findings,



we determined that the surface chemistry of the substrate could be controlled by assembly of these films, and that the chemistry can be measured using XPS. A key result of the XPS composition analysis is that the thiolate ratio of BCMs can be determined by measuring the nitrogen content of the film. This allowed us to later produce films of known composition without further XPS analysis, and it allowed us to compare the properties of different composition SAMs based on the density of BAT in the film, an operational parameter in terms of our objectives of controlling streptavidin binding.

The angle-resolved XPS data suggested that whereas the MHD and OEG SAMs appeared to orient their endgroups away from the solid surface as desired, the biotin terminus of pure BAT SAMs is poorly oriented, i.e., it was “mixed” throughout the depth of the film. However, orientation of the biotin terminus to the “top” of the film (i.e., opposite the Au-SAM interface) was promoted by the addition of shorter diluent thiolates. This result implies that for proper control over the interfacial chemistry using the BAT thiolates, mixed monolayers should be used.

The NEXAFS measurements supported the general view that MHD containing SAMs possess fairly regular inter-chain packing but that OEG containing (or pure BAT) SAMs did not. However, the addition of MHD to BAT SAMs promoted the regular packing of the methylene region of the adlayer. This regular packing appeared to be promoted, though to a lesser extent, by mixing the OEG thiol with BAT. Pure BAT containing SAMs are not as regularly packed as OEG, mixed BAT / OEG, mixed BAT /

MHD or pure MHD SAMs, consistent with the ARXPS results that indicate the biotin groups are distributed throughout the depth of the film.

We also determined that the film thickness increased with the addition of the longer BAT thiol, and the relationship between film thickness and composition could be described by a mathematical model assuming a constant packing density for the different thiolates and the way that these different packing behaviors interact in mixed SAMs.

These measurements present a detailed picture of the composition and architecture of the SAMs at various compositions. The next step is to determine whether these SAMs will bind streptavidin from solution, and, if so, how the composition and architecture of the various SAM compositions affect protein binding.

## 4. Protein Binding and Desorption

The ability to control the chemistry of gold surfaces has been demonstrated, and the architecture of the self-assembled monolayers used to affect this control has been characterized in detail. We now move on to evaluating how these monolayers interact with protein solutions; specifically, the protein binding behavior at the surface / solution interface as determined by the surface chemistry and architecture. (see Figure 1-3, step two.) Recall that we are attempting to control two types of protein binding activity, both specific and non-specific (see Figure 3-1), and that the “activity” of the surface along each axis is hypothesized to be controlled by the proportion of the thiolate in the monolayer that contributes to the surface activity along that axis. For example, control over specific protein binding is expected to be achieved by varying the amount of the biotin-containing thiolate on the surface, whereas the surface’s resistance to protein adsorption is expected to be controllable by varying either the surface concentration of the other (“diluent”) thiol or its endgroup chemistry.

On top of this, so to speak, it will be necessary to confirm that the streptavidin adlayer is able to support the biotin-mediated coupling of additional protein ligands. This third layer is what is ultimately depended upon to mediate cell attachment. As this is the principle motivation driving this surface modification strategy, it will be important to also determine to what extent the streptavidin surface will promote or resist non-specific protein binding to itself.

## Chapter Aims

This chapter will focus on characterizing the behavior of proteins at the interface of an aqueous solution and the engineered interface. The important questions to be answered are:

1. Can non-specific protein binding be controlled using the OEG and MHD thiols, as expected?
2. Does an engineered surface that contains the biotinylated thiolate support the specific adsorption of streptavidin?
3. If so, is the amount of specific streptavidin adsorption controllable by varying the surface concentration of the biotinylated thiolate?
4. If so, what is the optimum surface composition for maximum streptavidin adsorption and avidity?
5. Can the streptavidin-functionalized surfaces be used to support specific (i.e., biotin-mediated) secondary protein adsorption?
6. To what extent do the streptavidin-functionalized surfaces promote (or resist) non-specific protein adsorption?

The outcomes of the experiments and measurements designed to answer these questions will establish the foundation for the next stage of experimentation: exploring the response of adhesion-dependent cells on proteins specifically immobilized on a substrate.

### **Overview of Surface Plasmon Resonance protein adsorption measurements**

There are a variety of experimental techniques for measuring protein adsorption on surfaces, each with their own strengths and drawbacks. One of the more versatile methods that these surfaces are particularly well suited for takes advantage of the optical properties of a metal surface. This method, known as Surface Plasmon Resonance (SPR), is a technique that takes advantage of optical properties of metal surfaces. Very briefly, lossy metal lattice electronic displacements driven by coupling between them and the oscillating electric field of photons impinging on the lattice result in decrease in reflected intensity of the illuminating beam. The decrease in intensity is a function of the overlap between the natural frequency of the lattice field and the wave vector of the incident photons; the better the match between the incident wave vector and the surface wave frequency, the stronger the coupling (and thus energy transfer) and the lower the reflected intensity. (Actually, it is the non-radiative loss of energy caused by decay in the electric lattice displacement amplitude that results in a decreased re-emission of photons from the surface.) Figure 4-1 gives an example of how the incident light is coupled to the plasmon wave through a prism, which is needed to match the wave vectors since light in air could not reach the velocity required to match the plasmon velocity, and a higher refractive index medium is required for coupling.

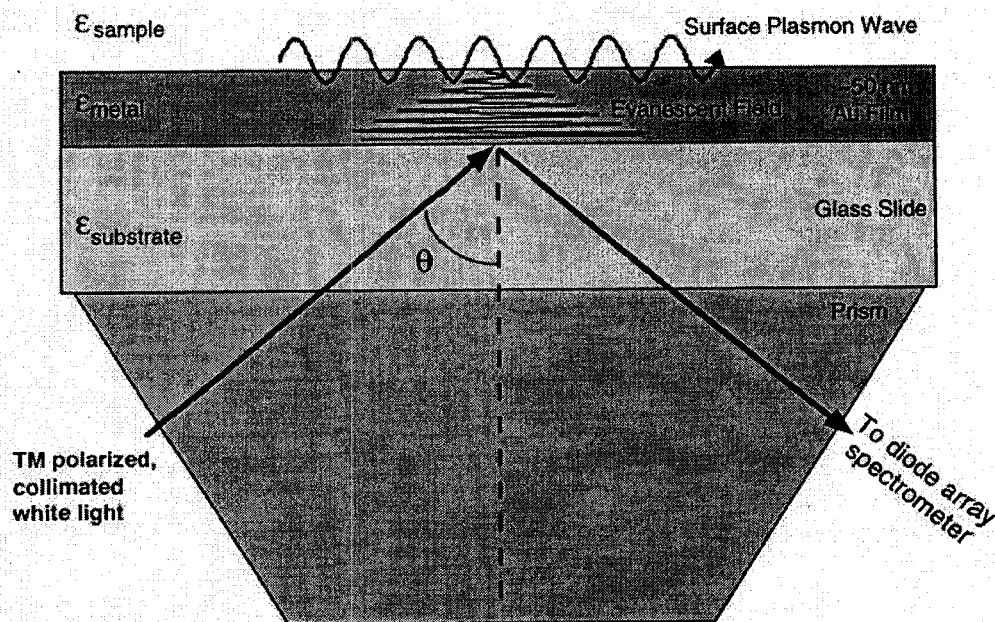


**Figure 4-1: Schematic illustration of SPR coupling device**

The key behavior of this phenomenon is that the natural frequency of the lattice electrons (according to Maxwell's equations describing the physics of electromagnetic energy) is required to match the optical properties on the other side of the interface (where, in this case, the aqueous solution exists.) It is the index of refraction on this side of the interface that determines the coupling frequency (i.e., the matching wave vector); as the index of refraction of the environment changes, so does the coupling frequency, and hence the surface plasmon coupling wavelength. Figure 4-2 shows how SPR reflectivity curve changes in response to an adsorbed protein layer.

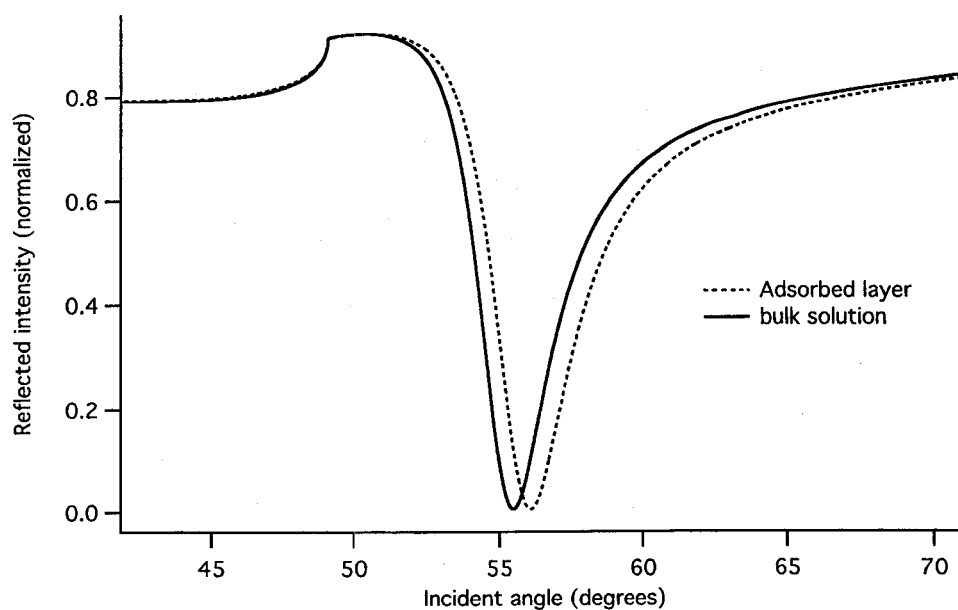


**Figure 4-2: Ideal SPR reflectivity curves for bulk solution and adsorbed protein layer**

These curves show how the reflected intensity changes as a function of incident angle for an ideal (theoretical) setup. As the incident angle changes, the wave vector of the incident light passes through a regime in which it matches the surface plasmon propagation velocity resulting in energy coupling and loss of reflected intensity. A similar result occurs if the incident light is not a single wavelength scanned through different angles but instead uses multiple wavelengths (white light) at a fixed angle, and measures the minimum wavelength (at which the optimal coupling occurs.) The solid line is the outcome when the interface has a refractive index equivalent to an aqueous buffer solution, the dotted line is the outcome that would occur with a 5 nm layer of index 1.5 (roughly equivalent to a monolayer of protein adsorbed on the surface.) The difference in reflected intensity provides a highest signal to noise ratio where the reflectivity curve is the steepest (vertical line.)

This method is particularly useful for the experimental system used for surface modification as it requires a metal interface such as gold, as does the self-assembly of alkylthiols, and is very sensitive to changes in refractive index near the interface, which occurs when protein, that has a bulk refractive index that differs from the aqueous

solution, binds to the functionalized surface. SPR was therefore used to determine how proteins interact with the various compositions of alkylthiolate monolayers.

### ***Characterizing and controlling non-specific protein adsorption***

#### **Non-specific protein binding can be controlled by diluent identity**

It has long been known that proteins in solution are highly active at interfaces, particularly hydrophobic interfaces. Indeed, this is a central tenet of the research strategy of the UWEB organization; that adsorbed proteins direct the behavior of cells that come into contact with the surface. Therefore, the ability to control the unspecific adsorption of proteins at an engineered interface is of paramount importance. Without at least some ability to control protein adsorption, the surfaces would be useless as an experimental system for studying cell/protein interaction. Therefore, the first step for validating the utility of these surfaces is to determine to what extent they promote or prevent non-specific protein binding. The proteins selected for these experiments are those which would be used for cell adhesion studies, mainly streptavidin, osteopontin (actually the "30N" amino-terminal fragment containing the RGD integrin binding tripeptide), and collagen type I.

Figure 4-3 presents the SPR response recorded when a pure OEG SAM was exposed to a 0.1 mg/mL solution of streptavidin. The data are presented as the calculated adsorption of protein (in ng/cm<sup>2</sup>) while the right axis shows the actual SPR minimum wavelength. Unfortunately, the minimum wavelength drifted upward during this experiment; however, the initial drift is constant throughout the data collection



(emphasized by the sloped line). Noting that the baseline drift is constant, any shift that occurs as a result of protein binding is negligible ( $<1 \text{ ng/cm}^2$  or  $< 1 \times 10^{10}$  molecules/cm<sup>2</sup> for a 52.8 kDa protein.)

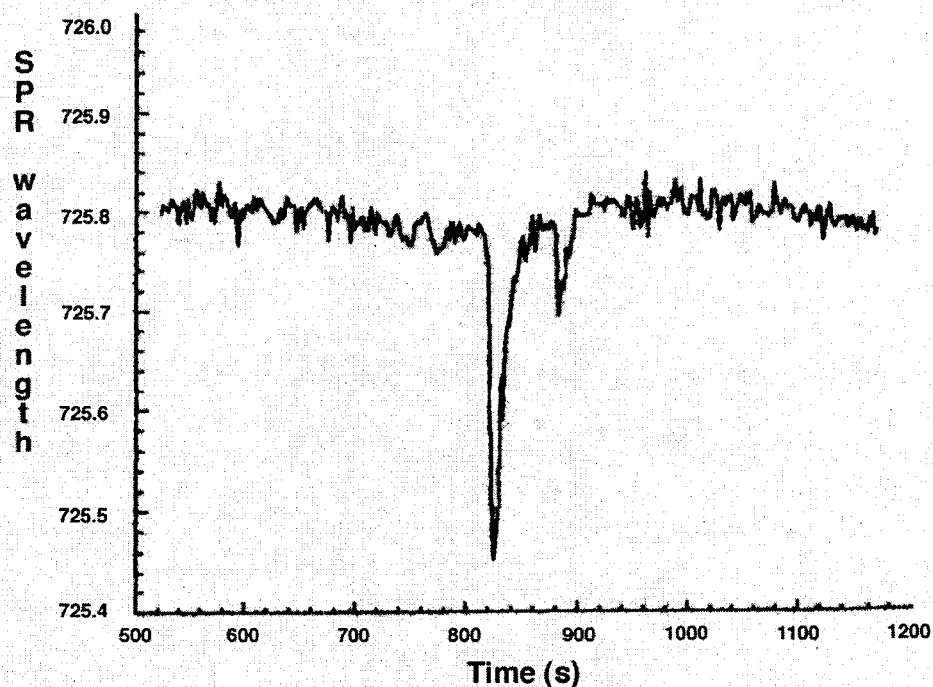


**Figure 4-3: OEG SAMs prevent streptavidin adsorption**

A solution of streptavidin was introduced into a flow cell above the OEG SAM but no change in the SPR minimum wavelength was observed. The baseline of the fluctuates somewhat in this experiment, but it occurs both before and after the protein solution into the flow cell, and is likely caused by temperature changes or other physical artifacts. No shift resulting from protein injection is detectable.

This result is one of several that confirm that the OEG SAMs will not support streptavidin adsorption. Other OEG SAMs were challenged with other proteins such as

bovine serum albumin and 10% fetal calf serum (actually a complex mixture of proteins). Whereas the OEG SAM was resistant to BSA, exposing the surface to FCS resulted in significant protein binding (data not shown). This result precludes the use of FCS in any cell culture experiments that aim to strictly control the surface protein composition.

In stark contrast to the results obtained from the OEG monolayer, the MHD SAMs do promote protein adsorption to the interface in significant quantities, as is clear from Figure 4-4.

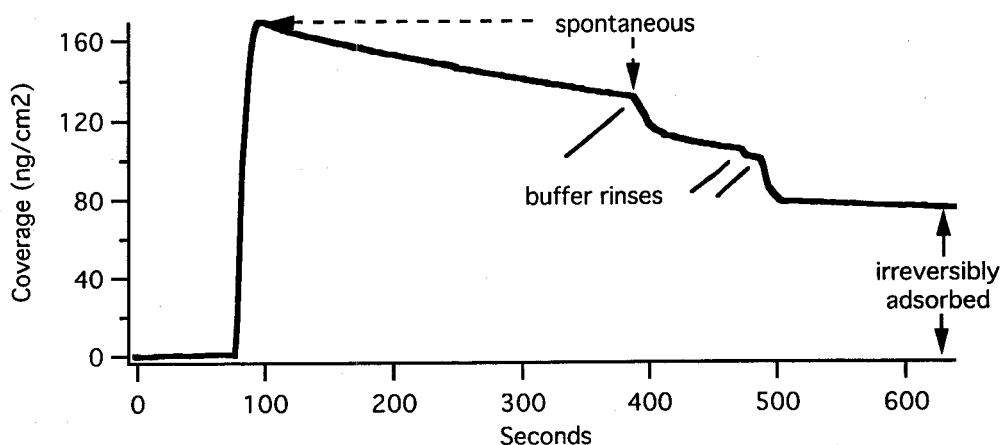


**Figure 4-4: MHD SAMs support (non-specific) streptavidin adsorption**

A solution containing streptavidin (0.1 mg/ml) was injected into the flow cell attached atop a MHD SAM. The change in the SPR minimum wavelength demonstrates protein binding directly to the surface as a result of non-specific interactions at the hydrophobic/aqueous interface. 22% of the protein that initially binds to the surface immediately and spontaneously dissociates, indicated by the drop in the SPR minimum wavelength. Following several buffer exchanges in the flow cell (rinses), approximately 45% of the adsorbed protein remains ( $\sim 75$  ng/cm<sup>2</sup>). The physical mechanisms underlying the spontaneous dissociation and irreversible binding are not evident from this data.

As expected based on a large body of research on protein adsorption to interfaces, the MHD SAMs presented an interface that supported a significant level of adsorption of streptavidin from solution (maximum binding reached 168 ng/cm<sup>2</sup>). Several different adsorption mechanisms are evident in Figure 4-4. The first large shift that occurred immediately after protein injection was followed by a period of either dissociation or restructuring, which resulted in a gradual return of the SPR minimum wavelength toward the initial value. After about 5 minutes of exposure to the protein solution the flow cell was flushed several times with buffer (not containing protein.) While these flushes tended to increase the rate of dissociation from the surface, eventually the SPR wavelength stabilized, implying the protein remaining was irreversibly bound. Further characterization of the mechanisms underlying these complex non-specific interactions were not within the objectives of this study. Suffice to say that this result confirms that the MHD thiols can be used to widen the range of surface characteristics available with the reagents used, and while our ultimate goal of cell adhesion studies precludes the use of surfaces that allow non-specific adsorption, the MHD thiols are a reagent that can be used to broaden the range of control over surface properties (see Figure 3-1) and as a tool for probing the nature of protein-surface interactions.

#### **Non-specific protein adsorption to mixed BAT / OEG SAMs**

Since most specific protein immobilization would be carried out using more complex surface mixtures of thiolates, generally including the BAT thiol, it was deemed

worthwhile to investigate whether BAT SAMs promoted or resisted non-specific adsorption. Figure 4-5 provides an example of such an experiment.

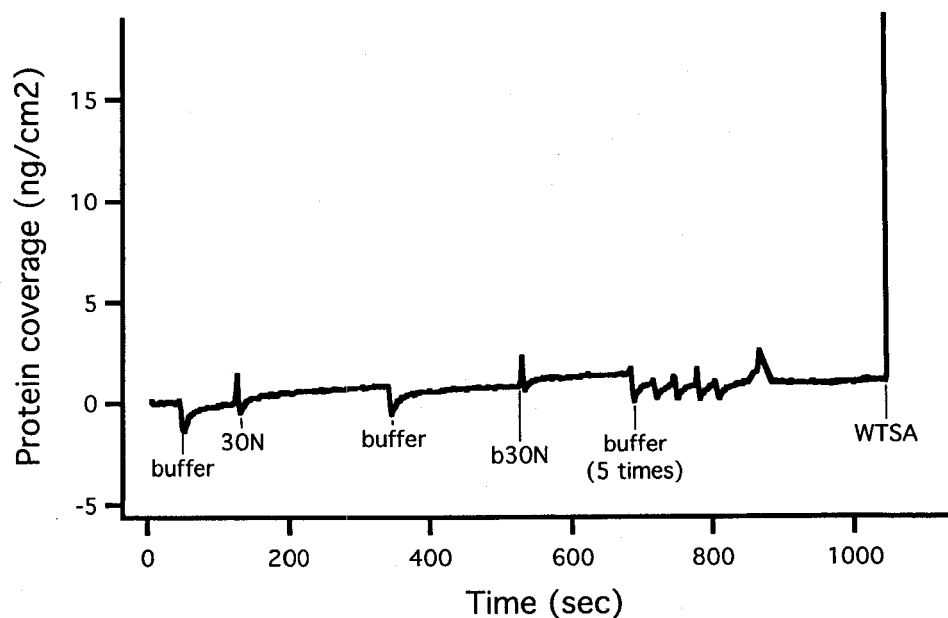


**Figure 4-5: 85% OEG / 15% BAT surface exposed to 30N osteopontin**

This experiment was undertaken to determine whether BCM would non-specifically adsorb a cell adhesion ligand planned for use in cell binding experiments. The SPR minimum wavelength baseline was established with a BCM containing ~15% BAT (OEG diluent). The surface was then challenged with a 1 $\mu$ M solution of the 30N osteopontin (30N) and a biotinylated 30N fragment (b30N). The amount of protein that adsorbed was estimated following aggressive buffer rinses. Judging from the change in SPR wavelength from the start of the experiment ( $t = 0$ ) to just before the streptavidin was injected ( $t \sim 1000$ ), slightly under 1 ng/cm<sup>2</sup> bound to the surface.

- There is some indication that the mixed BAT/OEG SAMs bind the 30N fragment non-specifically, albeit in very small amounts.

- A caveat is that there was a small refractive index mismatch between the buffer used to establish the baseline and the buffer the 30N and b30N were solubilized in (causing “spikes” rather than “dips” in the trace just after injection)
- Small changes in salt concentrations could cause both these spikes and possibly result in small permanent shifts in the baseline (due to physisorption on the surface for example)
- To be on the conservative side, the change is attributed to protein adsorption.
- The matter was left at this point, reasoning that the non-specific adsorption of proteins to the streptavidin adlayer would likely be more significant for cell attachment experiments, as the streptavidin layer would intervene between the cell receptors and whatever trace molecules might be on the surface.

### ***Characterizing and quantitating biotin-mediated streptavidin adsorption***

Equally, or not more important than controlling non-specific protein adsorption is the ability to stably and specifically bind streptavidin from solution. The next set of experimental results demonstrates that the addition of BAT to the assembling solution does indeed produce a film that will specifically and stably bind streptavidin.

### **Wild-type core recombinant streptavidin binds stably to BCMs with distinctive kinetics**

Let us begin with the results shown in Figure 4-6.

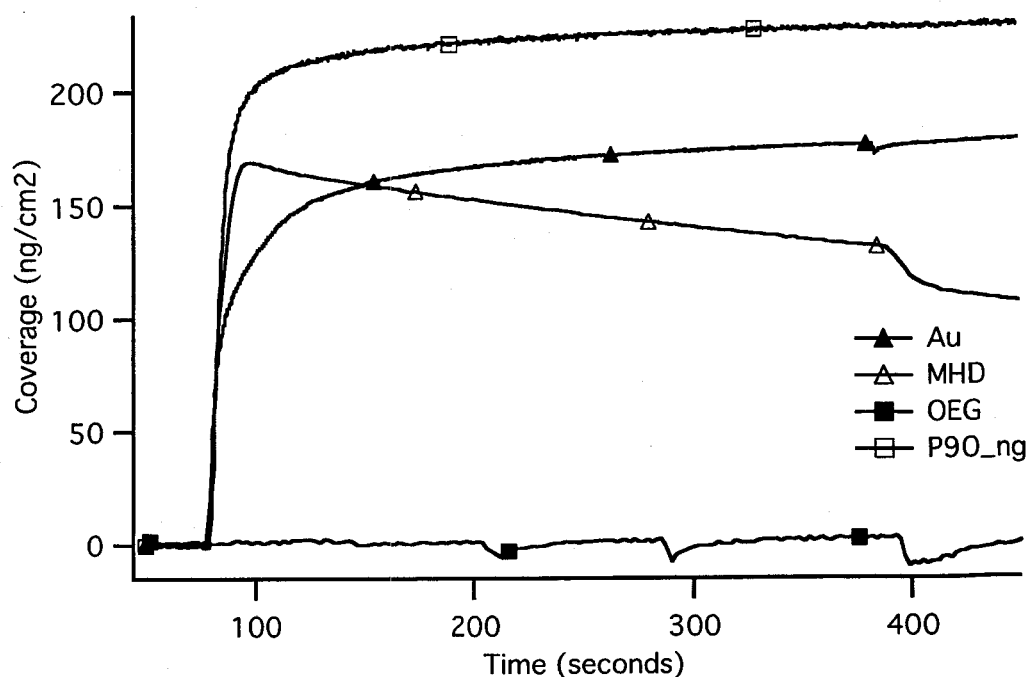


**Figure 4-6: Comparison of streptavidin adsorption kinetics on different surfaces.**

Four different surfaces were exposed to a streptavidin solution: 1) bare gold, 2) a pure MHD SAM, and 3) an OEG SAM, and 4) a mixed BAT/OEG that contains  $\sim 0.3 \chi_{\text{BAT,Sur}}$ . The differences in the rate of adsorption are indicative of different adsorption mechanisms. Note the  $>25\%$  additional adsorption to the specifically modified surfaces compared to those that support non-specific adsorption of streptavidin (Au and MHD.)

The data shown in Figure 4-6 are three overlaid SPR measurements that follow the binding of streptavidin from solution onto three qualitatively different surfaces: clean gold, MHD SAM, and a mixed BAT/OEG SAM where the surface mole fraction ( $\chi_{\text{BAT,Sur}}$ ) of BAT is approximately equal to 0.15. The first thing to note is that all three surfaces bind streptavidin from solution, albeit with different kinetics. Since the ability of the OEG thiol to resist protein adsorption has already been demonstrated, initial evidence for the BAT thiol to bind streptavidin is encouraging. Definitive proof that the adsorption of

streptavidin to BAT/OEG SAMs will come a little later. But for a first, qualitative argument, notice distinctly different rates of adsorption and desorption after protein injection (desorption is only really evident in the MHD trace) after the initial, diffusion-limited adsorption. These different results can be understood based on the rate of adsorption and binding mechanism of the three surfaces. There are two principle factors to consider: 1) the differing binding mechanisms and 2) the number of available surface sites. First, whereas the binding to MHD and gold is non-specific and (almost certainly) caused by a high interfacial energy at the solution / surface interface, the binding to the BAT / OEG SAM is more likely to occur via the biotin functional groups presented by the adlayer. Binding of streptavidin non-specifically to a hydrophobic interface likely entails some denaturation of a percentage of the proteins at the interface. Compared with the diffusion-limited rate of binding between streptavidin and biotin in solution, the denaturation process is sure to take much longer, slowing the rate of adsorption. As for the number of available surface binding sites, both the MHD and Au surfaces should have a comparable number of surface binding sites, as they are continuous surfaces (i.e., have no special structure of limited area for binding the ligand), and therefore the density of binding sites need not be taken into account when comparing these two. As for the BAT / OEG SAM, based on the film thickness measurement calculations (see chapter 3) which gives estimated density of adsorbed thiolates is  $4.0 \times 10^{14}$  molecules/cm<sup>2</sup> for OEG and  $2.7 \times 10^{14}$  molecules/cm<sup>2</sup>, assuming that the distribution of the BAT thiolates is generally homogeneous (over a length scale which is approximately the same as the

protein footprint, which is  $225 \text{ \AA}^2$ ), we would expect  $2.7 \times .15 = 4.05 \times 10^{13}$  molecules/cm<sup>2</sup> which is approximately  $250 \text{ \AA}^2$  / BAT or 1 BAT per SA footprint. This means that the number of surface sites is at least comparable to the other two surfaces, if not slightly lower. Since a lower binding site density would result in an even slower adsorption kinetics than a comparable, continuous surface, the rapid adsorption of SA to the BAT/OEG SAMs argues for a much faster binding mechanism than protein denaturing. The most likely candidate is via surface biotin functionality. Weak non-specific interactions with the BAT thiol are extremely unlikely, as flushing the flow cell with buffer does not remove any protein (not shown on this graph.) With this encouraging initial result, further experiments were undertaken to determine how the amount of biotin on the surface affected how much protein would bind. As already mentioned, definitive evidence that binding is biotin-mediated will be presented shortly.

#### **Correlating the surface density of BAT with maximal streptavidin binding**

A series of SPR measurements were carried out to quantitate the amount of protein that bound to BCMs containing varying surface mole fractions of BAT. These experiments were from a 0.05 mg/ml solution of streptavidin



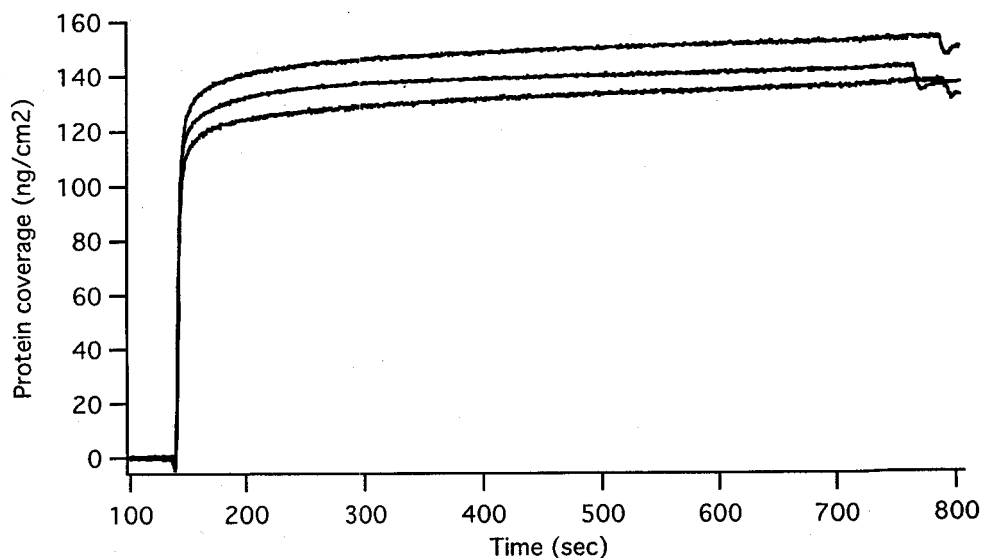


**Figure 4-7: SPR measurement of streptavidin adsorption to pure BAT SAMs**

This series of experiments illustrates the consistency of binding to BCMs (in this case, 100% BAT), as well as how the “maximum” amount of protein adsorbed to monolayers is determined.

This set of three experiments, charted on the same axis for comparison, illustrates how the streptavidin binding kinetics are distinctly different than those in Figure 4-4. In particular, binding is spontaneous, rapid, and stable (the protein does not spontaneously dissociate as observed in Figure 4-4; however, a small amount of protein--usually less than 2%--is removed when the protein solution is flushed from the flow cell with buffer.) These three traces are shown to illustrate the reproducibility of these type of experiments and to explain how the maximum adsorption was defined.

#### **Determining the maximum protein coverage from SPR data**

As is clear from inspection of Figure 4-7, the SPR minimum wavelength (and thus the amount of protein adsorbed to the surface) continues to slowly increase, though with

diminishing rate, long after the rapid initial adsorption. The question then becomes when to stop the experiment and measure the “maximum” protein coverage? And what about the amount that sometimes “rinses off” after flushing the flow cell? On account of limitations in the stability of the SPR baseline over long time periods (mainly as a result of temperature variations and lamp wavelength stability) an arbitrary yet reasonable decision was made to define the maximum amount of protein bound as the amount of protein that remained following a 1.5 mL rinse (flushing an ~80uL flow cell) initiated ten minutes after the protein injection. Selection of the 10 minute time period is justifiable both in terms of consistency and inter-experimental comparison as all the experiments were conducted similarly, but also in an absolute sense because in comparison with protein adsorption experiments that occurred over very long time periods (several hours), it was determined that ~95% of adsorption had taken place after the initial 10 minutes, so a shorter run time that reached near maximum would provide useful data for comparison as well as allowing more runs to be carried out in a single day. See Figure 4-8 for a typical example of the few long-term binding experiments that were carried out.

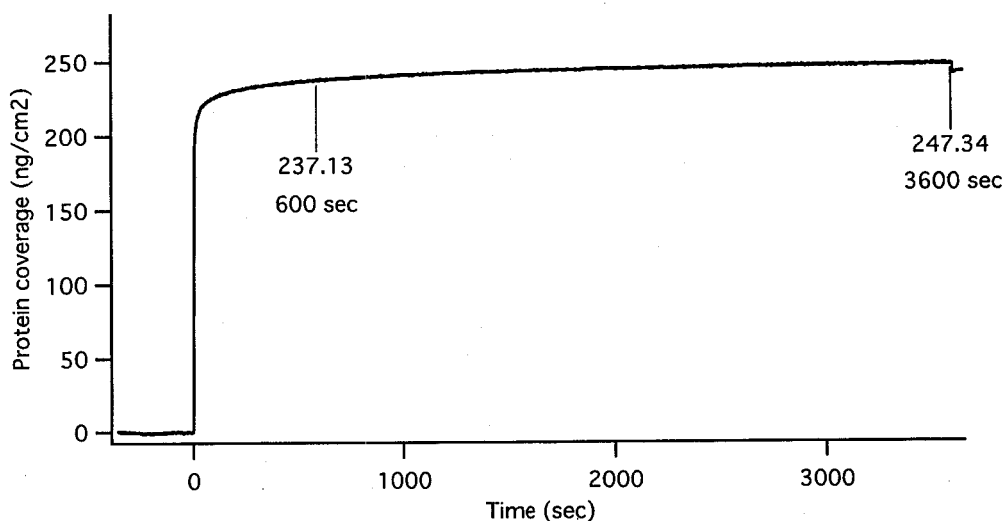


**Figure 4-8: Extended duration SPR adsorption experiment**

Data is shown to illustrate that ~10 minutes following the initial 0.05 mg/ml protein injection, the protein coverage had reached > 95% of the value reached after an additional 50 minutes. Result is typical of several long-term experiments.

Protein adsorption measurements were then carried out using surfaces functionalized with mixtures of BAT /OEG and BAT/MHD adlayers. The proportion of BAT in the mixtures covered the entire range from 0 to 100%. Results of these measurements are summarized in Figure 4-9. Also shown in Figure 4-9 is the outcome of the ARXPS N/C experiments undertaken using the BAT/OEG surfaces (refer, if necessary, to Figure 3-18, page 69). The relevance of the ARXPS N/C ratio to the SPR binding data will be discussed shortly.

For the moment, the focus will be on the range of surface BAT concentrations that support near maximal protein binding. The data show that maximal SA coverage occurs over a wide range of  $\chi_{\text{BAT,Sur}}$ . Interestingly, same maximal SA density occurs whether the

diluent thiolate is OEG or MHD (except at  $\chi_{\text{BAT,Sur}} < 0.05$ ), suggesting that at observed maximum coverage (averaging  $\sim 220 \text{ ng/cm}^2$ ) is a near-monolayer of protein.

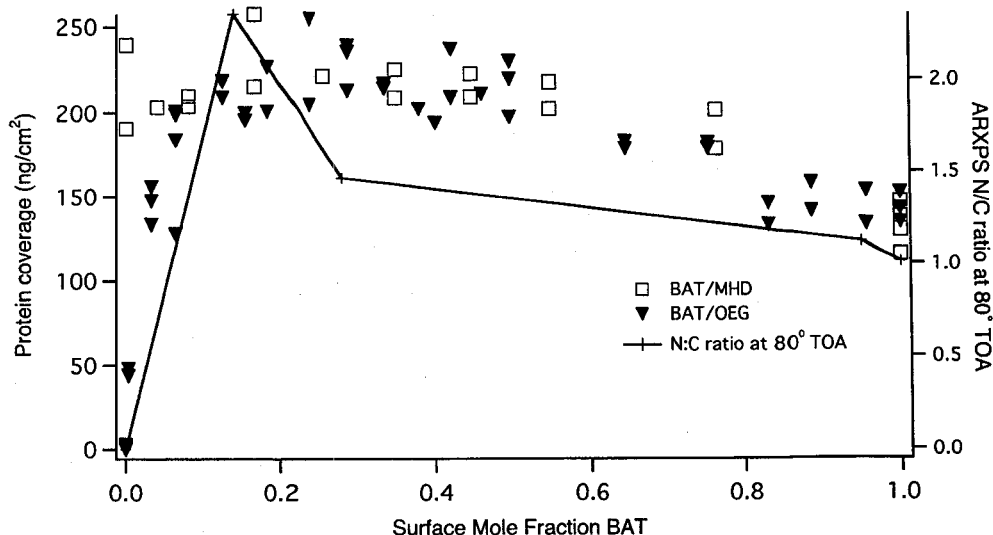


**Figure 4-9: Maximum streptavidin adsorption to mixed composition BAT SAMs**

Streptavidin adsorption was followed *in-situ* by SPR and the maximum binding density determined using the instrument calibration as determined by Jung et al (Jung, Campbell et al. 1998). The ARXPS N/C ratio for representative surface compositions of BAT / OEG SAMs (and hence the relative surface biotin density) is shown for comparison (solid line connecting (+))

Indeed, the average SA footprint at this surface density (i.e., the average area occupied per protein molecule) is  $(220 \text{ ng/cm}^2) * (10^{-9} \text{ gm/ng}) * (1 \text{ mole}/5.28 \text{ kDa}/\text{SA}) * (6.02 \times 10^{23} \text{ SA/mole}) = 2.5 \times 10^{12} \text{ molecules/cm}^2 = \sim 4000 \text{ \AA}^2/\text{molecule}$ . This is roughly 1.3x greater than the measured unit cell area observed for SA 2-D crystals formed under LB films at the air/water interface, which is quite reasonable for stochastic irreversible adsorption to a solid interface in solution.

An interesting result is obtained if the number of molecules per  $\text{cm}^2$  of both BAT and SA are compared to the maximum SA coverage as a function of surface composition. This ratio is obtained from the SA coverage quantitated by SPR and from the SAM thickness model (refer, if necessary, to Figure 3-32), which determined that the maximum density of BAT is  $4.0 \times 10^{14}$  molecules/ $\text{cm}^2$ . Assuming that the number of molecules of BAT varies continuously from zero to maximum as the surface mole fraction of BAT ranges from 0 to 1, the ratio of molecules per unit area as a function of surface composition can be determined.

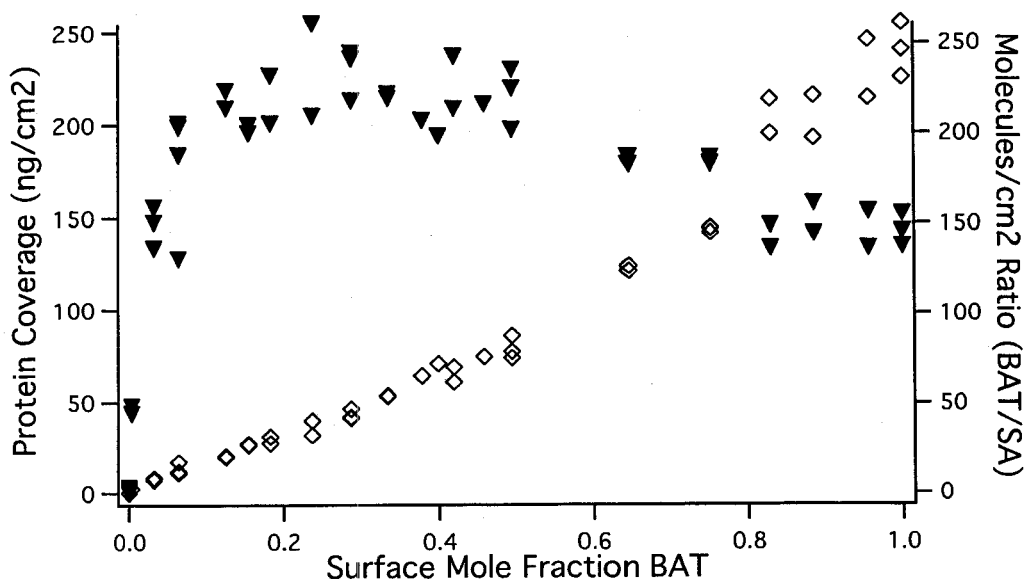


**Figure 4-10: Comparison of maximum SA coverage to BAT/SA area ratio.**

The left axis (triangles) shows the maximum SA coverage as a function of the surface composition and the right axis (diamonds) shows the ratio of BAT molecules to SA molecules per unit area.

Several things to note about this plot:

- 1) The initial BAT/SA ratio increases from 2 to 30 as  $0.0 < \chi_{\text{BAT}} < 0.15$ .
- 2) the increase in maximum binding at low surface coverages ( $0.0 < \chi_{\text{BAT}} < 0.1$ ) is associated with an increase of the BAT/SA MMA ratio with an average (initial) slope of 160.
- 3) The decline in maximum SA coverage begins at a BAT / SA ratio of  $\sim 80$
- 4) The slope of BAT/SA ratio increases at this point
- 5) The BAT/SA ratio reaches a maximum value of  $\sim 250$ .

These results are interesting for a number of reasons. First, the initial ratio suggests that there must be more than one BAT molecule per SA, in fact closer to 15, to support near maximal SA binding (on the order of  $200 \text{ ng/cm}^2$ ). Maximum SA coverage occurs at a BAT/SA MMA ratio range of between 20 to 80 (as  $0.15 < \chi_{\text{BAT}} < 0.5$ ), and it is at the low end of this range that we noted the minimum off-rate in the W120A desorption experiments. Once the BAT/SA MMA ratio increases to  $>100$ , the maximum amount of SA bound begins to decline, suggesting that despite an increasing BAT/SA ratio, the number of available binding sites on the surface is decreasing, most likely due to steric constraints. At a ratio of  $\sim 200$ , the maximal SA coverages levels off (near  $150 \text{ ng/cm}^2$ ), whereas the slope of the BAT/SA ratio increases to a final maximum of  $\sim 250$  BAT molecules / SA. In other words, Even though the MMA of streptavidin does not change in this range, the BAT/SA ratio continues to increase. One explanation for this observation is that despite the increase in the BAT/SA ratio, the availability of BAT for

SA binding remains roughly the same. This possibility is supported by the ARXPS data that shows decreased angular dependence of the composition profile at high BAT densities, implying a lowering of the number of biotin molecules on the surface available for binding despite the BAT surface density increase. A similar effect may well be occurring at lower BAT/SA ratios, such as around 100, where the initial decline in maximal SA coverage is first observed. Since the maximum amount of SA binding to the mixed SAMs goes down, the number of available surface sites must be declining. This could be the result of steric constraints against SA binding caused by high local densities of BAT, or it could be the result of high local densities of BAT creating a microenvironment that is akin to a 100%BAT surface coverage and therefore local surface architecture with lower surface biotin density.

Taken together, the wide range of  $\chi_{\text{BAT}}$  that supports maximal SA binding, the increasing ratio of MMAs at maximal binding, the decrease then plateau of maximal SA binding at very high BAT / SA ratios, and the geometry of streptavidin binding sites suggests that the protein could be bound to the surface in different modes at different  $\chi_{\text{BAT}}$ . This possibility was explored in detail, leading to a model of the different SA/surface binding modes that accurately describe the dissociation kinetics. The results of this analysis are presented in detail in the next section.

### ***Demonstrating Specificity, Affinity, and Avidity of SA binding***

In order to measure the stability of the bound streptavidin, experiments were designed to determine how fast the protein would dissociate from the surface following removal of the protein solution from the flow cells. Not surprisingly, wild-type streptavidin, with its extremely high affinity, did not measurably dissociate over the timeframe of practical experiments. Therefore, site-specifically mutated SA variants with much faster off-rates were used. These mutants, created by the Stayton lab, have been described extensively in the available literature (Klumb, Chu et al. 1998). One of the more useful variants was W120A (indicating that the tryptophan residue at position 120 in all the four monomers had been substituted by alanine.). This mutant would bind to the BCM similarly to wild-type (though to a somewhat lower maximum coverage) and would also *dissociate* from the adlayer if the protein solution in the flow cell was exchanged with buffer. Furthermore, the protein could be competitively dissociated from the surface by exchanging the protein solution with a buffer containing an excess concentration of soluble biotin (2mM, about the solubility limit of biotin in aqueous solutions.) Figure 4-11 compares the results of these two dissociation conditions.

The results shown for binding and dissociation of W120A under plain buffer (i.e., not containing soluble biotin) clearly demonstrate that this mutant protein will come off the surface rapidly. In addition, the fact that only some of it comes off readily suggests two different “populations” of bound protein. The protein population that does not spontaneously dissociate upon addition of plain buffer must be bound more tightly to the



surface than the population that does desorb. This suggests two different surface binding modes available to the protein.

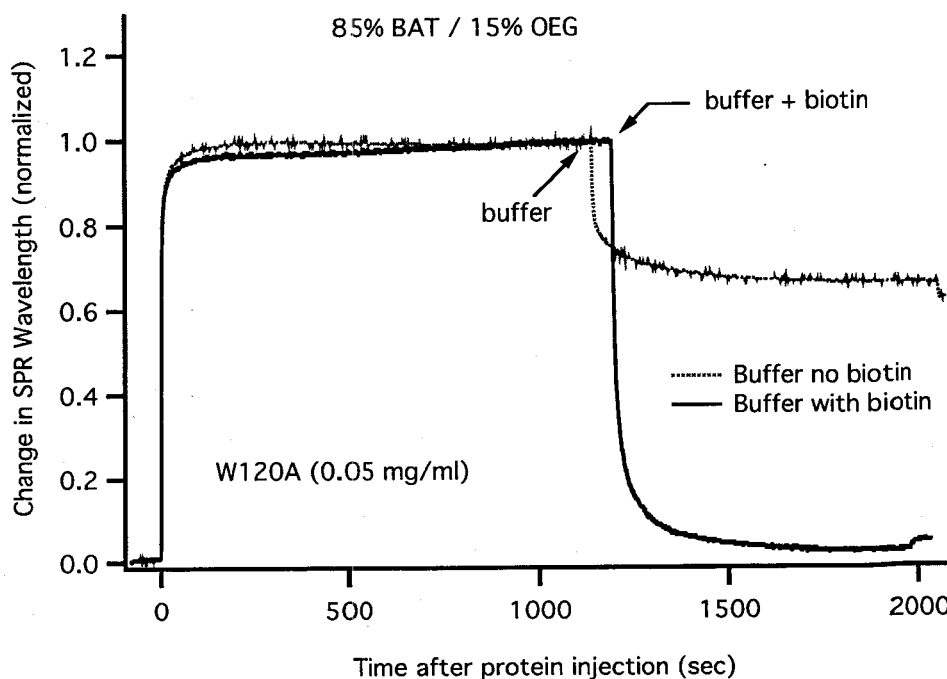


**Figure 4-11: Streptavidin mutant W120A is useful for investigating binding avidity**

W120A will spontaneously dissociate from mixed BAT / OEG SAMs following replacement of the protein binding solution with buffer only (red trace), or can be competitively dissociated from the surface with buffer containing biotin. The kinetics of dissociation in the presence or absence of a soluble biotin competitor can be used to investigate the nature of the streptavidin / surface bond(s).

Incidentally, though most importantly, demonstration that the fraction that remains bound after buffer addition can be completely dissociated by addition of soluble biotin provides clear evidence that streptavidin is indeed bound to the surface via biotin.

Aside from that, we were interested in whether the different binding modes could be caused by the density of BAT on the surface. Therefore, a series of experiments were

carried out to probe how the streptavidin was binding to the surface, and whether the surfaces could be optimized for maximum protein binding stability (in other words, finding the surface BAT density that was associated with the slowest SA off-rate.)

### Measuring streptavidin binding mutant dissociation rate as a function of thiolate monolayer composition

Figure 4-12 illustrates representative results from these experiments. The first thing to notice is that the dissociation kinetics compared across a range of surface BAT densities are dramatically different.

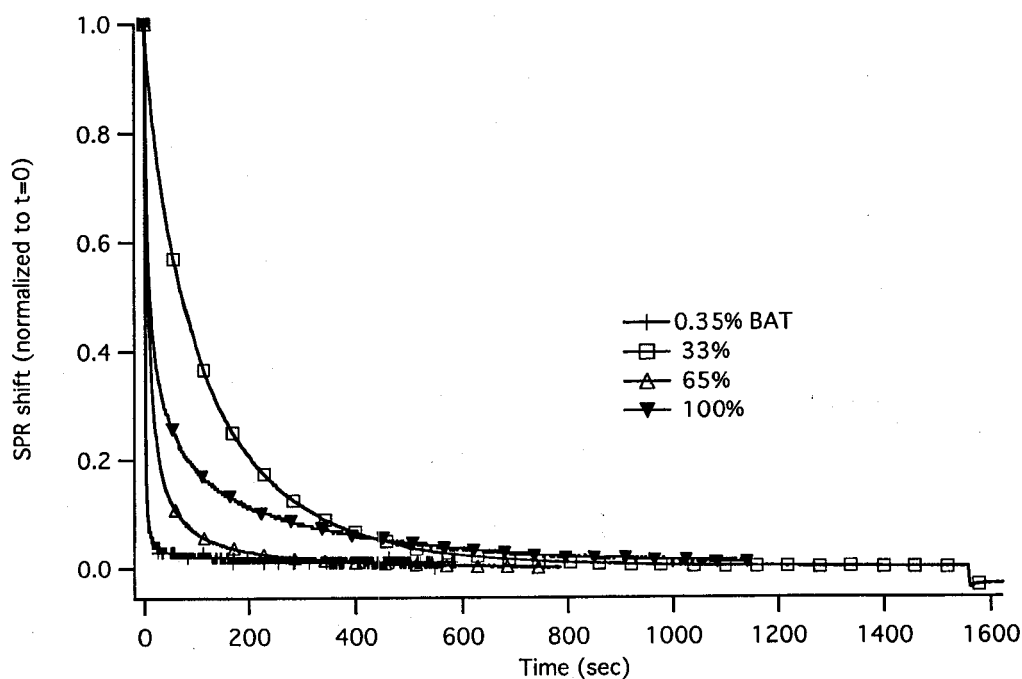


**Figure 4-12: W120A dissociation curves for three different BAT / OEG SAM compositions**

Selected dissociation curves illustrating how the off-rate changes with surface composition. The initial protein coverage differed by surface composition as expected; the dissociation curves were normalized to the maximum amount of protein bound (1)

and the minimum amount remaining (0) to ensure comparable results from the kinetic analysis.

Note, in particular, the dramatically decreased desorption rate exhibited by the 33% BAT composition compared to both the 0.35% and 65% surface. These and other dissociation curves and off-rate mutants (Figure 4-13) were used to probe the nature and strength of protein/surface associations. Differences in the rate constants in what appear to be a double-exponential decay from surfaces with differing BAT densities guided the development of a mechanistic picture of the types and quantities of interactions between adsorbed streptavidin and the functionalized surface.

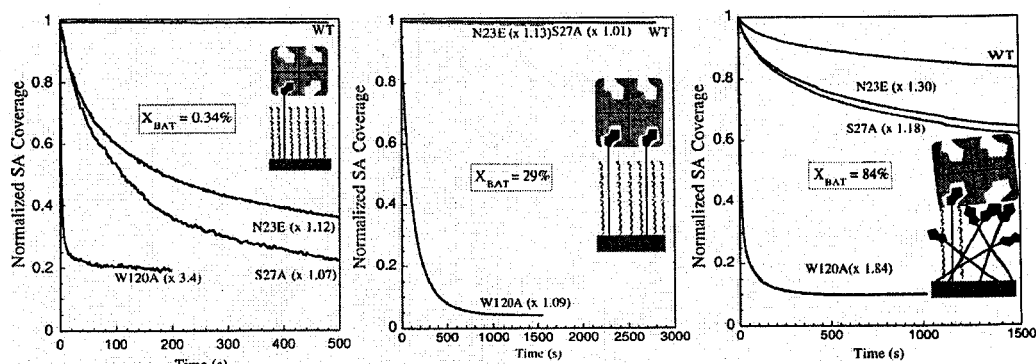


**Figure 4-13: W120A dissociation curves obtained from a representative range of mixed BAT / OEG SAMs using three different SA binding mutants and wild-type.**

The left panel shows the normalized desorption curves at the lowest concentration of BAT in the surfaces studied. W120A, N23E, S27A, and WTSA are shown; note how the desorption rate is dependent on the binding mutant's solution off-rate. The middle panel shows just WTSA and W120A (the other two mutants are not shown for clarity.) The final figure shows the data collected from all four isotypes. Note here that the desorption rate for W120A has increased and that WTSA displays a relatively rapid off-rate, suggesting much weaker association to the surface.

Dissociation kinetics were measured with three streptavidin binding mutants (W120A, S27A, N23E) and core recombinant streptavidin (WTSA). Noting that the

desorption rates were the slowest at intermediate  $\chi_{\text{BAT}}$ , and that the rates again increased at higher BAT densities, and also noting that the protein has two binding sites on the side of the molecule facing the biotins, the following mechanistic model for explaining the data was proposed. The development of this model is explained briefly in the following section (see (Jung, Nelson et al. 2000) for full details.)

First of all, two rate constants suggest two different populations of SA that are bound differently to the surface. The most obvious explanation is that the one population is bound via one biotin, the other is bound via two (see Figure 4-14.)

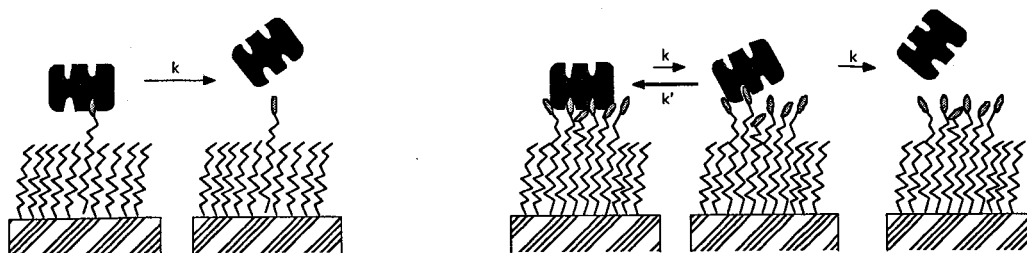


**Figure 4-14: Depiction of streptavidin binding modes**

The example on the left proposes the dissociation mechanism for a SA bound via one biotin, in which the singly-bound protein simply dissociates from the surface irreversibly (the binding pocket is assumed to be rapidly filled by the excess soluble biotin). The second example (right) shows a SA protein bound to a region on the surface with a local high density of BAT. Here we propose that the protein dissociate from one binding pocket at a time with the same rate constant as the single-dissociation shown on the left, but in this case the protein can re-bind to the surface before fully dissociating. The rebinding rate constant is much faster than the dissociation rate due to the proximity of surface biotins. Occasionally, the protein may completely dissociate before rebinding; we assume the same single-dissociation rate applies here also.

Following the derivation published by Jung et al. (Jung, Nelson et al. 2000), this model of dissociation leads to the following formula:

$$\theta(t) = \theta_{-SB}^{\circ} \exp(-kt) + \theta_{BSB}^{\circ} (1 + K) \exp(-kKt) + \theta_{irrev} \quad (\text{eq. 7})$$

This dissociation model describes the two populations of SA, the first singly bound ( $\theta_{SB}$  for “SA-biotin”) the second doubly bound ( $\theta_{BSB}$ ). The constant  $K$  equals  $(k/(k+k'))$ . Notice that the dissociation model based on our mechanistic assumptions closely resembles a double-exponential function with two fixed rate constants and initial population values. We found that the dissociation model accurately fit the data ( $\chi^2$  values typically ranged from 0.01 – 0.06, similar to a pure double-exponential function). Fitting the desorption data to this model yields the rate constants listed in Table 4-1. The values for the constants shown are averages of fits for a particular mutant from a very low BAT density surface ( $k_{SB}$ ) and the intermediate density surface with the slowest off-rate ( $k_{BSB}$ ) since these two surfaces represented those whose SA populations were dominated by singly bound and doubly bound proteins, respectively. Observe that the dissociation rate constants for the doubly-bound population of SA is the square of the singly-bound rate constant for all except wild-type. This is strong evidence of the mechanism proposed whereby this population of protein must undergo two identical yet independent dissociation steps before the protein leaves the surface.

**Table 4-1: Rate constants determined by fitting data to Equation 7.**

Listed are the average values found for  $k$  and  $k'$  for each different SA variant by analysis of off-rate curves at 0.35% and 29% surface BAT, respectively, and the values for  $k_b$  found for these values found by extension (see (Jung, Nelson et al. 2000)). Listed for comparison are the rate constants determined in homogeneous solution (Jung, Nelson et al. 2000). The large variations in the reverse rate constant by variant are artifacts of the fitting algorithm that poorly determines the fast rate if very much greater than the slow step.

SA variant	k (solution)	k (SB)	k (BSB)	k'
WT	$4.0 \times 10^{-6}$	$1.4 \times 10^{-5}$	$< 3 \times 10^{-6}$	$> 5 \times 10^{-5}$
S27A	$1.2 \times 10^{-3}$	$6.1 \times 10^{-3}$	$3.9 \times 10^{-6}$	9.6
N23E	$1.6 \times 10^{-3}$	$2.1 \times 10^{-3}$	$8.4 \times 10^{-6}$	0.52
W120A	(23*)	0.23	$8.2 \times 10^{-3}$	6.4

In summary, the fast off-rate mutants to measure the variations in dissociation kinetics from different composition BCMs enabled us to develop a physically realistic mechanism of SA binding at the different BAT densities that fits neatly together with the film thickness data, the maximal SA adsorption data, and the ARXPS data. This picture has enabled us to determine the optimal surface BAT density for maximizing the stability of the bound streptavidin, an important consideration when using a system that does not covalently (i.e., irreversibly) link the ligands to the surface.

### ***Protein multilayer assembly***

Now that the binding of the “adaptor” streptavidin layer has been demonstrated and extensively characterized, it is time to determine the conditions under which a protein multilayer can be formed, if it can at all.

### **Biotin-mediated protein multilayer assembly on BAT / OEG SAM**

Attempting to form a protein multilayer is as simple as following the SPR shift caused by injecting a biotinylated protein into the same setup used to first measure SA adsorption. Determining the specificity of protein binding is also quite straight-forward: inject proteins that have not been conjugated with the necessary linkers; namely, biotin. A classic example of just such an experiment is shown in Figure 4-15. This experiment

demonstrates both the requirements for the proper assembly sequence (Figure 1-3) and linkers (e.g., “bOp” or “biotinylated osteopontin”, instead of “Op” for non-biotin-conjugated osteopontin) and the concentration-dependent formation of a protein multilayer.

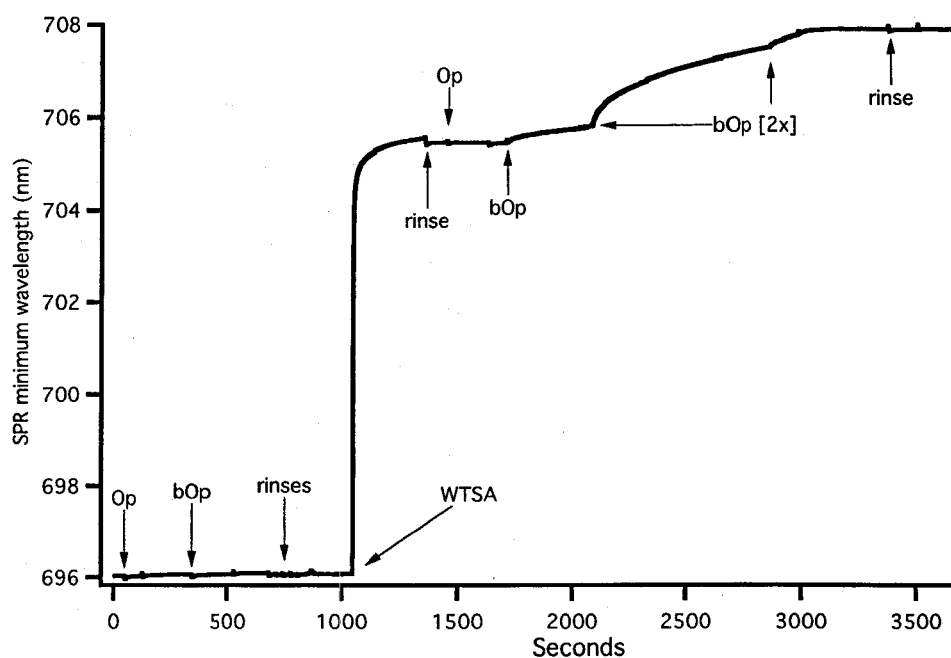


**Figure 4-15: Demonstrating conditions necessary for assembling engineered protein multilayers**

This SPR experiment demonstrates not only how protein multilayers can be formed, but also the conditions and sequence necessary for their formation. Here, a biotinylated osteopontin fragment (bOp) is bound to a streptavidin layer, forming an engineered protein multilayer. This fragment will not bind to the biotin SAM unless streptavidin is first adsorbed (first two injections), and the streptavidin layer does not support attachment of a non-biotinylated osteopontin fragment (Op). Concentration-dependent adsorption kinetics (bOp / bOp [2x]) and maximum osteopontin adsorption are also demonstrated in this experiment. Further details are given in the main text.

Only the correct sequence of appropriate adsorbates will support protein multilayer assembly. A mixed SAM containing ~ 30% BAT will not support adsorption of the 30N terminal fragment of osteopontin, whether conjugated to biotin or not (first two injections). However, exposure of this biotin-functionalized surface to streptavidin results in rapid protein adsorption (WTSA injection.) Multilayer formation only results when the secondary adsorbate is conjugated to biotin, enabling it to bind to the streptavidin coated surface (Op / bOp injections); the rate of binding of the secondary adsorbate is dependent on its solution concentration (bOp [2x]). The multilayer formed does not spontaneously dissociate when the protein solution is replaced with buffer (rinse).

To demonstrate that the streptavidin surface can bind different types of proteins (e.g., fibrillar vs. globular), a similar experiment was carried out using biotinylated collagen (Figure 4-16.) As in Figure 4-15, controls are included to show specificity of binding. The controls shown in Figure 4-16 include the requirement for biotinylation of collagen (i.e., no non-specific binding between collagen and the streptavidin surface) and whether osteopontin can bind to the collagen secondary layer. The fact that no osteopontin bound to the surface strongly suggests that this fragment has no affinity for collagen (unlike full-length osteopontin, Ceci Giachelli, personal communication), and that the time allowed for the biotinylated collagen to bind was sufficient to fully saturate the streptavidin binding sites (or at least block the 30N fragment's access to them.) Assuming that the streptavidin surface is fully saturated by the collagen secondary layer (an assumption supported by the very slow adsorption rate just prior to flushing the flow cell), and using



the method for quantitating the amount of protein bound (Jung, Campbell et al. 1998), the ratio of the number of collagen molecules to the number of streptavidin molecules can be determined. In the example shown in Figure 4-16, 3 collagen molecules bound for every 4 streptavidin.

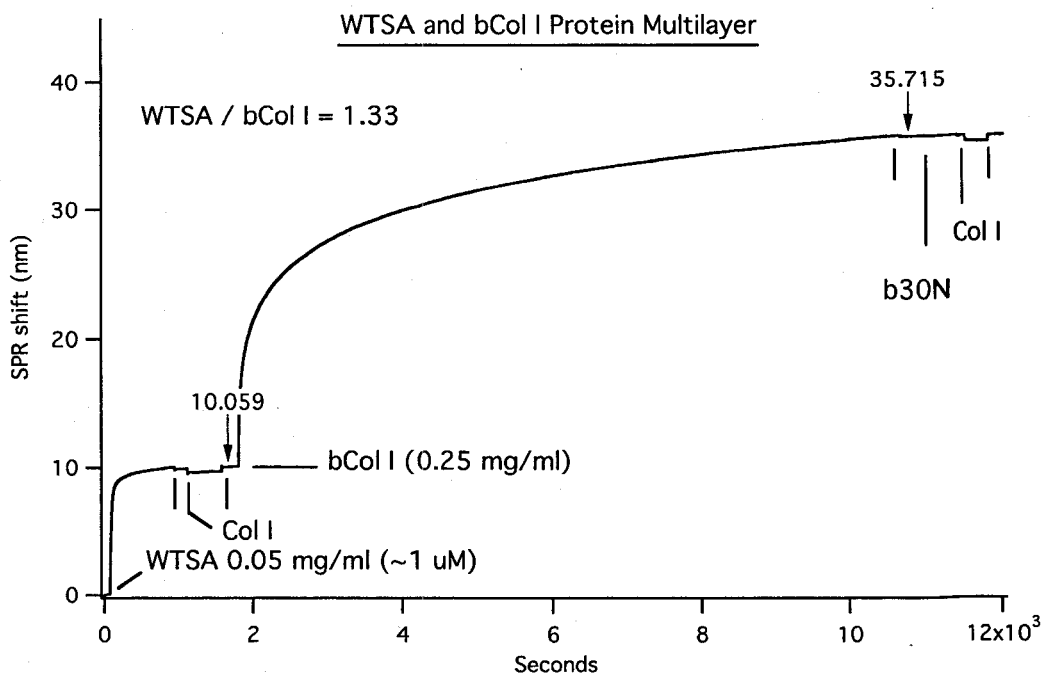


**Figure 4-16: Protein multilayers created using collagen as a secondary adsorbate**

In this experiment, SPR is used to monitor the assembly of streptavidin on a ~30% BAT / 70% OEG SAM, followed with the attachment biotinylated bovine collagen type I. As illustrated in the previous experiment, the secondary adsorbate must be biotinylated in order for binding to occur; note that “ColI” (non-biotinylated collagen) does not bind to the streptavidin layer, whereas “bColI” bound to a large extent.

This somewhat low ratio is not representative of similar experiments, though it is shown since it includes the control data to demonstrate the specificity of binding biotinylated ligands. The low ratio in this case could possibly be the result of collagen

self-assembly (fibril formation) which was occasionally observed in similar experimental regimes, where the concentration of collagen or the salt concentrations (pH, temperature, age of the solution) varied, causing the protein to gel. While not entirely common, it was noted often enough to support this explanation.

Noting that a saturation coverage of secondary adsorbates could be achieved by using a high concentration of secondary protein, these experiments were repeated and the average ratio of either collagen or 30N osteopontin to the amount of streptavidin bound was determined. Table 4-2 shows the average amount of collagen and osteopontin that would routinely bind to a specific amount of immobilized streptavidin.

**Table 4-2: Ratio of streptavidin density to secondary protein adsorbate for collagen I and 30N Osteopontin Fragment**

Multilayer Composition	binding ratio
WTSA / bColI	2.0
WTSA / b30N	1.0

The first entry shows that one collagen I molecule required two streptavidin molecules (on average) for adsorption. This result is consistent with the average area occupied by a single streptavidin molecule ( $\sim 3800 \text{ \AA}^2$ ) and the approximate molecular weight of a single collagen molecule ( $\sim 282\text{kDa}$ ). In contrast, the much smaller 30N osteopontin fragment ( $\sim 18\text{kDa}$ ) could be expected to fit well within the area occupied by

a surface-bound streptavidin, and indeed the experimental data indicates that each streptavidin, on average, binds one 30N molecule at saturation coverage.

Having determined that protein multilayers could be formed using one of two very different ligands, experiments were performed to demonstrate that a single streptavidin adlayer could bind more than one type of ligand (Figure 4-17.)

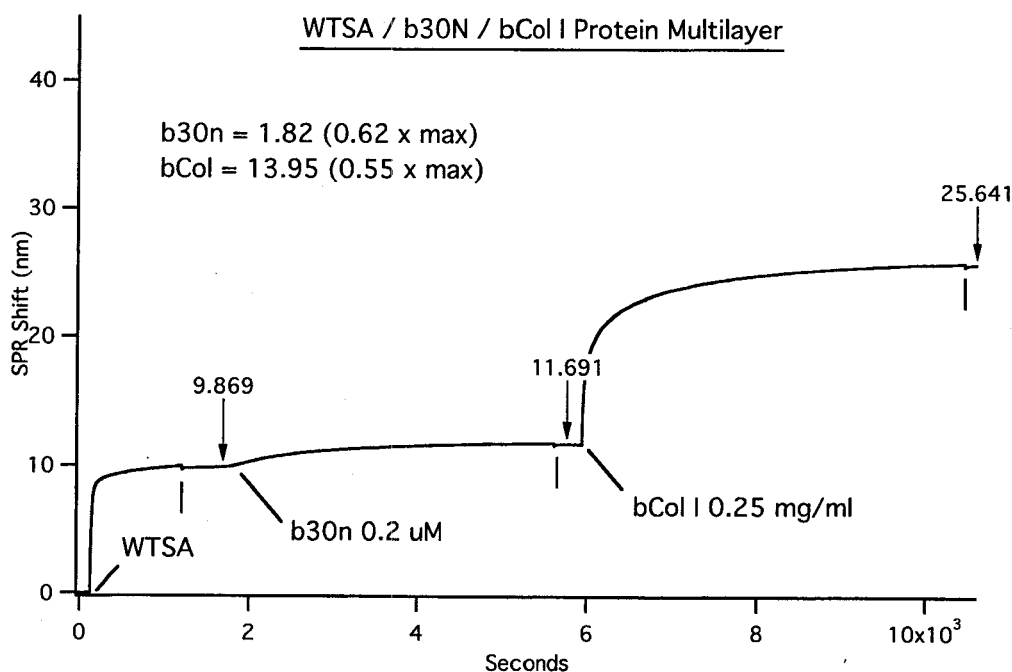


**Figure 4-17: Creating a protein multilayer with a mixture of secondary adsorbates**

In this experiment, both biotinylated osteopontin (b30n) and biotinylated collagen are bound to the streptavidin coating. The fraction of osteopontin coverage on the streptavidin layer was determined by comparison to previous experiments in which it was allowed to proceed to saturation (no further adsorption occurred over time.) For this experiment, adsorption of osteopontin proceeded at a relatively slow rate, controlled by decreasing the concentration of the protein in the flow cell. After a limited time, the surface was rinsed with buffer and subsequently exposed to a solution containing biotinylated bovine Collagen I (bCol I). Adsorption of Collagen proceeded essentially to completion, and the amount that bound was compared to maximum saturation amounts achieved in previous experiments.

The figure clearly shows that the sequential exposure of different biotinylated ligands will result in the formation of a “binary multilayer”, that is, one in which the secondary protein layer consists of two different proteins.

Interestingly, when the coverage of the two secondary adsorbates was compared to the saturation coverage when either one of the ligands were present (Table 4-2), it was found that if the second ligand to be immobilized on a binary multilayer was allowed to proceed to saturation, the sum of the ratios of secondary protein coverage to the coverage of the SA adlayer was close to 1; that is, that the number of streptavidin binding sites constrained the amount of protein that bound, and that as the SA sites filled up with the first adsorbate, the amount of the second adsorbate that would bind decreased (Table 4-3), and that the overall density of the proteins bound to the streptavidin support was controlled mainly by the relative size of the adsorbate to the area occupied by the underlying streptavidin density.

**Table 4-3: Fraction of maximum binding of secondary adsorbates in mixed protein multilayers**

	Fraction of maximum binding capacity	
	b30N	bColI
run 1	0.61	0.55
run 2	0.43	0.57
run 3	1.01	0.05

### *Chapter Summary and Conclusions*

The results presented in this chapter represent a significant addition to the overall picture of how mixed BCMs can support streptavidin binding, and how the composition and architecture of the surface affects the amount and stability of the adsorbed protein. In summary, we have shown that: OEG SAMs are resistant to non-specific protein adsorption and that MHD SAMs bind protein non-specifically (as expected), and that therefore the amount of non-specific protein adsorption depends on chemical nature and surface concentration of diluent thiolate. Perhaps most importantly, we have demonstrated that mixed BCMs specifically bind SA to reproducible levels, that surface nitrogen content (BAT concentration) correlates with SA binding capacity, that maximum binding is observed at sub-maximal BAT concentration, and that maximum SA coverage approaches the density of SA in a 2D SA crystal. This set of results demonstrates that by varying the proportion of thiolates in a mixed BCM, control over non-specific and selective protein binding has been achieved (Figure 3-1).

We have also shown that mutant desorption characteristics provided significant insight into specific and non-specific protein-BCM interaction, and we have developed a model for how the SA adlayer is bound to the surface. In this model, there are two populations of bound SA, and using this model we have determined that the proportions of the different populations change from mostly singly-bound to mostly doubly bound as the surface density of BAT increases from very low to that at which the maximum amount of SA coverage was achieved.

We have also shown that bound SA is available for subsequent immobilization of biotinylated molecules from solution, and that multilayer assembly requires appropriate (biotin) functionalization of surface and proteins, as well as proper assembly sequence. This confirmed the specificity of binding and mechanism of multilayer assembly outlined in Figure 1-3.) We noted, importantly, that this method of secondary protein immobilization was quantitatively determined by the number of SA binding sites, further demonstrating the robustness and predictability of the system.

Finally, we note that multilayers can be assembled using a mixture of secondary adsorbates, providing a tool for exploring cell culture substrates of controlled yet complex composition.

Having provided broad and detailed evidence of the protein binding capabilities of this method for surface engineering, we now move on to whether or not the immobilized proteins will support specific cell response.

## 5. Cell Response to Immobilized Proteins

The work presented so far has laid the foundation, literally and figuratively, for using BCMs to engineer surfaces that can be used as an experimental system for studying how cells respond to surface-immobilized proteins. Having established that 1) the alkylthiolate adlayers will control the chemistry and protein binding characteristics of the surface, 2) that the engineered surfaces rapidly, reproducibly and specifically bind streptavidin from solution, and 3) that the streptavidin layer can bind specifically and quantitatively bind proteins from solution, we are prepared to test the engineered surfaces as cell culture substrates.

Cell culture is a broad discipline, to say the least. Cell behavior in culture is nearly as varied as there are types of cells. Therefore, a reasonable and meaningful test of these surfaces' suitability for use as a cell culture substrate needed to be sharply defined. We did not expect that these surfaces would be suitable for every experimental situation, for a number of reasons. Foremost among them was that they were principally designed to provide a system that enabled the researcher to control and quantitate the proteins that the cells interacted with when they came into contact with the surface. There are inherent biological limitations to implementing systems such as these, since cells in culture are known to actively remodel their environment by secreting both proteases and matrix

proteins. Therefore, the ability to control the proteins cells encounter on the surface would be limited to a time frame that is shorter than the time it takes for cells to remodel their environment. This could be as short as several hours (if not beginning almost immediately for cells such as fibroblasts.) This does not preclude the utility of the surfaces described in this research for longer-term experiments, though they would have to be carried out with cell's ability to restructure their environment in mind.

Along these lines, initial characterizations of these surfaces was chosen to be limited to experiments that could be carried out over a short term and therefore establish that the substrates provided control over the quantity and composition of cell receptor ligands and thereby elicit a controlled cell response. Short-term cell adhesion experiments were chosen to fit these requirements.

The experiments described in this chapter were designed to answer the following questions:

1. Did the engineered surfaces themselves promote non-specific cell attachment?
2. Would adhesion ligands that are specifically immobilized on these surfaces support cell adhesion?
3. If so, was cell adhesion to the surfaces specific (i.e., integrin-dependent and RGD mediated)?
4. Would different adhesion ligands support cell adhesion in a manner consistent with the cell type?



5. Could the streptavidin support be engineered to contain an RGD tripeptide that will itself support cell attachment?

Let us begin with the first aim, to determine whether the engineered surfaces only support cell adhesion when functionalized with specific adhesive ligands.

#### **Adhesion ligands used for this series of experiments**

Several different adhesive ligands were chosen for these experiments based on the outcomes of previous experiments and the availability of a fairly well-defined set of cell lines that differ in their response to osteopontin; this differential response was determined to be correlated with the cell lines' integrin receptor expression patterns (i.e., the amounts and types of the different integrin  $\alpha$  and  $\beta$  subunits, see Table 5-1 and further details below.) The biologically active and specific ligands chosen were:

1. b30N – the “30N” terminal fragment of osteopontin containing the RGD integrin binding tripeptide, recombinantly expressed and subsequently conjugated with biotin (hence the “b” designator of “b30N”—“30N” is just the recombinant fragment not conjugated to biotin),
2. bCol I – acid hydrolyzed and purified bovine soluble collagen type I, conjugated to biotin (as above, “Col I” is the precursor collagen not conjugated to biotin),
3. Engineered SA variants expressing RGD cell adhesion motif on a surface loop (two variant RGD sequences were engineered into SA, one with flanking

residues homologous to the fibronectin type III domain (“FNSA”), and one with flanking residues homologous to osteopontin (“OPSA”).)

### Cells used for adhesion experiments

As mentioned above, we had a set of cell lines that had been used in previous, related experiments that provided a good fit to the recombinant and otherwise readily available surface ligands. The adhesion-dependent cells used in these experiments are of four types:

1. an M21-derived human cell line of two strains (Table 5-1):
  - a. “Mo” which expresses a wide range of integrin receptors, though the  $\alpha_v\beta_3$  integrin is not expressed at very high levels,
  - b. “Mo $\alpha_v$ ”, similar to the Mo cell line, though the  $\alpha_v\beta_3$  receptor is expressed at higher levels (note that other, poorly or uncharacterized intracellular differences may exist as well)
2. “IC4” human smooth muscle cells derived from a neointimal carotid arterial biopsy
3. “HNBE6E7” (aka HNB) human newborn smooth muscle cells “immortalized” by stable transfection with a transforming viral gene set.

These cells were used because they were relatively easy to grow and were known to bind both osteopontin and collagen, and were potentially interesting for use in further experiments that characterize their interactions with these immobilized ligands. For the purposes of this discussion, the focus will be mainly on the M21 derived cells. Since we

were immobilizing integrin receptor ligands, we report here the integrin receptor expression patterns of the M21 derived cell subsets here in Table 5-1 (IC4 SMC integrin receptor expression was not characterized.)

**Table 5-1: Integrin receptor expression patterns for Mo, Mo $\alpha_v$ , and HNB18E6E7 cell lines (from (Hu, Hoyer et al. 1995; Smith, Cheung et al. 1996; Smith and Giachelli 1998)**

Antibody	Peak fluorescence		
	Mo	Mo $\alpha_v$	HNB18E6E7
$\alpha_1$	1.90	1.65	2.5
$\alpha_2$	4.14	9.12	33
$\alpha_3$	3.10	7.74	12
$\alpha_4$	1.62	2.64	2.5
$\alpha_5$	1.26	1.30	14
$\alpha_6$	1.83	1.72	1
$\alpha_9$	7.02	7.24	1
$\beta_1$	12.14	24.27	65
$\beta_6$	1.02	0.98	n/d
$\beta_3$	1.21	36.49	n/d
$\alpha_v$	1.17	64.60	17
$\alpha_v\beta_3$	1.07	26.35	4
$\alpha_v\beta_5$	1.07	3.88	9

Note the dramatically increased levels of the  $\beta_1$ ,  $\beta_3$ , and  $\alpha_v$  subunits displayed by the Mo $\alpha_v$  subset, and in particular the >25-fold higher levels of  $\alpha_v\beta_3$  subunit expression. This integrin has been associated with wound healing and angiogenesis (among other important functions) and binds to osteopontin; this makes it an interesting subject for future study. Note also that whereas the Mo $\alpha_v$  cell line does express more of the  $\alpha_1$ ,  $\alpha_2$ , and  $\beta_1$  subunits, the Mo cell subset consistently demonstrated a stronger adhesion to collagen than did the Mo $\alpha_v$  cell subset. The reason for this observation was not well

characterized; potentially there are more  $\alpha_2\beta_1$  integrin subunits associated in the Mo cells than the Mo $\alpha_v$ , though this was not characterized. There could be other—also uncharacterized—intracellular differences as well.

Using these cells and the ligands mentioned earlier, experiments were undertaken to determine whether the engineered cell culture substrates would support specific cell adhesion. These results are shown in the next several sections.

### ***Cell adhesion results***

#### **Cell adhesion controls and comparison to ligands on polystyrene**

This first data set shows the results of a series of control experiments designed to determine the specificity of cell adhesion to the various layers of the engineered surfaces. Briefly, all the wells were coated with BAT/OEG SAMs ( $\chi_{\text{BAT,Sur}} \sim 0.15$ ), then treated with different components of the engineered surfaces (or related binding controls.) Figure 5-1 shows that the surfaces, when properly prepared, promote strong cell adhesion.

The details of the results shown in the different bars in Figure 5-1 are described here as follows (from left to right): 1) “no cells” – wells were functionalized with a mixed 15% BAT / 85% OEG SAM (as all were) and treated with mock protein solutions (buffer only). This set of wells was used to determine the amount of background signal due to non-specific binding of dye to the well and surface.

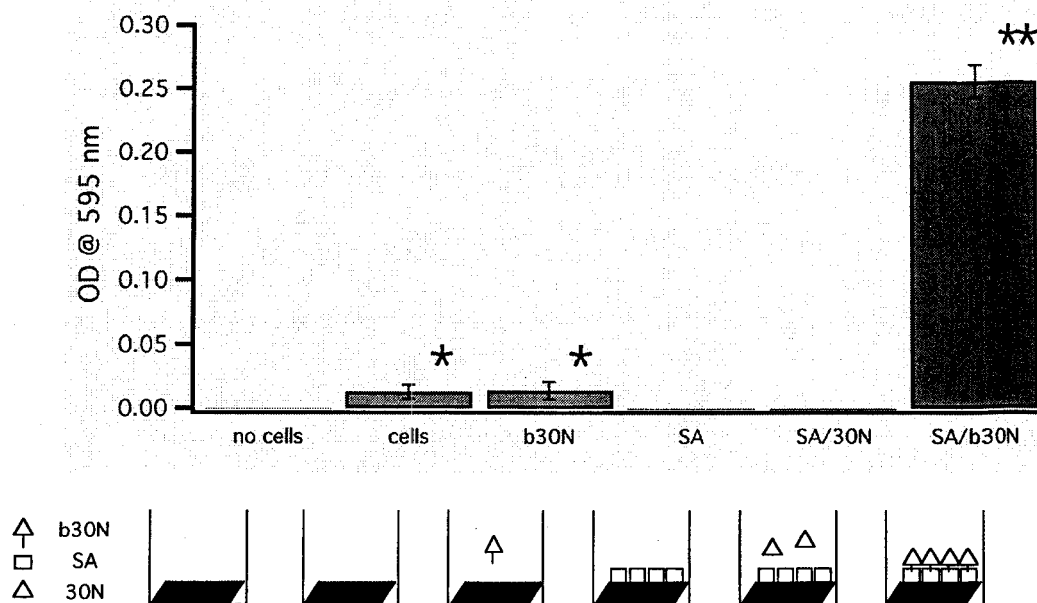


**Figure 5-1: Cell adhesion to protein multilayers requires proper assembly sequence and ligand functionalization**

Bars represent relative amount of cell adhesion in terms of optical density of assay (see Methods section for experimental details). Illustrations below the axis labels depict the elements of the engineered multilayers used for assembly. Each of the tests were run in triplicate wells on the same plate, using cells collected from the same time (several flasks were combined and mixed before using for seeding surfaces.) Single asterisks denote significant difference from “no cells” control (student’s t-test,  $p < 0.05$ ), double asterisk denotes significance with  $p < 0.01$ .

All other results were normalized to the background determined by this control. 2)

“cells” – wells functionalized with mixed BAT / OEG SAM but no proteins (SA or 30N) were added. This set was used to determine how much the BCMs themselves promoted non-specific cell adhesion, 3) “b30N” – the biotinylated osteopontin fragment was added to wells that had not been treated with streptavidin. Lacking this key adaptor between the BCM and potential ligands, it is expected that no 30N would remain after rinsing out the protein solution. The result of this experiment is essentially identical to the ‘cells only’

control since no adhesive proteins should be present, 4) “SA” – this BCM had been coated with wild-type SA but no adhesive ligand. This experiment was included to control for SA adlayer-induced cell attachment, 5) “SA/30N” – this surface was treated with SA and a *non*-biotinylated 30N fragment. Based on prior SPR experiments, no 30N ligand is expected to bind to the SA-treated surface (see Figure 4-15.) However, there was a slim chance that trace amounts of protein might remain that may promote cell attachment. Consistent with the SPR results, there was no difference in the results of this experiment compared to the “SA” control, 5) when the engineered surfaces are assembled using the appropriate components in the proper sequence (BCM, SA, biotinylated ligand), the result was significant cell adhesion.

These results demonstrated two important properties of these monolayers: 1) that “bare” (i.e., before coating with streptavidin) BCMs did support a small amount of Moav cell attachment, but 2) that this attachment was abrogated by streptavidin-functionalized BCMs, and 3) that a specifically immobilized RGD-containing 30N ligand strongly promoted cell adhesion.

Further demonstration that the immobilized 30N was responsible for mediating cell adhesion is presented in the dose-response curve shown in Figure 5-2.

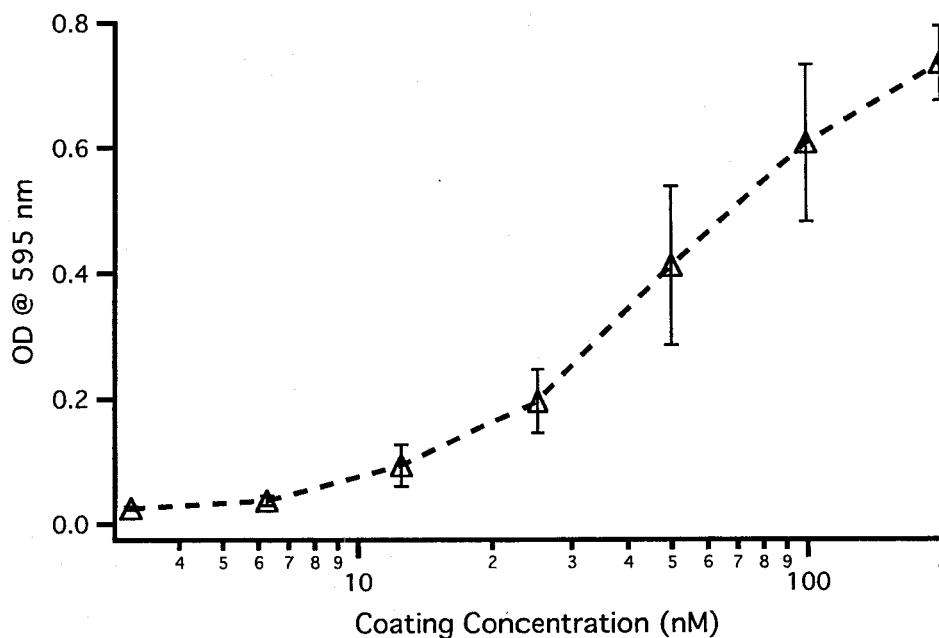


**Figure 5-2: Dose-dependency of cell adhesion on 30N coating concentration**

The number of cells adhering to b30N-coated engineered surfaces depends on the concentration of b30N in the coating solution. The zero coating concentration is not shown on this log plot, but does not differ from the lowest point shown (result =  $0.035 \pm 0.02$ ). All concentrations were run in triplicate wells; bars are  $\pm 1$  s.d.

The results presented in Figure 5-2 are representative of a number of different experiments with respect to the coating concentration of b30N required to initiate detectable levels of cell attachment. Calculations were made to determine the approximate surface coverage that this coating concentration would result in, assuming complete attachment of the biotinylated proteins in solution. For the experiment shown in Figure 5-2, which used 100  $\mu\text{L}$  of solution ( $0.1 \text{ cm}^3$ ) in a 24-well tissue culture plate (total surface area  $1.9 \text{ cm}^2$ ), a coating concentration of 6.25 nM would result in 8% surface coverage and a 12.5 nM coating concentration would result in 16% coverage.

Since the volume of solution is small, which results in a solution depth of  $\sim 0.5$  mm, and the exposure time was long (1 hour) and included mild agitation, it is reasonable to expect that all the proteins in the solution would come into contact with the surface during this coating step. Based on the rate of adsorption measured in various SPR experiments (see, for example, Figure 4-15 - Figure 4-17), which did not include agitation, the percentage of immobilization to the surface is likely to be nearly complete. Assuming, to be conservative, that 80% of the proteins do become immobilized, the total surface coverage that supports initial cell attachment as measured in this adhesion assay is between  $\sim 7 - 12\%$ . At the other end of the range, based on the same assumptions, concentrations of 100 nM or greater should result in full coverage (i.e., all available binding sites filled.) Since the level of cell adhesion continued to increase above the levels observed when a 100 nM treatment was used, it is possible that not all the protein in the solution is bound to the surface, and, by extension, the surface coverage at the lower concentrations (12.5 nM) could be even less.

Visually, the cells that remained on the surface after removing the “non-adherent” cells and fixing the remainder with paraformaldehyde (which cross-links proteins), appeared normal, and would spread if allowed to adsorb for somewhat longer (approximately 2.5 hours.) Figure 5-3 shows representative photomicrographs taken from random fields at different coating concentrations. As can be seen Figure 5-3, the cells that are attached to the surface that had been treated with the lowest concentration (12.5 nM, upper left) are differentially refractile, with some appearing dark and others



with a bright ring around them. This is probably due to differences in the proximity of the cells with the surface. The cells that appear dark are likely to be weakly associated to the surface (i.e., less tightly adherent) and those that appear light are likely to be more tightly associated which caused a phase-differential between the surface and the cells, leading to the white ring in these phase-contrast photomicrographs. This effect is not noticeable in the other images, where the cells are much more tightly bound to the surface. Also evident in Figure 5-3 is the cells' ability to spread on these surfaces (lower right) if given enough time to do so. This is further evidence that the cells are able to recognize and react to adhesive ligands immobilized on the engineered surfaces normally, at least in terms of visual morphology.

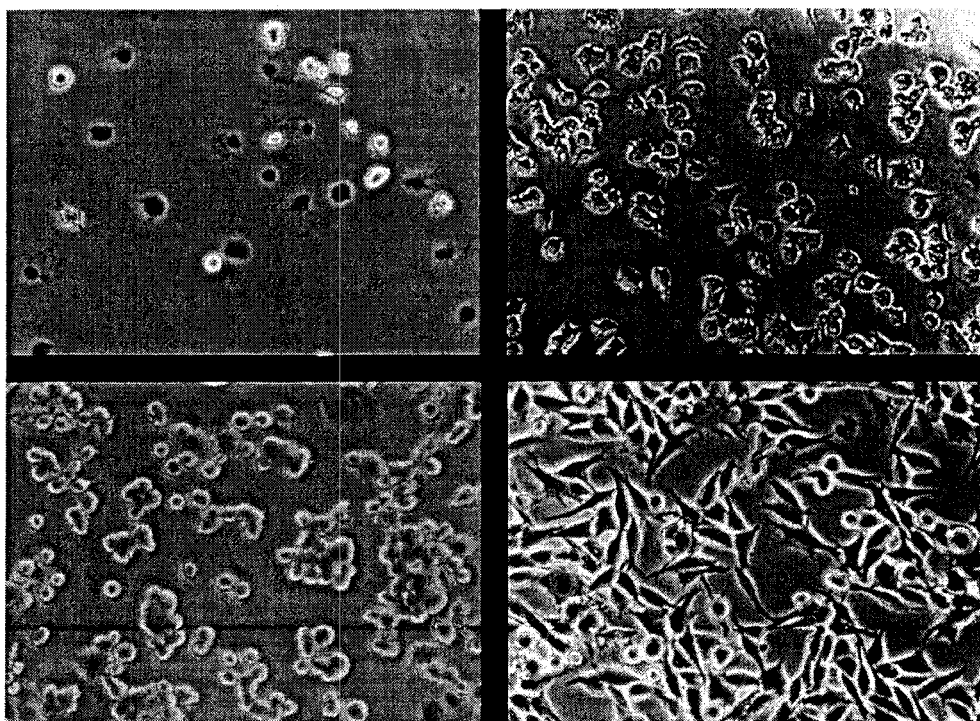


**Figure 5-3: Phase-contrast photomicrographs of adherent Moav cells at three concentrations and extended time.**

Images 1-3 were taken after attachment was allowed to proceed undisturbed for 60" and non-adherent cells washed away. Coating concentrations were (left-right, top-bottom): 12.5 nM, 100 nM, 200 nM, 200 nM. Image 4 (bottom right) was a duplicate well to image 3 (bottom left) and taken after a 2.5 hour adhesion period. All images acquired at 100x total magnification.

Further characterization of the specificity of the cell attachment mechanism will be presented shortly. But first, it is worth comparing the cell attachment to 30N that is bound to the engineered surfaces to the same ligand that is bound non-specifically to a plastic dish (in the "traditional" manner – coating the dish with a protein solution for a period of time, rinsing, and blocking with bovine serum albumin (BSA)). Figure 5-4 compares the dose-dependent Moav cell attachment to either polystyrene or the engineered surfaces that have been treated with protein solutions at the indicated concentration.

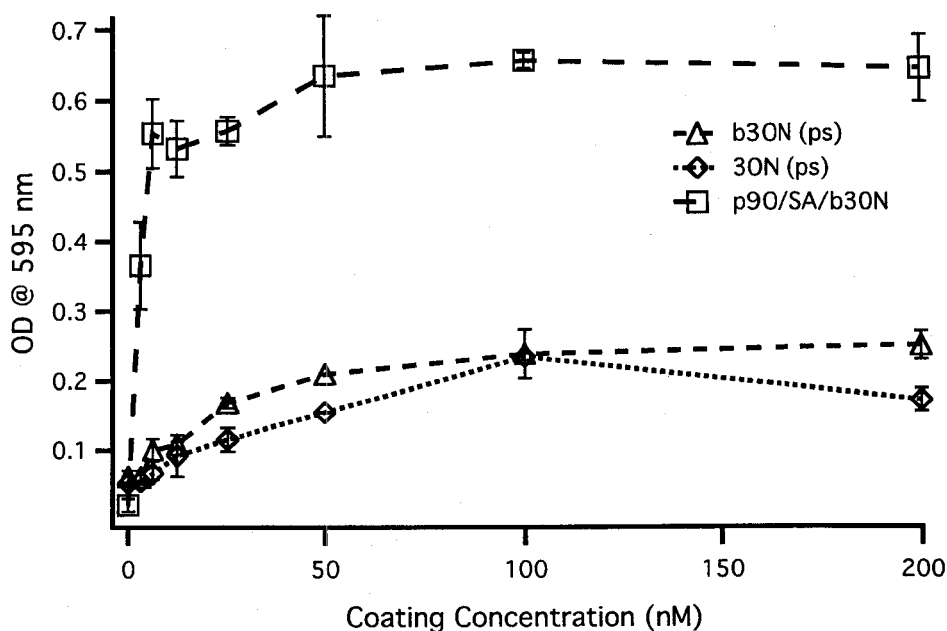


**Figure 5-4: Comparison between cell attachment to 30N coated polystyrene vs. b30N treated BCMs**

Identical coating concentrations were used for both the polystyrene plates (ps) and the engineered surfaces (p90/SA/b30N). Note the strikingly higher level of cell attachment to the engineered surfaces.

The difference in the level of cell attachment evident in Figure 5-4 can be attributed to several factors: 1) more protein binds to the engineered surfaces than to polystyrene, 2) the protein bound to the engineered surface is more accessible to the cell receptors due to the increased rotational freedom of the molecule which is tethered to the surface rather than non-specifically physisorbed, or 3) that there is a greater percentage of osteopontin on the engineered surface that is in its native conformation compared to those bound to the polystyrene. Further experimentation is necessary to differentiate between these possibilities.

One possibility that is not mentioned above is that the osteopontin bound to the engineered surfaces is more optimally oriented away from the surface, leading to a higher biological activity apparent in the cell adhesion assay. This is not listed as a factor because the conjugation method used to link the osteopontin to biotin is random and will not lead to controlled orientation. However, this method of surface immobilization opens up an interesting possibility for improving the orientation of molecules immobilized on a surface. One way to do this is as follows:

Since many of the ligands that researchers may wish to investigate have not been crystallized, and therefore it is unknown which is the proper orientation of the molecule to direct the active epitope away from the surface, the proper orientation could be “guessed at” by means of neutralizing antibodies. Assuming that the neutralizing antibodies interact with (or near) the active epitope of the protein in question, these antibodies could be used to create an immunoaffinity column. Binding the protein of interest to the column should constrain the protein such that the active epitope is buried. Using conditions suitable for conjugation with the biotinylation reagent that do not elute the protein from the immunoaffinity column, the conjugation may occur to areas of the protein away from the active epitope. Proteins conjugated thus, after elution and concentration, would, after being bound to a streptavidin adlayer, have their active epitope preferentially oriented away from the interface. It is left to an industrious graduate student to attempt such a protocol and to verify the preferential orientation of the immobilized proteins, perhaps using a spectroscopic technique based on strongly

adsorbing proteins (cytokines, hemoglobins, ferritin are several potential candidates.) This method requires the availability of neutralizing antibodies (and non-neutralizing antibodies for controls), but these should be much easier to obtain and screen than it would be to solve the protein crystal X-ray diffraction pattern of novel molecules.

Having shown that these cells will bind to surfaces treated with immobilized ligands, but not to “bare” SA coatings, and that the level of cell adhesion is dependent on the coating concentration (and, by extension, the amount of protein on the surface), we move now to demonstrating the specificity of cell adhesion.

#### **Cell adhesion to osteopontin is predominantly dependent on $\alpha_v\beta_3$ Integrin**

Integrin specificity was demonstrated using a relatively straight-forward competition assay. Three sets of identical surfaces were prepared, but this time, the cells used for seeding were pre-incubated with either an isotype-matched non-neutralizing control antibody, a neutralizing anti- $\alpha_v\beta_3$  antibody (LM609), or a mock treatment. Figure 5-5 shows the results of a representative experiment.

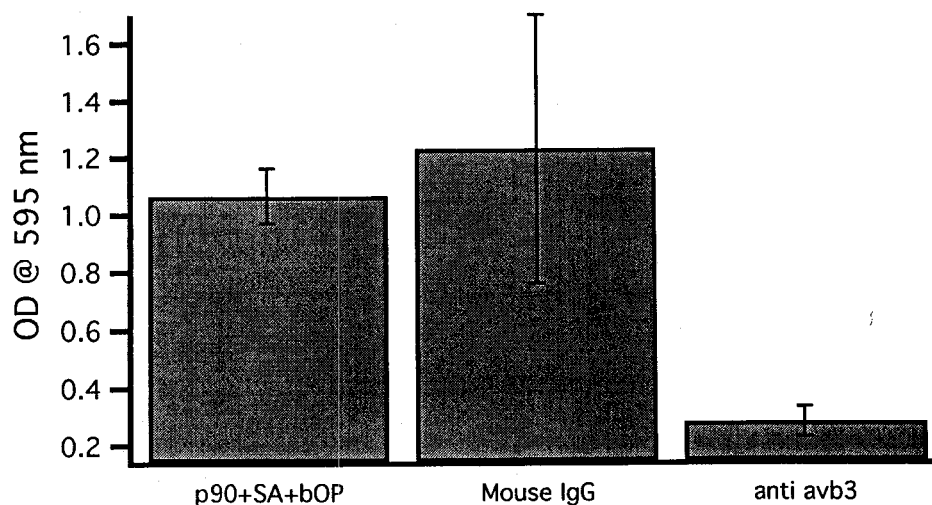


**Figure 5-5: Cell adhesion to immobilized 30N osteopontin is integrin mediated and largely dependent on alpha-v beta-3 expression**

This result shows that cell attachment can be nearly completely inhibited by pre-binding the alpha-v beta-3 integrin, demonstrating specificity of cell adhesion.

Compared with the mock treatment and the control IgG, the anti- $\alpha_v\beta_3$  IgG prevented ~70% of cell attachment. This illustrates two things: 1) that  $\alpha_v\beta_3$  predominantly mediates cell attachment to 30N osteopontin immobilized on the engineered surface, and 2) that an additional receptor is likely also recognizing the 30N fragment supporting, to a lesser degree, some cell attachment. Exhaustive characterization of which receptors might be responsible was not performed, though it is likely to be integrin(s) that are responsible, as suggested in the following set of experiments.

#### **Cell adhesion is inhibited by soluble GRGDS peptides**

To complete the picture of the specific cell recognition to the immobilized 30N and to verify biological activity of the adhesive ligand, it was necessary to show that not only

is the  $\alpha_v\beta_3$  integrin receptor responsible for mediating a large majority of cell adhesion but that the attachment was specific to the RGD peptide within the 30N fragment. The RGD peptide has been conclusively demonstrated in numerous studies to be one of the most common sequences recognized by integrin receptors mediating cell attachment to extracellular matrix proteins (such as fibronectin, osteopontin, and many others.) To demonstrate this activity, a soluble GRGDS peptide competition assay was performed. Figure 5-6 presents representative results of a peptide competition assay. It shows that inhibitor concentrations of approximately 30  $\mu\text{M}$  are sufficient to moderately inhibit  $\text{Moc}\alpha_v$  attachment to immobilized 30N, with full inhibition achieved at a peptide concentration of 100  $\mu\text{M}$  or higher. In comparison, a soluble control peptide (GRGES) even at 200  $\mu\text{M}$  did not inhibit cell attachment (inverted triangle, Figure 5-6). This conclusively demonstrates that cell attachment to the 30N osteopontin fragment immobilized to these surfaces is the same that mediates cell attachment osteopontin *in vivo*.

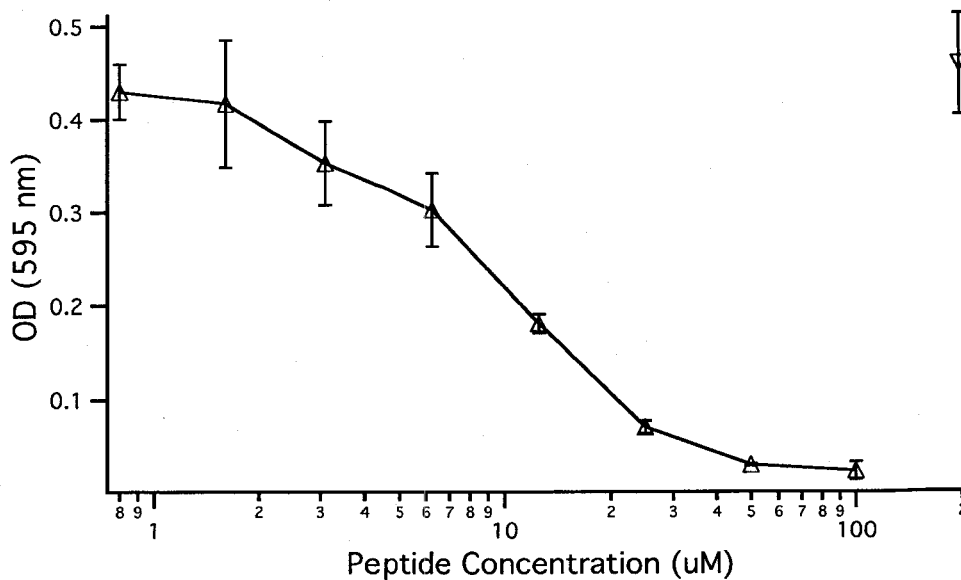


**Figure 5-6: Cell attachment to immobilized 30N osteopontin is inhibited by addition of soluble GRGDS peptide**

Data illustrate that cell attachment is dose-dependently inhibited by soluble RGD peptides (upright triangles), but not the RGE peptide (inverted triangle).

The data presented to this point have been based on immobilized an N-terminal osteopontin fragment. To show that different cells will respond to the proteins immobilized on the surface according to their receptor expression patterns, identical surfaces were created to compare the dose-dependency of cell adhesion for different cell types. Figure 5-7 shows compares adhesion of the Mo and Mo $\alpha_v$  melanoma cells and the HNB smooth muscle cells to increasing coating concentrations of osteopontin. Whereas the Mo $\alpha_v$  cells, as usual, showed strong adhesion to osteopontin treated surfaces, the Mo cells were much less adherent. This result is not due to differences in staining between the two cells, as they are equivalent in size and differ mainly by the biochemistry of their



gene expression (as described previously, they are derived from the same parent cell type.) The adhesion of the HNB cells is similar to the Mo $\alpha_v$  cells, although they are significantly larger in size and may therefore stain more strongly. Interestingly, adhesion of all three cell types is detected using this assay at the same coating concentration (62.5 nM); it is the slope of the adhesion curve that differs. The results shown in Figure 5-7 are somewhat unique in that the highest coating concentration used was 1  $\mu$ M.

Unexpectedly, cell adhesion to the two highest coating concentrations did not plateau as was predicted based on the maximal protein coverage estimations (above.) This again suggests that using this coating regime the number of ligands has not yet saturated the number of surface binding sites.

#### Cell attachment depends on integrin expression pattern and identity of immobilized ligand

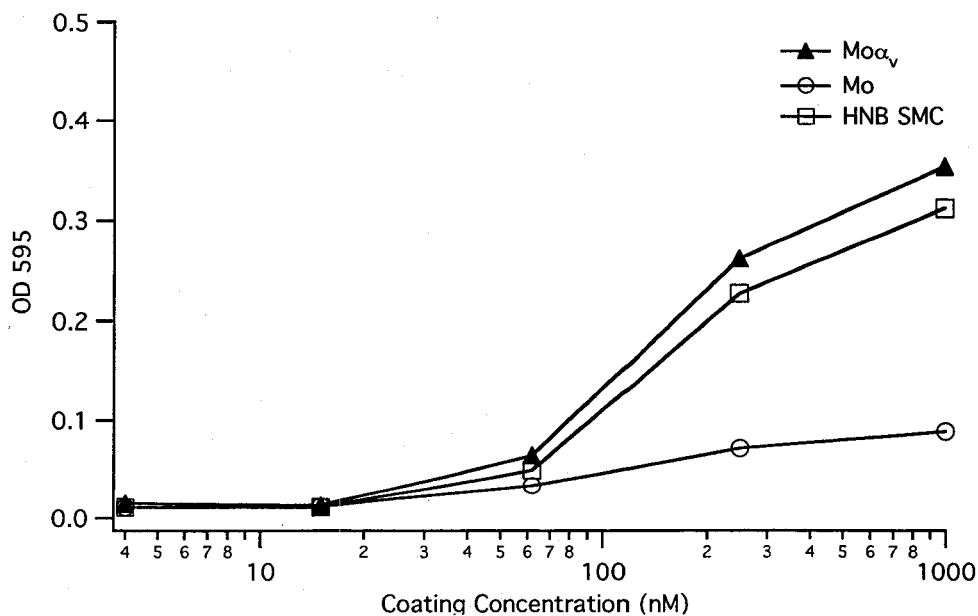


**Figure 5-7: Comparison of Mo, Moav, and HNB cell adhesion to immobilized 30N osteopontin**

Three identical sets of surfaces were prepared using BCMs and streptavidin. These three sets of surfaces were dosed with equal volumes of the osteopontin concentrations shown. Cell adhesion was measured as described in the Methods section.

In contrast to the results shown in Figure 5-7, when a similar experiment was carried out using collagen as the adhesive ligand, the results were quite different (Figure 5-8.)

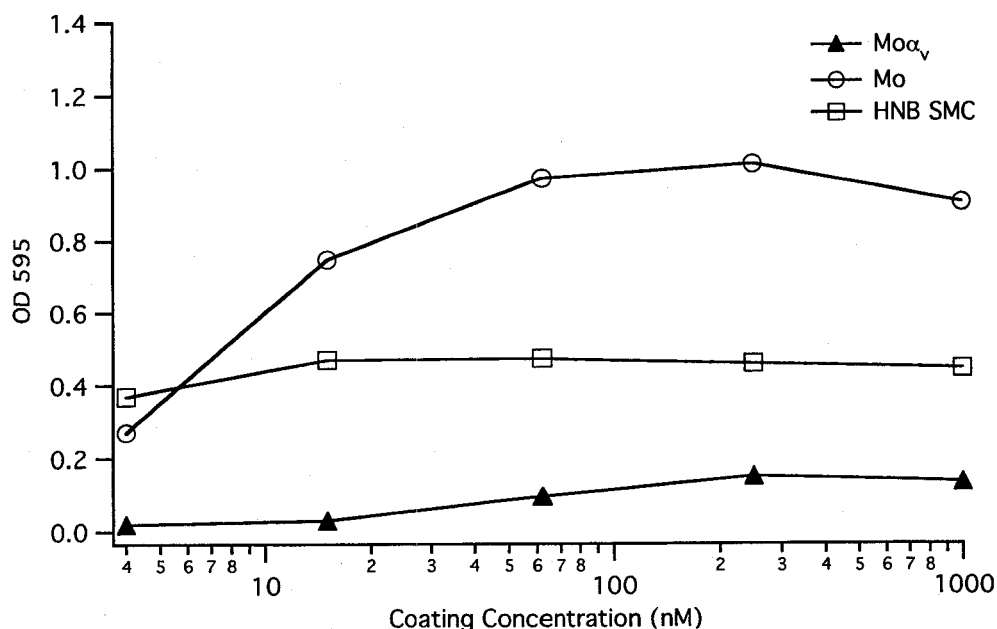


**Figure 5-8: Comparison of Mo, Moav, and HNB cell adhesion to immobilized bovine collagen I**

As in the previously described experiment, three identical sets of SA coated BCMs were prepared but in this case were dosed with biotinylated collagen rather than biotinylated osteopontin.

Compared to surfaces that were coated with osteopontin, the collagen coated surfaces strongly promoted Mo cell attachment but not Mo $\alpha_v$ , while the HNB cells

apparently reached saturation coverage even at very low collagen coating concentrations. It would appear from this result that even at the lowest coating concentration, in this case 32  $\mu\text{M}$ , sufficient collagen was bound to the surface to strongly promote cell attachment. Again in contrast to the previous data, surface ligand density apparently reached a level that promoted maximum cell binding before the highest coating concentration was reached. Actual protein quantities were not determined in this case, but one explanation could be the relatively large size of the collagen molecule ( $>10\text{X}$  the size of 30N), which may provide numerous binding sites per molecule as opposed to 1 in the 30N fragment.

#### **More than one cell adhesion ligand can be specifically immobilized to control cell response**

This immobilization strategy can be extended to using more than one ligand on the surface. As illustrated in Figure 5-9, when solutions containing different proportions of two ligands were mixed and this mixture was used to prepare the surface, the cell adhesion levels reflected the different proportions of each ligand present on the surface. This effect is particularly striking for the Mo cell type that consistently showed much higher adhesion to collagen than to osteopontin. As the proportion of collagen in the coating solution decreased from 50% to 25%, a strong decline in adhesion was noted. The reverse is true for the  $\text{Mo}\alpha_v$  cell type, which consistently displayed the opposite propensity of adhesion to collagen and osteopontin than the Mo cells did. This alternate behavior is evident in the increase in adhesion the  $\text{Mo}\alpha_v$  cells displayed as the proportion of 30N in the coating solution increased from 50% to 75%. It is worth pointing out that

the change in adhesion behavior between the Mo and Mo $\alpha_v$  cells occurs when the proportion changes from 50/50 to 25% collagen and 75% collagen. Recall that these are independently prepared surfaces, which suggests that the mechanism for adsorption (diffusion to the surface) can be used to repeatedly prepare similar surface ligand densities from a mixed solution.

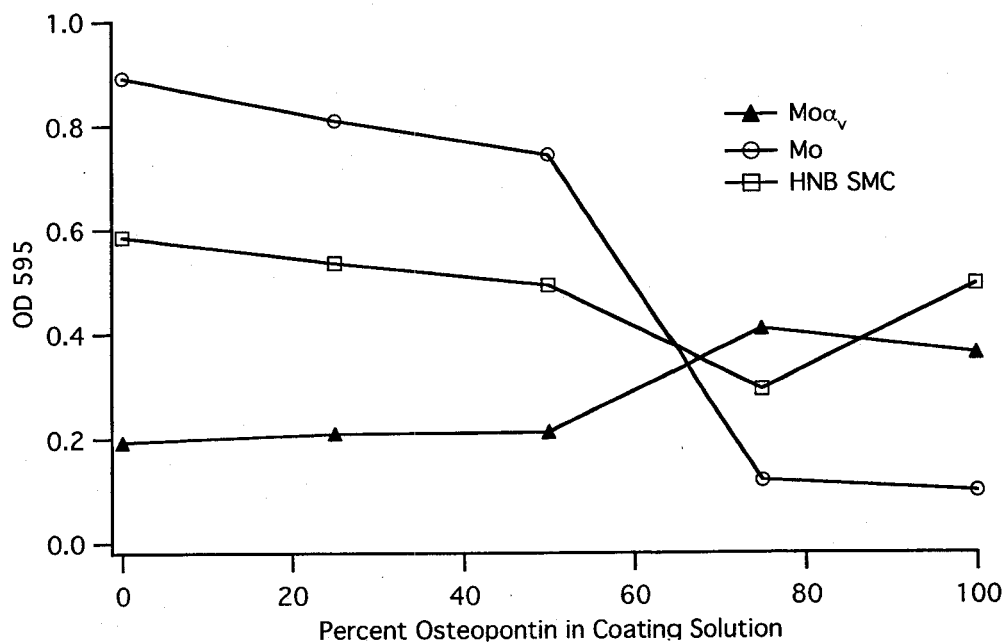


**Figure 5-9: Comparison of cell adhesion to surfaces functionalized with two integrin ligands**

In this experiment, both the biotinylated 30N and biotinylated collagen were added to the coating solution. The relative quantities of adsorbed proteins are not known, as this coating protocol is essentially a “race to the surface.” Nevertheless, the differential response of the three cell types to the different proportions of the two ligands is apparent.

The data shown in this section demonstrate that these surfaces can be used to immobilize cell adhesion ligands via a biotin linkage to a streptavidin coated surface, that cell adhesion is mediated by an integrin receptor / RGD peptide interaction, and that different substrates can be immobilized to the streptavidin coated surfaces and retain their expected biological activity.

### ***Engineering streptavidin to express an RGD-containing surface loop***

It was recognized early on that the versatility of these engineered surfaces as a tool for investigating techniques in surface engineering for controlling cell response in general and cell adhesion in particular if the streptavidin adlayer itself could display sequences that integrin receptors could bind to. This would serve at least two purposes: 1) eliminate the necessity for an additional binding step, relying on robustness and predictable behavior of streptavidin, and 2) take advantage of the availability of a recombinant protein that is relatively inexpensive for certain surface and tissue engineering studies that do not require more subtle biological activity. Implementation of this strategy was encouraged by the extensive experience our lab had in site-specific streptavidin mutagenesis, which demonstrated in many instances that the protein would tolerate significant changes in its sequence and still retain its biotin binding activity.

This strategy was also developed in part from the fact that core SA contains a GRYDGS sequence that had been identified as a cell-binding domain in some reports. However, based on X-ray crystallographic structural determinations, these residues were

shown to be buried somewhat below surface of the protein, which would make them inaccessible to cell receptors. Indeed, in our hands, wild-type (GRYDGS-containing) streptavidin does not support integrin-mediated cell adhesion (described below). It was decided that the native sequence of core streptavidin would be modified to express an RGD-containing sequence in a surface loop so that it would be more accessible to cell adhesion receptors.

#### **Location of surface loop in core recombinant streptavidin for RGD tripeptide modification**

A number of candidate surface loops were identified (Figure 5-10) from the known 3-D structure of the protein. As shown in Figure 5-10, four solvent-accessible beta-turns are located near the surface of the monomer and directed away from the center of mass of the protein. One such loop (residues 63 – 68) is near the biotin binding sites on one face of the tetramer, and would therefore be directed away from the solid interface should the protein be immobilized by the biotin binding sites on the opposite face of the tetramer (see Figure 5-12). Another factor that makes this loop a good candidate is that the wild-type sequence at residues 65-67 is RTD, so the switch to RGD is quite conservative and is likely to have little affect on the structure or stability of the folded protein. This, in addition to its solvent accessibility and location opposite from the putative surface binding face of the protein, made this loop the first choice for site-directed mutagenesis to incorporate the RGD motif.

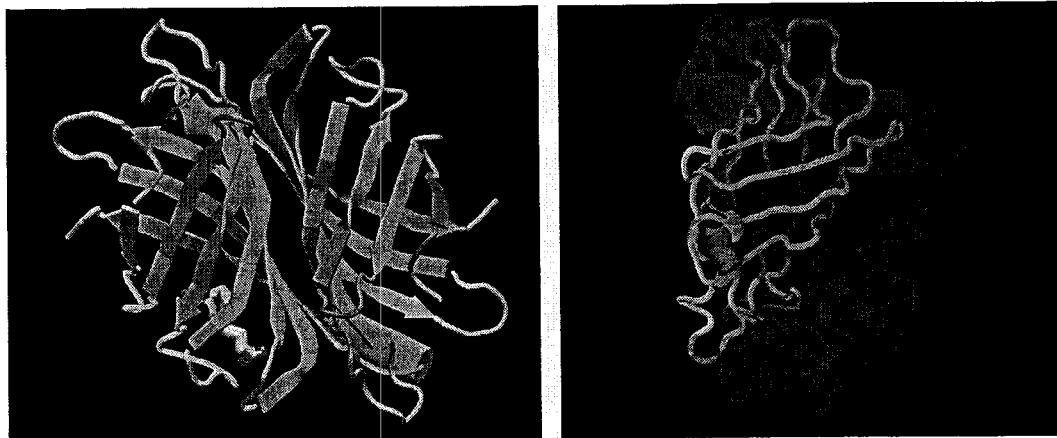


**Figure 5-10: Two representations of streptavidin dimers showing locations of surface loops**

Both images (left and right) show a dimer of streptavidin monomers (the other pair of dimers is not shown for clarity.) Biotin is shown in one of the monomers in its location observed in crystals grown from streptavidin bound to biotin. The backbone strands and CPK colors range from red (innermost) to blue (nearest the protein surface.) The surface loops, colored blue, are turns between the proteins  $\beta$ -barrel secondary structure and, as such, are relatively insensitive to changes in the residues (assuming fairly conservative sequence modifications.) The surface loop chosen for RGD expression is the one at the bottom right in the left image. Note its apposition to biotin; an identical geometry occurs on the “top” side (in the figure). This upper loop would be directed toward the bulk solution if the protein was bound to a surface via the biotin shown.

Figure 5-10Figure 5-11 show the locations of the candidate surface loops in the protein’s folded structure. Figure 5-10 shows just the backbone of one of the four monomers (in association with another monomer—the complete tetramer is not shown for clarity) with the surface loops visible, whereas Figure 5-11 demarcates the surface loops on a space-filling model of the complete tetramer.

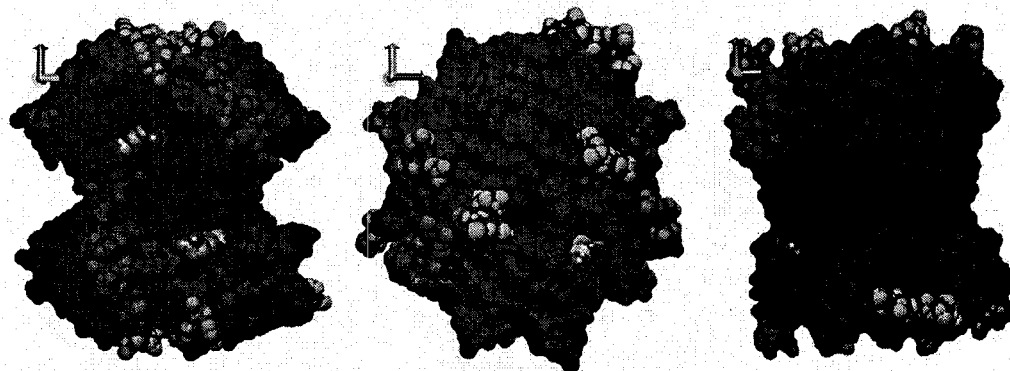


**Figure 5-11: Location of surface loop modified to contain RGD peptide**

Three orthogonal views of a space-filling model of core recombinant wild-type streptavidin are shown. Bound biotins are visible in the left view (facing the binding pockets) and the middle view (from a “pore” in on the opposite side of a monomer from the binding pocket). Surface loops that were candidates for sequence engineering have been colored in grey, blue, silver, and red. The red loop was selected for site-directed mutagenesis.

As described earlier, residues 65-67 are positioned very near the biotin-binding pocket of one of the adjacent monomers (Figure 5-11). Due to the dyad symmetry of this homotetrameric protein, if it is attached to a surface via one or two of its biotin-binding sites, as it would be on a biotin-containing monolayer, the RGD-containing loop would be oriented toward the bulk solution as depicted in Figure 5-12. This is the preferred orientation for interaction with a cell-surface receptor, and further favors this segment of the polypeptide for directed mutagenesis.



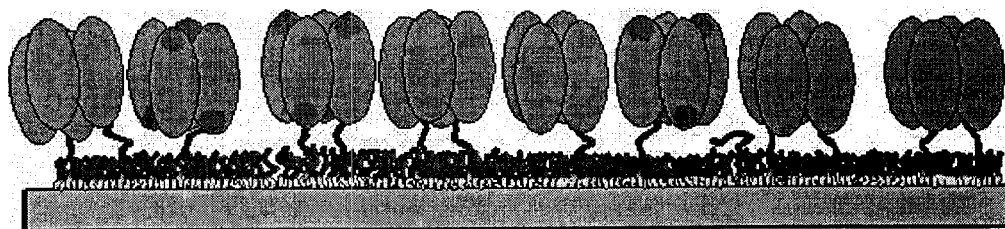


**Figure 5-12: Conceptual illustration showing location of RGD peptide loops engineered into core streptavidin and bound to biotin-functionalized SAMs**

Based on the depiction of the engineered surfaces, the selected surface loop was chosen for its accessibility to the bulk volume when the protein is specifically bound to the BCM. A mixture of wild-type (all grey) and RGD-containing SA (red-tipped) proteins are shown in the figure. The location of the surface loop is shown in red.

Several different variants were tried before obtaining one that was both stable in solution and bound to integrin receptors.

#### **Variants of RGD containing streptavidin created and tested**

In total, four different variants of streptavidin were constructed. The first, denoted CP/RGD-SA (described in more detail below) was found to spontaneously denature. Due to its instability, it was not tested for biotin binding or RGD mediated cell adhesion properties. The next variant, designated RGD-SA, was stable but did not promote cell adhesion. The last two, denoted FN-SA and OPN-SA, successfully promoted RGD / integrin mediated cell attachment. Biotin binding affinity of FN-SA and OPSA was determined to be indistinguishable from wild-type. The locations and sequences chosen for the different RGD-containing streptavidin variants are detailed in Table 5-2.

**Table 5-2: Sequence comparison of engineered SA variants expressing an RGD cell adhesion motif.**

The sequences of the four variants are compared to the wild-type sequence (core WTSA). The last two variants, FN-SA and OPSA, contained two additional residues (64A and 67A) not present in wild-type or the first two variants created. \*The N-terminus of the CP/RGD-SA begins with this sequence. The C-terminus of this circularly permuted protein ends at residue 67 and the original (wild-type) C-terminus was linked to the original N-terminus by the tetrapeptide Gly-Gly-Gly-Ser. Additional details are given in the text.

	Residue #							
Variant designation	64	64A	65	66	67	67A	67B	68
Core WTSA	Pro	--	Arg	Thr	Asp	--	--	Gly
CP/RGD-SA	Pro	--	Arg	Thr	Asp	--	*MCDRGDSVC	Gly
RGD-SA	Pro	--	Arg	Gly	Asp	--	--	Gly
FN-SA	Pro	Gly	Arg	Gly	Asp	Ser	Pro	Gly
OPN-SA	Pro	Gly	Arg	Gly	Asp	Ser	Val	Gly

The first variant to be constructed, named CP/RGD-SA (for “circularly permuted, RGD-containing streptavidin”) was created from a gene construct that had two streptavidin monomer genes in tandem, connected by a GGGS linker. This construct, provided by Vano Chu, was used to create a gene coding for a single monomer by PCR amplification. Figure 5-13 illustrates how a gene for a circularly permuted streptavidin gene is constructed.

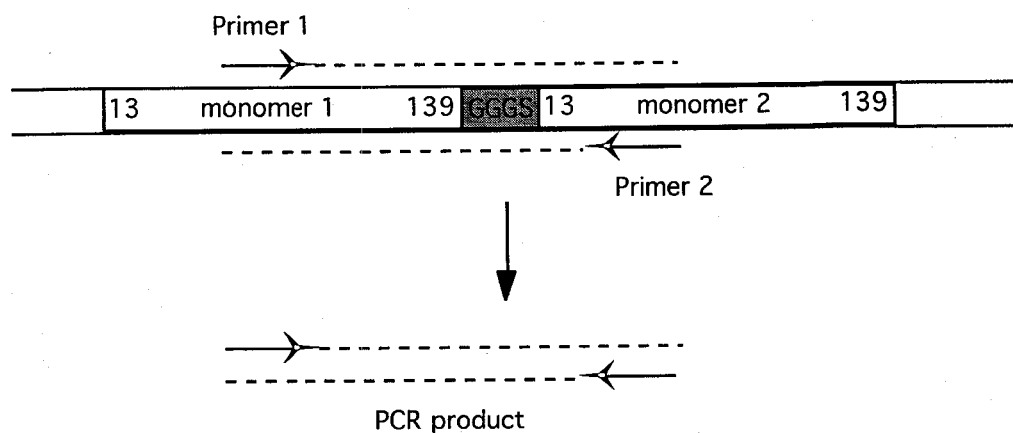


**Figure 5-13: Creating a circularly permuted protein from a tandem gene plus linker.**

A recombinant DNA sequence that codes for two tandem streptavidin monomers (monomer 1 and 2) attached by a GGS linker sequence. A circularly permuted streptavidin monomer is created using PCR amplification by selecting a primer sequence complementary to the codons where the new monomer will begin, the second primer 130 residues downstream. The PCR product is then cloned into an expression vector for protein production. For the circularly permuted RGD streptavidin, the upstream linker contains additional codons for MCDRGDSVC, the remaining streptavidin sequence is identical to wild-type (plus the linker.)

The CP/RGD-SA construct was created using a primer that has a 5' sequence homologous to codons that begin at the codon for residue 67 and several codons downstream. The 3' residues code for the RGD sequence to be included in the new construct. This peptide is spanned by two cysteine residues included to form a disulfide bond to encourage stable secondary structure. Unfortunately, despite these efforts, after expression, the protein folded state was observed to be unstable as aggregates accumulated in the tube over time and the protein concentration solution concomitantly decreased. As a result of the instability of the CP/RGD-SA folded state, further attempts to characterize its activity were abandoned.

The next attempt was to simply change the threonine at position 66 with a glycine to establish the RGD sequence at residues 65-67. This time, the protein was stable, but did not support cell adhesion

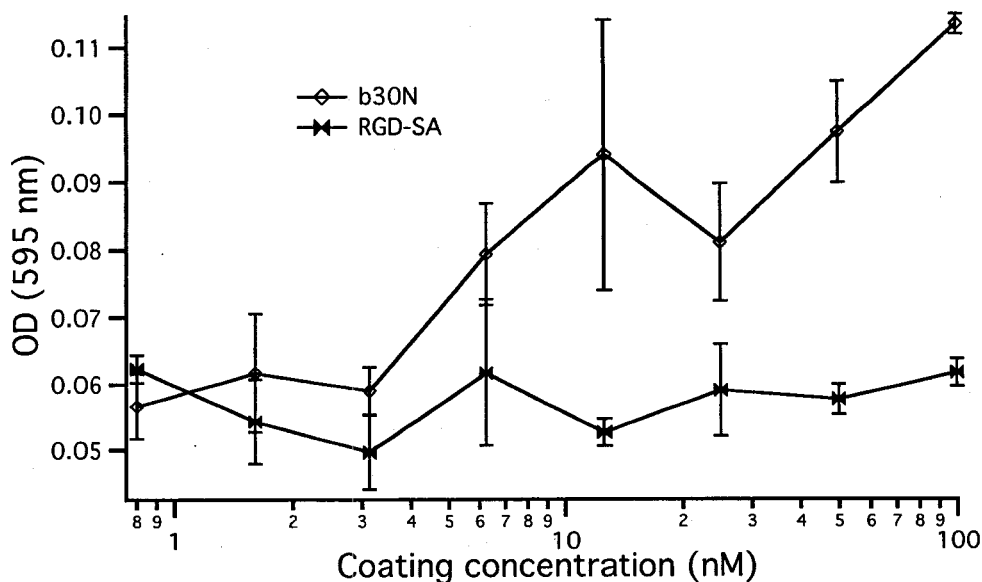


**Figure 5-14: Comparison between cell adhesion to immobilized osteopontin and RGD-SA.**

Cell adhesion to osteopontin serves as a control for the results from the immobilized RGD-SA series, which shows no change between zero (not shown on the log plot) and 100 nM coating concentration (which will saturate the surface.)

The failure of this streptavidin variant to promote cell attachment led to the next iteration that included two additional residues surrounding the RGD peptide, one that is identical to the fibronectin type-III domain RGD containing sequence, the other identical to the osteopontin RGD containing sequence. These additional residues were added to improve the homology of the flanking sequence in an effort to increase potential binding

energy between the sequence and the integrin receptors and to increase its distance from the surrounding surface of the protein. As the saying goes, “The third time’s the charm.” Both the FNSA and OPSA streptavidin variants strongly supported cell adhesion, compared to the wild-type control (Figure 5-15)

### Cell adhesion and specificity to RGD tripeptide containing engineered streptavidin variants

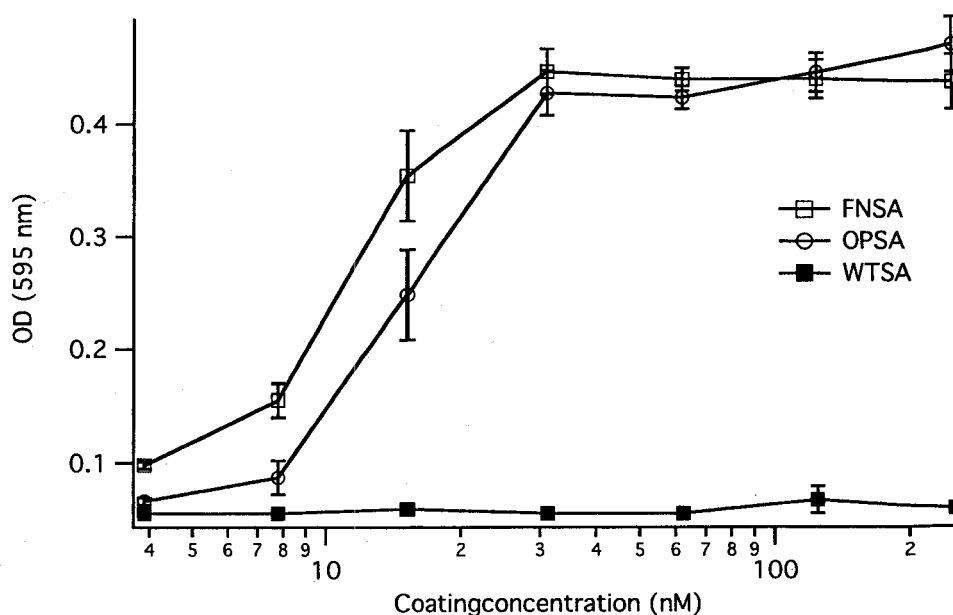


### Figure 5-15: Streptavidin variants expressing RGD peptide promote cell adhesion.

Similarly to previous dose-dependencies, increasing the coating concentration of the RGD containing SA variants results in a dose-dependent increase in cell adhesion. In contrast, WTSA does not support cell adhesion, at least for the Mo $\alpha_v$  cell line used in this experiment.

As shown in Figure 5-15, both of the two different RGD-containing sequences supported cell adhesion. Furthermore, it was observed that even the lowest coating concentration used (32 nM) promoted cell attachment greater than the WTSA control.

While this stands in contrast to the concentrations needed to promote cell adhesion using the biotinylated 30N fragment (Figure 5-2), because of the tetrameric structure of streptavidin, each protein contains two binding sites, effectively doubling the density of cell attachment sites over the number achievable using the 30N fragment.

Also apparent from the experimental data shown in Figure 5-15 is that the FNSA variant promotes somewhat greater cell adhesion than the OPSA variant does. This effect was reproducible. Since the peptide sequences of these two variants differ by only one residue, evidently the additional proline residue present on the end of the engineered RGD-containing peptide sequence encourages a stronger or more optimal fit between the protein and its putative receptor.

We showed next that cell attachment to the FNSA and OPSA variants was mediated by RGD by carrying out an inhibition assay similar to those described in Figure 5-6. As before, pre-incubating the cells with soluble RGD peptide inhibited cell attachment in a dose-dependent fashion, whereas the soluble RGE peptide had no effect, even at a concentration as high as 200  $\mu\text{M}$  (Figure 5-16.) This result demonstrates that cell attachment to the RGD-containing SA mutants was indeed determined by the incorporated RGD peptide sequence. The next obvious question is whether the binding is integrin mediated. Figure 5-17 summarizes the results of an experiment carried out by pre-incubating the  $\text{Mo}\alpha_v$  cells in one of two monoclonal antibodies, either anti- $\alpha_v\beta_1$  (the common fibronectin receptor) or anti- $\alpha_v\beta_3$ , which has been shown to be fairly

promiscuous (i.e., recognizes and binds to a wide variety of RGD containing ligands as binding partners.)

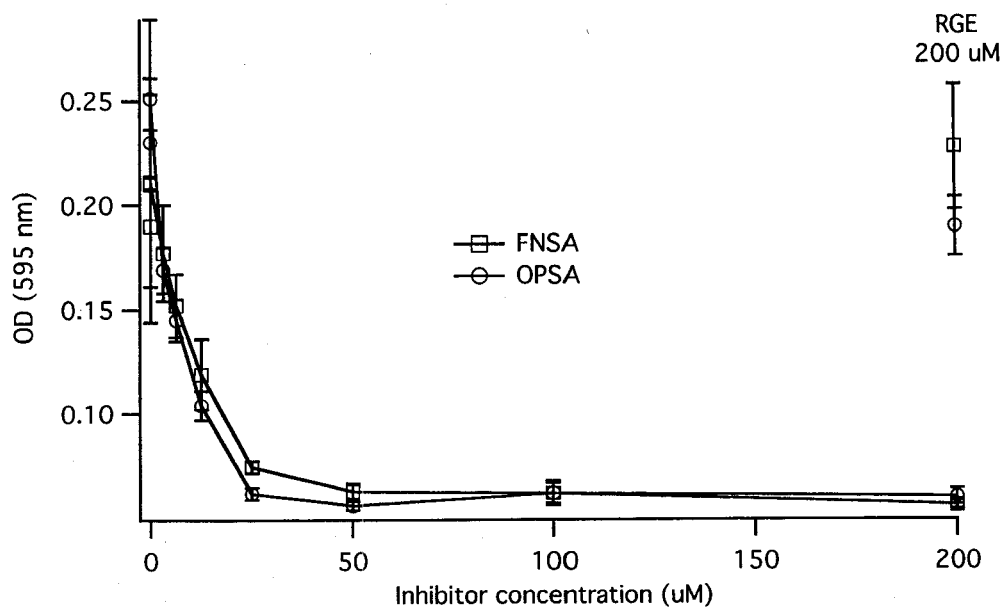


**Figure 5-16: Cell adhesion to RGD containing streptavidin variants is RGD dependent**

Cells were pre-incubated with the indicated concentrations of soluble RGD or RGE containing pentapeptides for 15 minutes before seeding them onto surfaces coated with either the FNSA or the OPSA variant.

Interestingly, Figure 5-17 shows that the anti- $\alpha_5\beta_1$  antibody appeared to simulate cell adhesion over the no-antibody control. This outcome is probably caused by the antibody activating the integrin receptors, probably by cross-linking them. As such, it was a poor choice for this experiment that was initially designed to test whether the  $\alpha_5\beta_1$  integrin recognized either of the SA variants. Nevertheless, the complete inhibition caused by the

LM609 antibody should leave no doubt as to which integrin is responsible for mediating cell attachment to FNSA and OPSA (though not 30N, as also shown in Figure 5-5.)

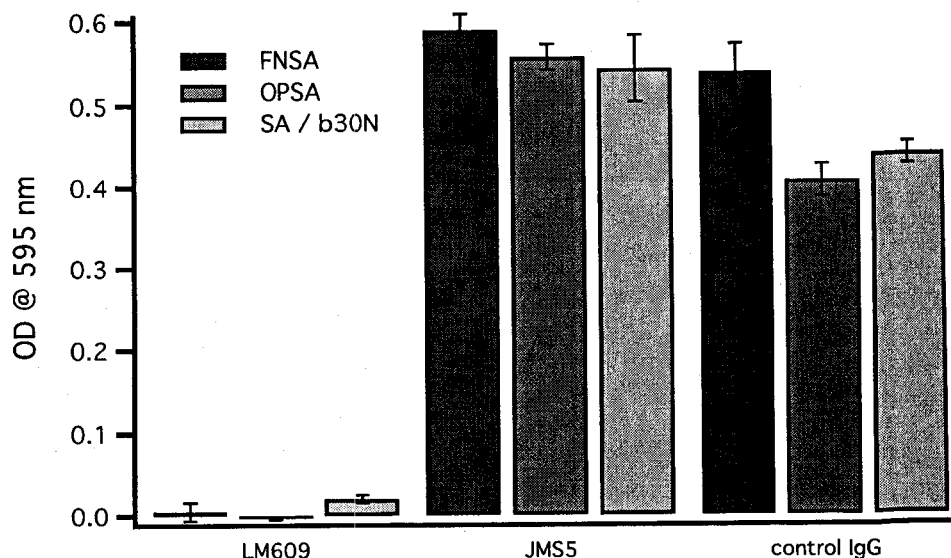


**Figure 5-17: Cell adhesion to RGD containing streptavidin variants is mediated by alpha-v beta-3 integrin**

This inhibition assay was designed to test both the  $\alpha_5\beta_1$  and  $\alpha_v\beta_3$  integrins to determine the receptor responsible for mediating adhesion to the FNSA or OPSA variants. Compared to the control IgG, LM609 blocked all cell attachment, whereas  $\alpha_5\beta_1$  seemed to activate attachment.

Taken together, these results show that the RGD-containing SA variants are biologically active as demonstrated by their ability to dose-dependently promote cell adhesion that is mediated by the RGD- $\alpha_v\beta_3$  integrin bond. These RGD mutants may be of use in a variety of biotechnology applications, and contribute to the breadth and depth of the bioengineer's "toolbox." They are particularly useful for applications in which the tight binding of biotin or biotinylated reagents are necessary, though they also represent a



platform for further site-directed mutagenesis modeled after other binding-site mutants with well-characterized dissociation kinetics.

### Top layer determines adhesion to SAMs

An interesting tidbit was observed in other explorations using the RGD variants. An experiment was carried out to measure how much additional cell attachment could be achieved if the biotinylated 30N fragment was added to FNSA coated BCMs. The results are shown in Figure 5-18. Unexpectedly, the amount of cell attachment to a FNSA layer that had been dosed with 30N was actually somewhat less than (though similar to) a plain SA surface dosed with the same 30N concentration. However, when FNSA alone was present, the level of attachment nearly doubled. This seems to suggest that the cells are recognizing only the uppermost layer of the protein multilayer. In other words, the immobilized 30N seems to “get in the way” of the cells contact with the FNSA layer.

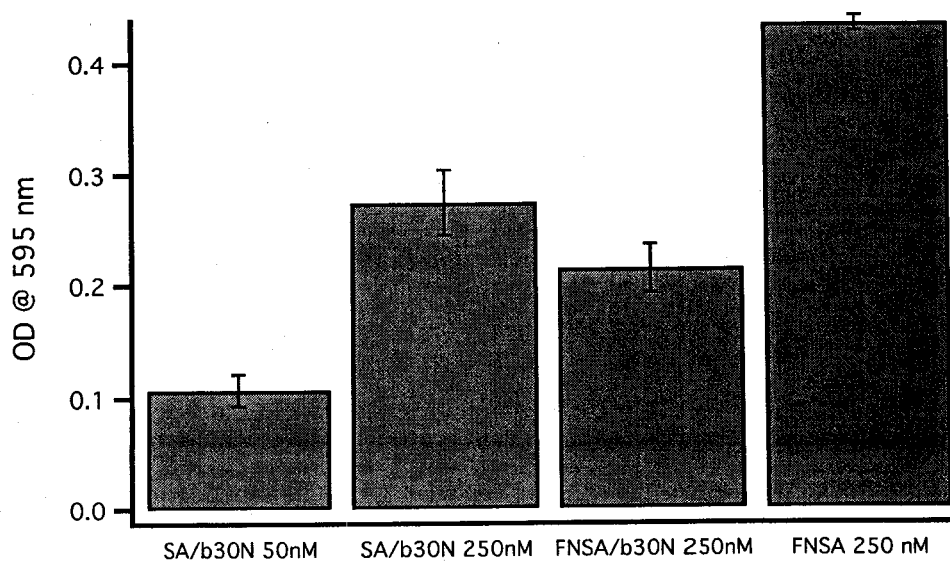


**Figure 5-18: Cell adhesion is determined by uppermost ligand.**

The first two bars (from left) confirm the expected cell binding dependency on the concentration of ligand used. The next two results suggest that when 30N is bound to the top of the FNSA layer, binding is mediated only by 30N (compare to last result of FNSA only.)

The same mechanism can explain the next set of results, where an uncommonly used BCM that contains the hydrophobic MHD diluent that supports non-specific protein binding was used to determine whether cells can probe deep below the adlayer surface. It was expected that the presence of the MHD diluent would allow the non-specific attachment of the 30N fragment. Figure 5-19 shows the conditions used for this series of adhesion experiments and their outcomes.

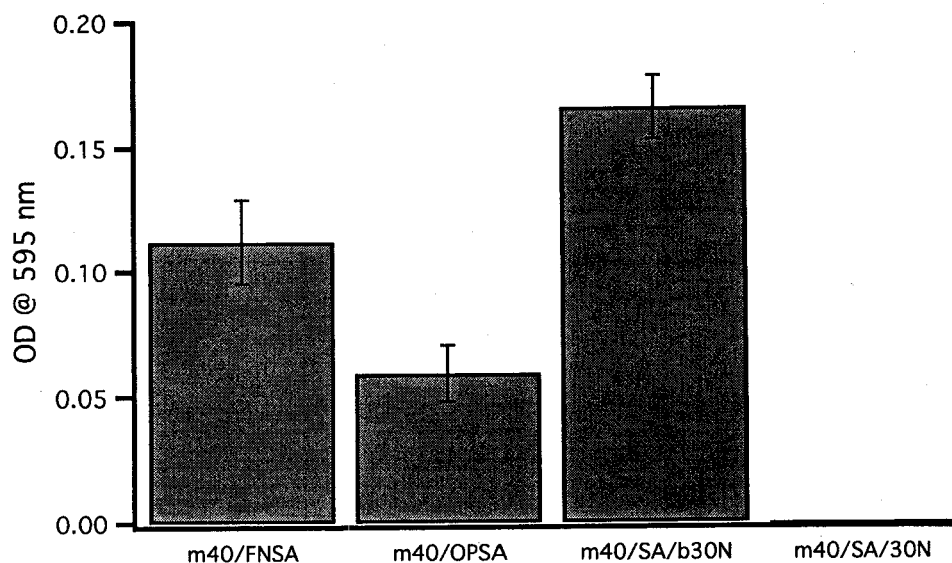


**Figure 5-19: Additional evidence that "uppermost" ligand is responsible for cell attachment**

The bottom axis describes the components used to create the adhesion substrates. M40 indicates that the BCM was assembled using 40% MHD and 60% BAT, resulting in a nearly 50/50 proportion of two thiolates in the completed film.

Oddly enough, this time, the cell attachment caused by the FN3A and OP3A proteins was less than that caused by the protein multilayer incorporating 30N. This may have been an anomalous result, though it is also possible that the hydrophobic interface could have caused some change in the average orientation of the protein that the tethered 30N did not suffer from. Such a change in orientation or conformation may have resulted in the lesser cell attachment than expected based on the majority of experiments comparing the RGD-containing SA protein to 30N containing multilayers. The data originally desired when carrying out this experiment is shown at the far right. It was expected that the relatively small 30N fragment could find interstices in the SA adlayer and come into contact with the hydrophobic layer below. Evidently this is either not the case, or if it is, that cells are not able to probe this far into the protein adlayer.

One last little tidbit is shown in Figure 5-20.

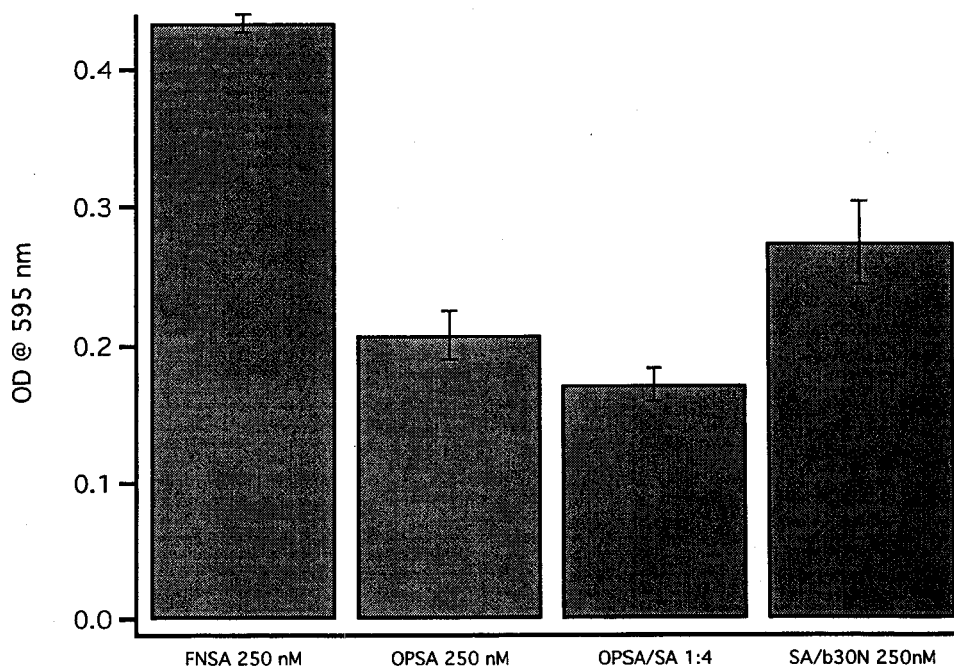


**Figure 5-20: Maximum surface density of immobilized SA exceeds cell receptor density by at least 4:1**

### *Chapter Summary and Conclusions*

We set out to demonstrate that these engineered surfaces could be used as cell culture substrates, and immobilization of receptor ligands by this method would not adversely affect the biological activity and specificity of the immobilized molecules. We have shown that immobilized integrin ligands do indeed strongly support cell adhesion. In comparison to the same ligand bound non-specifically to polystyrene, in fact, 30N osteopontin immobilized via biotin-conjugation and binding to a SA adlayer promotes

greater cell adhesion, possibly due to a greater amount of protein bound to the surface in a “native” conformation, or due to greater rotational mobility of the immobilized ligand.

Moreover, we have demonstrated that the cell culture substrates are well-behaved in that non-ligand mediated cell adhesion to streptavidin treated BCMs is prevented by streptavidin conditioning. Furthermore, cell adhesion to specifically immobilized RGD-containing integrin ligands has been shown to be RGD mediated and integrin-specific. Cells that expressed different integrin subsets responded to different immobilized ligands as shown by differential cell adhesion. An extension of this was that protein multilayers containing mixtures of ligands supported cell attachment that varied by cell integrin expression and the amount of adsorbed ligand.

We have also created an engineered streptavidin that expresses an RGD-containing peptide sequence on a surface loop (FNSA and OPSA), and have shown that these engineered variants will support integrin-mediated cell adhesion. It appears that the length and sequence of RGD containing loop strongly influences this ability, as demonstrated by the necessity of adding two flanking residues to the RGD loop before the engineered SA would support cell adhesion. Importantly, cell adhesion to RGD variants was also shown to be integrin-mediated and RGD specific.

Finally, we note that the “uppermost” ligand layer appeared to mediate cell/surface interactions.

In summary, these engineered surfaces have a demonstrated capability and flexibility for supporting cell attachment that is mediated by the specific, selective, quantitative, high affinity SA-biotin coupling.

## 6. Summary and Conclusions

We have achieved all of the main objectives of this study. We set out to implement method for specifically modifying surfaces suitable for cell culture experiments such that we could control both non-specific protein binding and allow the binding of a protein(s) of our choosing to the surface. We also aimed to achieve high-affinity, quantifiable protein binding of those we proteins we wished to immobilize for further study. And having immobilized selected proteins, we aimed to demonstrate that adhesion dependent mammalian cells would recognize and respond to them in a “natural” way (that is, such that their response is very similar-if not identical-to the way that they respond to the same proteins encountered *in vivo*). Having done so, we would have developed a tool for cell culture experimentation that was better suited for studying how cells interact with proteins on a surface. With this tool, we could then proceed with cell culture studies to identify and characterize the biochemical pathways regulated by the specific cell-protein interaction. Ultimately, one could use this tool to identify those proteins that possess and/or stimulate the biological activity or desired outcome, such as controlled healing of biomaterial devices. Such a tool has been developed and characterized.

We have demonstrated that the chemical interface is nearly entirely defined by the molecules used for surface modification. We have shown how the molecules used for modification assemble spontaneously on the surface, and we have detailed how their

assembly is controllable by varying the conditions of under which they assemble (in this case, the thiol composition of the “assembling solution”). We found that mixing two thiols, either a biotin-containing thiol and a shorter chain, hydrophobic or hydrophilic diluent thiol, we could produce films with mixed thiolate composition, and that their composition determined (or was correlated with) their architecture.

We have shown that the mixed SAMs are oriented with their endgroups that we chose for controlling surface chemistry directed toward the new interface. A very important exception to this general outcome is that the BAT molecules, when assembled by them selves, do not orient well, presumably burying desired functionality (the biotin end group) and exposing undesired functionality (the sides of the thiolate chains.) We have also shown that the different compositions have varied regularity of bond orientation, with those SAMs containing the MHD thiolate exhibiting more regular carbon bond orientation than the SAMs containing either the BAT or the OEG thiolate. We suggest that the lack of regular bond orientation in SAMs composed of BAT or OEG assist in their ability to inhibit non-specific protein binding by creating an entropic cost for restricting their rotational freedom.

Using these mixed BCMs, we have shown that we can control the specific and non-specific binding of streptavidin. This is critical for the success of this surface modification strategy, as the extremely high affinity and unique geometry of streptavidin make it a very useful and common “molecular adaptor” for the further immobilization of many different types of ligands. We have shown that the binding of streptavidin to



BCMs varies with the amount of BAT present in the film, with routinely achievable densities ~80% of the density of a 2-D streptavidin crystal. Through the use of streptavidin biotin affinity mutants, we have explored and characterized how the SA molecules are attached to the surface, and we have quantitated the strength of binding to the surface and compared it to the strength of biotin binding to proteins in homogeneous solution. By doing so, we have defined the BCM composition that promotes the highest amount and maximum stability (i.e., avidity) of SA binding. We have shown that at this composition ( $0.1 < \chi_{\text{BAT}} < 0.3$ ) the SA molecules bound to the surface are dominated by those bound to the surface by two, rather than just one, biotin linkage. This results in a decrease in the observed off-rate roughly equal to square of the singly bound SA.

Using this optimized SA-binding surface, we have shown that we can controllably immobilize biotin-conjugated proteins. Biotin is necessary and sufficient to immobilize ligands onto the SA adlayer. Two different ligands were immobilized, a small, globular, RGD containing integrin ligand (the 30N terminal fragment of osteopontin) and a large, fibrillar, non RGD-containing extracellular matrix protein (collagen type I.) We have further demonstrated that the amount of these different proteins we were able to bind was controlled by the ratio between their molecular size and the number density of SA molecules, and hence the number density of binding sites, on the surface. Finally, we have demonstrated our ability to immobilize more than one of these ECM components to the SA surface, and that the amount of the two different ligands that would bind to the

surface was quantifiably controlled by their relative size, their coverage relative to each other and to the number density of SA molecules that define the binding surface.

Having immobilized these integrin ligands on the surface, we have finally demonstrated that they retain their natural ability to promote cell adhesion via specific receptors and their associated biochemical pathways. Cell attachment to the immobilized ligands was mediated by their integrin receptors' interaction with either the RGD containing ligand or collagen only. Adhesion was dose-dependent, as was the inhibition of cell adhesion using soluble competitors. Cell attachment was variable with the cell types' integrin receptor expression pattern and the type of and relative proportion of the immobilized ligands. On top of all this, we have even engineered an RGD containing loop directly into wild-type streptavidin itself, producing an engineered protein that stimulates specific integrin-mediated and RGD dependent cell adhesion without adversely affecting the affinity this streptavidin variant has for biotin. Since this protein is recombinantly produced, it can be made cheaply at scale, and in combination with the optimized surface modification method described here, establishes a convenient, reliable method for immobilizing a high density of integrin ligands on a surface much more cheaply than by using a low-conversion scheme and purified ligands; this combination of reagents may be useful in a wide range of biotechnology applications requiring generalized cell adhesion.

In closing, through these efforts we have contributed a system of surface modification that controls a selected range of surface protein activity enabling the rapid,

selective, high affinity binding of ligands of one's choosing for the purposes of studying and controlling specific, active cell responses to model biomaterial surfaces. We are hopeful that this model system will prove to be useful for the development of improved life-saving or life-enhancing engineered materials.

## Bibliography

- Adams, D. O. and T. A. Hamilton (1984). "The cell biology of macrophage activation." Annu Rev Immunol **2**: 283-318.
- Bain, C. D., H. A. Biebuyck, et al. (1989). "Comparison of Self-Assembled Monolayers on Gold: Coadsorption of Thiols and Disulfides." Langmuir **5**(3): 723-727.
- Bain, C. D., J. Evall, et al. (1989). "Formation of Monolayers by the Coadsorption of Thiols on Gold: Variation in the Head Group, Tail Group, and Solvent." J. Am. Chem. Soc. **111**: 7164-7165.
- Bain, C. D., E. B. Troughton, et al. (1989). "Formation of Monolayer Films by the Spontaneous Assembly of Organic Thiols from Solution onto Gold." J. Am. Chem. Soc. **111**(1): 321-335.
- Bain, C. D. and G. M. Whitesides (1988). "Molecular-Level Control over Surface Order in Self-Assembled Monolayer Films of Thiols on Gold." Science **240**: 62-63.
- Bain, C. D. and G. M. Whitesides (1989). "Attenuation Lengths of Photoelectrons in Hydrocarbon Films." J. Phys. Chem. **93**(4): 1670-1673.
- Bain, C. D. and G. M. Whitesides (1989). "Formation of Monolayers by the Coadsorption of Thiols on Gold: Variation in the Length of the Alkyl Chain." J. Am. Chem. Soc. **111**: 7164-7175.
- Beninati, S., D. R. Senger, et al. (1994). "Osteopontin: its transglutaminase-catalyzed posttranslational modifications and cross-linking to fibronectin." J Biochem (Tokyo) **115**(4): 675-82.
- Castner, D. G., K. Hinds, et al. (1996). "X-ray photoelectron spectroscopy sulfur 2p study of organic thiol and disulfide binding interactions with gold surfaces." LANGMUIR. Vol. 12, no. 21, OCT 16 **12**(21): 5083.
- Davies, J. E. (1996). "In vitro modeling of the bone/implant interface." Anat Rec **245**(2): 426-45.
- DiPietro, L. A. (1995). "Wound healing: the role of the macrophage and other immune cells." Shock **4**(4): 233-40.
- Dubois, L. H. and R. G. Nuzzo (1992). "Synthesis, Structure and Properties of Model Organic Surfaces." Annu. Rev. Phys. Chem. **43**: 437-463.
- Epstein, W. L. and K. Fukuyama (1989). "Mechanisms of granulomatous inflammation." Immunol Ser **46**: 687-721.
- Folkers, J. P., P. E. Laibinis, et al. (1992). "Self-Assembled Monolayers of Alkanethiols on Gold: Comparisons of Monolayers Containing Mixtures of Short- and Long-

- Chain Constituents with CH(3) and CH(2)OH Terminal Groups." Langmuir **8**: 1330-1341.
- Gailit, J. and R. A. Clark (1994). "Wound repair in the context of extracellular matrix." Curr Opin Cell Biol **6**(5): 717-25.
- Giachelli, C. M., N. Bae, et al. (1993). "Osteopontin is elevated during neointima formation in rat arteries and is a novel component of human atherosclerotic plaques." J Clin Invest **92**(4): 1686-96.
- Green, N. M. (1975). "Avidin." Adv-Protein-Chem **29**: 85-133.
- Green, N. M. and M. A. Joynson "A preliminary crystallographic investigation of avidin." Biochem-J. 1970 Jun. **118**(1). P 71-2.
- Green, N. M. and E. J. Toms "Purification and crystallization of avidin." Biochem-J. 1970 Jun. **118**(1). P 67-70.
- Grunze, M. (1993). "Preparation and characterization of self-assembled organic films on solid substrates." Physica Scripta Volume T  
13th General Conference of the Condensed Matter Division of the European Physical Society in Conjunction with Arbeitskreis Festkorperphysik Deutsche Physikalische Gesellschaft, 29 March-2 April 1993 T49B: 711-17.
- Harder, P., M. Grunze, et al. (1998). "Molecular Conformation In Oligo(ethylene glycol)-Terminated Self-Assembled Monolayers on Gold and Silver Surfaces Determines Their Ability To Resist Protein Adsorption." J. Phys. Chem. B **102**(2): 426-436.
- Haskill, S., A. D. Yurochko, et al. (1992). "Regulation of macrophage infiltration and activation in sites of chronic inflammation." Ann N Y Acad Sci **664**: 93-102.
- Hauser, C. J. (1996). "Regional Macrophage Activation After Injury and the Compartmentalization of Inflammation in Trauma." New Horizons **4**(2): 235 - 251.
- Hausling, L., Michel, B., Ringsdorf, H., Rohrer, H. "Direct Observation of Streptavidin Specifically Adsorbed on Biotin-Functionalized Self-Assembled Monolayers with the Scanning Tunneling Microscope." Angew. Chem. Int. Ed. Engl. **30**(5): 569-572.
- Hausling, L., H. Ringsdorf, et al. "Biotin-Functionalized Self-Assembled Monolayers on Gold: Surface Plasmon Optical Studies of Specific Recognition Reactions." Langmuir **7**(9): 1837-1840.
- Hu, D. D., J. R. Hoyer, et al. (1995). "Characterization of the interaction between integrins and recombinant human osteopontin." Ann N Y Acad Sci **760**: 312-4.
- Jackson, J. R., M. P. Seed, et al. (1997). "The codependence of angiogenesis and chronic inflammation." Faseb J **11**(6): 457-65.
- Jung, L. S., C. T. Campbell, et al. (1998). "Quantitative Interpretation of the Response of Surface Plasmon Resonance Sensors to Adsorbed Films." Langmuir **14**: 5636-5648.

- Jung, L. S., K. E. Nelson, et al. (1999). "SPR Measurement of Binding and Dissociation of Wild-type and Mutant Streptavidin on Mixed Biotin-Containing Alkylthiolate Monolayers." *Sens. Actu. B* **B54**(1-2): 137-144.
- Jung, L. S., K. E. Nelson, et al. (2000). "Binding and Dissociation Kinetics of Wild-Type and Mutant Streptavidins on Mixed Biotin-Containing Alkylthiolate Monolayers." *Langmuir* **16**(24): 9421-9432.
- Klumb, L. A., V. Chu, et al. (1998). "Energetic Roles of Hydrogen Bonds at the Ureido Oxygen Binding Pocket in the Streptavidin-Biotin Complex." *Biochemistry* **37**(21): 7657-7663.
- Knoll, W., M. Liley, et al. (1997). "Supramolecular architectures for the functionalization of solid surfaces." *Adv. Biophys.* **34**: 231-51.
- Laibinis, P. E., R. G. Nuzzo, et al. (1992). "Structure of monolayers formed by coadsorption of two n-alkanethiols of different chain lengths on gold and its relation to wetting." *J. Phys. Chem.* **96**(12): 5097-5105.
- Laibinis, P. E., G. M. Whitesides, et al. (1991). "Comparison of the structures and wetting properties of self-assembled monolayers of n-alkanethiols on the coinage metal surfaces, Cu, Ag, Au." *J. Am. Chem. Soc.* **113**(19): 7152-7167.
- Laskin, D. L. and K. J. Pendino (1995). "Macrophages and inflammatory mediators in tissue injury." *Annu Rev Pharmacol Toxicol* **35**: 655-77.
- Liaw, L., M. Almeida, et al. (1994). "Osteopontin promotes vascular cell adhesion and spreading and is chemotactic for smooth muscle cells in vitro." *Circ Res* **74**(2): 214-24.
- Nelson, K. E., L. Gamble, et al. (2001). "Surface Characterization of Mixed Self-Assembled Monolayers Designed For Streptavidin Immobilization." *Langmuir* **17**: 2807-2816.
- Nuzzo, R. G., L. H. Dubois, et al. (1990). "Fundamental studies of microscopic wetting on organic surfaces. I. Formation and structural characterization of a self-consistent series of polyfunctional organic monolayers." *J. Am. Chem. Soc.* **112**(2): 558-69.
- Nuzzo, R. G., F. A. Fusco, et al. (1987). "Spontaneously Organized Molecular Assemblies. 3. Preparation and Properties of Solution Adsorbed Monolayers of Organic Disulfides on Gold Surfaces." *J. Am. Chem. Soc.* **109**: 2358-2368.
- Nuzzo, R. G., E. M. Korenic, et al. (1990). "Studies of the temperature-dependent phase behavior of long chain n-alkyl thiol monolayers on gold." *J. Chem. Phys.* **93**(1): 767-773.
- Nuzzo, R. G., B. R. Zegarski, et al. (1987). "Fundamental Studies of the Chemisorption of Organosulfur Compounds on Au(111). Implications for Molecular Self-Assembly on Gold Surfaces." *J. Am. Chem. Soc.* **109**: 733-40.
- O'Brien, E. R., M. R. Garvin, et al. (1994). "Osteopontin is synthesized by macrophage, smooth muscle, and endothelial cells in primary and restenotic human coronary atherosclerotic plaques." *Arterioscler Thromb* **14**(10): 1648-56.

- Poirier, G. E. and T. M. J. (1994). "The c(4X2) Superlattice of n-Alkanethiol Monolayers Self-Assembled on Au(111)." Langmuir **10**(9): 2853-2856.
- Poirier, G. E. and E. D. Pylant (1996). "The Self-Assembly Mechanism of Alkanethiols on Au(111)." Science **272**: 1145-1148.
- Porter, M. D., T. B. Bright, et al. (1987). "Spontaneously Organized Molecular Assemblies. 4. Structural Characterization of n-Alkyl Thiol Monolayers on Gold by Optical Ellipsometry, Infrared Spectroscopy, and Electrochemistry." J. Am. Chem. Soc. **109**: 3559-3568.
- Prime, K. L. and G. M. Whitesides (1991). "Self-assembled organic monolayers: model systems for studying adsorption of proteins at surfaces." Science **252**(5010): 1164-7.
- Raghow, R. (1994). "The role of extracellular matrix in postinflammatory wound healing and fibrosis." Faseb J **8**(11): 823-31.
- Ratner, B. D. (1993). "New ideas in biomaterials science--a path to engineered biomaterials." J Biomed Mater Res **27**(7): 837-50.
- Rieley, H., P.-N. J., et al. (1995). "A NEXAFS and UPS study of thiol monolayers self-assembled on gold." Surface Science **331-333**(pt. A): 189-195.
- Rollo, E. E., D. L. Laskin, et al. (1996). "Osteopontin inhibits nitric oxide production and cytotoxicity by activated RAW264.7 macrophages." J Leukoc Biol **60**(3): 397-404.
- Schonenberger, C., J. A. M. Sondag-Huethorst, et al. (1994). "What Are the "Holes" in Self-Assembled Monolayers of Alkanethiols on Gold?" Langmuir **10**(9): 611-614.
- Schwartz, Z. and B. D. Boyan (1994). "Underlying mechanisms at the bone-biomaterial interface." J Cell Biochem **56**(3): 340-7.
- Sellers, H., A. Ulman, et al. (1993). "Structure and binding of alkanethiolates on gold and silver surfaces: implications for self-assembled monolayers." Journal of the American Chemical Society **115**(21): 9389-9401.
- Senger, D. R. and C. A. Perruzzi (1996). "Cell migration promoted by a potent GRGDS-containing thrombin-cleavage fragment of osteopontin." Biochim Biophys Acta **1314**(1-2): 13-24.
- Senger, D. R., C. A. Perruzzi, et al. (1994). "Adhesive properties of osteopontin: regulation by a naturally occurring thrombin-cleavage in close proximity to the GRGDS cell-binding domain." Mol Biol Cell **5**(5): 565-74.
- Smith, L. L., H. K. Cheung, et al. (1996). "Osteopontin N-terminal domain contains a cryptic adhesive sequence recognized by alpha9beta1 integrin." J Biol Chem **271**(45): 28485-91.
- Smith, L. L. and C. M. Giachelli (1998). "Structural requirements for alpha 9 beta 1-mediated adhesion and migration to thrombin-cleaved osteopontin." Exp Cell Res **242**(1): 351-60.
- Streuli, C. H. and M. J. Bissell (1990). "Expression of extracellular matrix components is regulated by substratum." J Cell Biol **110**(4): 1405-15.

- Tang, L. (1998). "Mechanisms of fibrinogen domains: biomaterial interactions." J Biomater Sci Polym Ed **9**(12): 1257-66.
- Tang, L. and J. W. Eaton (1993). "Fibrin(ogen) mediates acute inflammatory responses to biomaterials." J Exp Med **178**(6): 2147-56.
- Tang, L. and J. W. Eaton (1995). "Inflammatory responses to biomaterials." Am J Clin Pathol **103**(4): 466-71.
- Tang, L., L. Liu, et al. (1998). "Complement activation and inflammation triggered by model biomaterial surfaces." J Biomed Mater Res **41**(2): 333-40.
- Tang, L., T. P. Ugarova, et al. (1996). "Molecular determinants of acute inflammatory responses to biomaterials." J Clin Invest **97**(5): 1329-34.
- Tyler, B. J., D. G. Castner, et al. (1989). "Determining depth profiles from angle dependent X-ray photoelectron spectroscopy: the effects of analyzer lens aperture size and geometry." Journal of Vacuum Science & Technology A **7**(3): 1646-54.
- Tyler, B. J., D. G. Castner, et al. (1989). "Regularization: a stable and accurate method for generating depth profiles from angle-dependent XPS data." Surface and Interface Analysis **14**(8): 443-50.
- Ulman, A. (1996). "Formation and Structure of Self-Assembled Monolayers." Chem. Rev. **96**: 1533-1554.
- Wang, R. L. C., H. L. Kreuzer, et al. (1997). "Molecular Conformation and Solvation of Oligo(ethylene glycol)-Terminated Self-Assembled Monolayers and Their Resistance to Protein Adsorption." Journal of Physical Chemistry B **101**(47): 9767-9773.
- Zhao, X. M., J. L. Wilbur, et al. (1996). "Using two-stage chemical amplification to determine the density of defects in self-assembled monolayers of alkanethiolates on gold." Langmuir **12**(13): 3257-3264.
- Ziats, N. P., K. M. Miller, et al. (1988). "In vitro and in vivo interactions of cells with biomaterials." Biomaterials **9**(1): 5-13.



## Vita

Kjell Erik Nelson was born in Seattle, Washington in 1964. He graduated from The Bush School in 1982, then transferred from Shoreline Community College to the University of Washington in 1985. After early studies in mathematics and physics, he obtained his B.S. in Microbiology in 1989. He then worked for two years in the University of Washington's AIDS Clinical Trials Group as a research technologist performing HIV culture to support clinical trials of HIV therapies and vaccines. This led, unpredictably, to several contracts with the United States Antarctic Program, both of which included deployment to McMurdo Station, Antarctica (with one full-year deployment.) While working in McMurdo, Kjell had various duties: leading the civilian winter-over HazMat control team, a member of the winter-over primary Search And Rescue team, and the *de facto* on-site water quality expert, measuring potable water quality levels from samples in McMurdo and the South Pole Station. In this capacity, he traveled to the South Pole Station to successfully remediate a bacterial contaminant detected in their potable water distribution system. Ultimately rewarded with a Congressional Medal for Antarctic Service, he returned to Seattle and enrolled as a Ph.D. student in the UW's Center for Bioengineering (now the Department of Bioengineering.) During his work as a graduate student, he worked closely with the University of Washington Engineered Biomaterials group, acting as the student educational outreach coordinator during UWEBs first several years. In addition to the work described in this

dissertation, his thesis research included designing and constructing a surface plasmon resonance imaging device for imaging the creation of surface protein density gradients and DNA microarray studies. He was awarded the first Tom and Barbara Cable graduate research fellowship in 1999, and was the recipient of two National Science Foundation graduate research training grants. In 2001, the Department of Bioengineering specifically called upon Kjell to design and instruct a course in introductory cell and molecular biology for the first year graduate students, filling in for a faculty member who had recently left the department. This work led to several contracts with the University of Washington Extension's Evening Degree program, for which Kjell developed and instructed two quarter-long evening courses for professional engineers earning their Master of Medical Engineering degrees (offered through the Department of Bioengineering). This further led to a position as research scientist for the University of Washington's Center for Engineering Learning and Teaching working on an educational initiative to integrate biology into undergraduate engineering curricula. Kjell's current plans are to integrate his knowledge in both research and education to develop new educational initiatives to bring the life sciences into engineering disciplines; he presently lives in Seattle with his wife Elisabeth and their children Ethan and Erica.